

THE FLOW FIELDS RESPONSIBLE FOR THE GENERATION OF TURBULENCE NEAR THE WALL IN TURBULENT SHEAR FLOWS

Ву

Jeffery Allan Lovett

A THESIS

Submitted to
Michigan State University
in partial fulfillment of the requirements
for the degree of

MASTER OF SCIENCE

Department of Mechanical Engineering

1982

ABSTRACT

THE FLOW FIELDS RESPONSIBLE FOR THE GENERATION OF TURBULENCE NEAR THE WALL IN TURBULENT SHEAR FLOWS

By

Jeffery Allan Lovett

Knowledge of the turbulence production mechanism in the wall regions of bounded turbulent shear flows is essential for an understanding of the overall generation of new turbulent energy. A simultaneous visualization and hot-wire anemometry experiment was performed to determine the flow fields responsible for disturbances to the wall layers in a turbulent boundary layer. Two orthoganal views were employed for the visualization study, which captured the wall layer disturbances and the flow structure above the wall. The results show that concentrated vorticity on scales of the order of the Taylor microscale is highly correlated with the initiation of the bursting phenomenon. The data suggest that in the streamwise plane, the vorticity is configured in counter-rotating transverse vortex pairs.

To my father Marvin, and my mother Nancy, for their encouragement, faith and continual support throughout my college career.

ACKNOWLEDGEMENTS

The author would like to acknowledge the Air Force Office of Scientific Research for their financial support throughout this investigation. The author wishes to express his gratitude to Dr. Robert E. Falco, my major professor, for his guidance and assistance throughout my graduate program. I would also like to acknowledge the services of Mr. Brian M. Leary without whom this investigation would not have been achieved. The author wishes to thank Mr. Fritz Dotzlaf and Mr. Nelson Maldonado of the Turbulent Structures Laboratory for writing some of the computer software used in this study. In addition, I would like to express my sincere gratitude to Miss Mary Ann Ewing who patiently composed all of the tables in this report. Thanks are also due Mr. Brian E. Agar for assembling the vorticity probes used in this study, and Mr. David B. Signor for his assistance.

TABLE OF CONTENTS

LIS	T (OF	FI	Gl	JRE	ES		•	• •		•		•	•	•		•	•	•		•	•	• •	• •	•	•		•	•	•		•	•	•	•		. •		•	v
LIS	T (OF	TA	BI	LES	3		•	• •		•		•	•	•		•				•	•	• •	• •	•			•	•	•		•	•	•	•		,	v	ij	ii
LIS	T (OF	SY	MI	301	LS	•	•	• •		•	• •	•	•	•		•	•	•	• •	•	•	•	• •	•	•		•	•	•		•	•	•	•		. •	•	j	x
СНА	PTI	ER																																						
1	IN'	rrc	טסט	CJ	ric	NC	•	•	• •		•		•	•	•		•	•	•		•	•	• •		•	•		•	•	•		•	•	•	•		•		•	1
2		2.1 2.2 2.3	L 2	De Ec	social so	i pi ce si	me dı de	en ur	t e a t	: i		ns	•	•	•	• •	•	•	•	• •	•	•	• •	• •	•	•	• •	•	•	•	• •	•	•	•	•	• •	• •	•	3	28 38 11
		2.6	5	Ac	ccı	ır	ac	y	•	• •	•	• •	•	•	•	• •	•	•	•	• •	•	•	• •	• •	•	•		•	•	•	• •	•	•	•	•	• •	• •	•	6	53
	RE:																																							
4	DI	SCt	JSS	IC	NC	•		•	• •		•	• •	•	•	•	• •	•	•	•	• •	•	•	•	• •	•	•	• •	•	•	•	• •	•	•	•	•	• •	•		16	52
5	COI	NCI	LUS	IC	ONS	5	• •	•	• •	• •	•	• •	•	•	•	• •	•	•	•	• •	•	•	•	• •	•	•	• •	•	•	•	• •	•	•	•	•	• •	•		18	34
REF	'ERI	ENC	CES		• • •	• •		•	• •	• •	•		•	•	•		•	•	•		•	•	•	• •	•	•		•	•	•	• •	•	•	•	•	• •	. •		18	38
FIG	URI	ES	• •		• • •	• •		•	• •		•		•	•	•		•	•	•		•	•	•	• •	•	•		•	•	•	• •	•	•	•	•	• •	, •		19	€3
TAE	LE	5 .	•••	• •	•••	• •		•	• •	• •	•	• •	•	•	•	•	•	•	•	• •	•	•	•	• •	•	•		•	•	•	• •	•	•	•	•		. •		24	14
APF	Z	DI X A B	Ca		i br																																			

LIST OF FIGURES

Figure	2	page
1	Two Views of Split View Motion Picture	193
2	Mirror and Filter Arrangement	194
3	Four Element Vorticity Probe	195
4	Experimental Equipment	196
5	Motion Picture View Dimensions	197
6	Linear Velocity Profile	198
7	Average Velocity vs. Reynolds Number	199
8	U+ vs. Y+ with Log Law Friction Velocity	200
9	Wall Shear Stress	201
10	U+ vs. Y+ with Wall Shear Stress Friction Velocity	202
11	Local Velocity Gradient	203
12	Derivative Signals Associated with a Vortex as a Function of Probe Position	204
13	Causal Structures	205
14	Stagnation Flow Fields Created by Vortex Pairs	206
15	Normal Velocity Signal as a Means of Identifying Structural Boundaries	207

16	Ensemble Averaged Signals of Positive Rings with High Visual Certainty	208
17	Ensemble Averaged Signals of Positive Rings with High Visual Certainty and Centered Pockets	210
18	Ensemble Averaged Signals of Positive Rings with High Visual Certainty and Centered Pockets in Early Stages	212
19	Ensemble Averaged Signals of Negative Rings with High Visual Certainty and Centered Pockets	214
20	Ensemble Averaged Signals of Negative Rings with High Visual Certainty and Centered Pockets in Early Stages	216
21	Ensemble Averaged Signals of Type 1 Structures with High Visual Certainty and Pockets in Early Stages	218
22	Ensemble Averaged Signals of Type 1 Structures with High Visual Certainty and Centered Pockets in Early Stages	220
23	Scaled Signals of Positive Rings with High Visual Certainty and Centered Pockets	222
24	Scaled Signals of Negative Rings with High Visual Certainty and Centered Pockets in Early Stages	224
25	Scaled Signals of Type 1 Structures with High Visual Certainty and Pockets in Early Stages	226
26	Ensemble Averaged Signals of Positive Rings with High Visual Certainty and Centered Pockets After Removing Six Samples	228

27	Ensemble Averaged Signals of Positive Rings with High Visual Certainty and Centered Pockets in Early Stages After Removing Three Samples	230
28	Ensemble Averaged Signals of Negative Rings with High Visual Certainty and Centered Pockets in Early Stages After Removing Two Samples	232
29	Ensemble Averaged Signals of Type 1 Structures with High Visual Certainty and Pockets in Early Stages After Removing Three Samples	234
30	Percentage of the Time that the Probe Passes Through the Causal Structures Which is Spent in Each uv Quadrant	236
31	Shifting of the Average Due to the Skewness of a Signal	237
32	Sequence showing a positive vortex pair moving wallward with centered pocket occurring in front of probe	238
33	Positive vortex pair with probe at center	240
34	Sequence showing negative vortex pair passing above probe	24]
35	Sequence showing negative vortes pair and small off-center pocket	242
36	Example of type 1 structure	243

LIST OF TABLES

Table	e	page
1	Average Velocities for Each Data Set	244
2	Average Total Quantities for Each Data Set	245
3	u Statistics for Each Data Set	246
4	v Statistics for Each Data Set	247
5	uv Statistics for Each Data Set	248
6	du/dt Statistics for Each Data Set	249
7	dv/dt Statistics for Each Data Set	250
8	dU/dy Statistics for Each Data Set	251
9	<pre>dv/dx Statistics for Each Data Set</pre>	252
10	wz Statistics for Each Data Set	253
11	du/dz Statistics for Each Data Set	254
12	duv/dt Statistics for Each Data Set	255
13	$\overline{\overline{U}}$ Statistics for Each Data Set	256
14	Viscous Length Scale Determined Using Normal Velocity	257
15	Reynolds Stress Averages in uv Quadrants	258
16	Comparison of uv Averages with Brodkey et al. (1973)	259

LIST OF SYMBOLS

- A Collis and Williams constant in $E = A + B Q^{m}$
- B Collis and Williams constant in $E = A + B Q^{n}$
- c. Local skin-friction coefficient
- CF Calibration parameter of forward facing X-wire
- Calibration parameter of rearward facing X-wire
- E Anemometer output voltage
- G Clausers pressure gradient parameter
- H Shape factor
- 1+ Non-dimensional length
- n Collis and Williams exponent in $E = A + B Q^{n}$
- Q Velocity vector
- Qe Effective velocity
- Reg Reynolds number based on boundary layer thickness $(V_{ab} \delta_{A/})$
- Re Reynolds number based on momentum thickness ()
- t time
- t+ Non-dimensional time

- U Total streamwise velocity
- T Average streamwise velocity
- U. Freestream velocity
- u Fluctuating streamwise velocity
- u_x Friction velocity
- V Total normal velocity
- V Average normal velocity
- v Fluctuating normal velocity
- x Streamwise direction
- x+ Non-dimensional streamwise distance
- y Direction normal to the wall
- y+ Non-dimensional distance normal to the wall
- z Transverse direction
- z+ Non-dimensional transverse distance
- B Hot-wire inclination angle
- δβ Error in hot-wire inclination angle
- Boundary layer thickness, 99%
- Angle between velocity vector and probe axis
- Boundary layer momentum thickness
- ρ Density
- τ Local shear stress
- ✔ Kinematic viscosity
- w, Fluctuating vorticity

1 INTRODUCTION

The fundamentals of turbulence production in turbulent boundary layers is currently not understood. An intensive level of research is currently being performed to gain insight into the production phenomenon because of its wide ranging importance in many areas such as energy conservation. The production of turbulence near a wall is the governing mechanism of the turbulent drag from external flow around bodies and in internal flows involving turbulence. The production processes involve the transfer of mass, momentum and energy and therefore have great importance in the heat transfer from surfaces. Thus the production of turbulence and the mechanisms for momentum and energy transfer in turbulent flows is important to the design of all devices in which turbulent fluid is in contact with surfaces.

Our knowledge of turbulence structure has enabled mean velocity distributions to be predicted in pipe flows and

boundary layers using mixing length theories. These theories were initially developed to overcome the complexities of the turbulence phenomenon which limits its mathematical analysis. The majority of design methods in the past have relied on eddy viscosity models determined with the Prandtl mixing length, with modifications such as the Van Driest damping factor for near the wall, and the Clauser model for the outer region. Although these methods serve well for certain classes of turbulent flows they have failed to work satisfactorily for other flow conditions, and do not address the actual dynamics of the flow.

With improved instrumentation and equipment in the middle and late 1950's, evidence began to suggest that the quasi-steady randomly disorganized field of turbulent boundary layers as previously described, actually contained repeated sequences of events with organized structure, which evolved quickly near the wall. In the late 1950's space-time measurements gave a new view of temporal and length scales in boundary layers. It was becoming clear that the turbulent dynamics are governed by or at least closely associated with coherent structures that make up the boundary layer and perform its efficient mixing and transport properties.

Visualization of turbulent flows leading to the structural hypothesis (i.e. the dynamics of the flow are governed by coherent structures) was in essence started by Osborn Reynolds in 1883 when he visually discovered the phenomenon of turbulence. In the late 1920's evidence of a quasi-coherent structure was observed by Prandtl-Ahlborn. Fage and Townend in 1932 emphasized that the so-called laminar sublayer was quite unsteady, after observing the motions of particles in the wall region. The breakthrough visualization of Emmons in 1951 disclosed the turbulent spot in laminar turbulent transition.

In 1956, Townend on the structure of turbulent shear flows presented the hypothesis that large relatively coherent structures play a dominant role in maintaining turbulence. Beatty, Ferrell, Francis, Hama, Emmons and Mitchners work, and the Stanford group headed by Kline, used visualization in the wall layers and observed that the motions were governed by relatively large scale structures and not by local conditions. These observed events were directly contradictory to some existing ideas.

The structural hypothesis of turbulence has become invaluable in the study of boundary layers and free shear flows. Many models and theories have since been developed

focusing on this structural view point. Early theories suggested the outer flow controls the inner flow in the boundary layer, e.g. Einstein and Li (1957). Hanratty (1956), Black (1966) suggest the inner flow may control the outer flow. A more likely hypothesis is that the two flows are related by some intermediate scale coherent structure.

The strength of the turbulence production is substantially larger in the wall regions of boundary layers than in the outer regions. The interaction of the flow with the bounding surface is of great importance to the resulting flow condition downstream. Research into the production of turbulence has naturally been directed toward the near wall regions to gain insight into the processes involved with turbulence production near the bounding surface.

A brief survey of associated literature involving structural aspects of the boundary layer will now be presented describing some of the contributions to the current understanding of turbulent boundary layer structure. First some important results with respect to the outer region flow structure will be described followed by results involving the wall region flow structure.

The middle to late 1950's marks the time when the understanding of coherent structures in turbulent boundary layers began. Corrsin and Kistler (1955) suggested that large eddies were present in the outer region based on observed intermittency from data measured with probes in the outer region. Lumley (1967) suggested a large eddy decomposition of the boundary layer. Townsend (1970) stated that the relatively slow rate of entrainment of the irrotational fluid surrounding the boundary layer is from 'passive' distortion of the bounding surface by eddies of the main turbulent motion. The above observations indicated that coherent eddies of some scale exist in the outer regions of the boundary layer.

Kovasznay, Kibens and Blackwelder (1970) used space-time correlations with conditional sampling and averaging, and observed large scale motions at the turbulent non-turbulent interface, and suggested that these structures occur as the result of violent outward motion from the interior of a bulge in the boundary layer.

Improved mathematical techniques and computers were helping predictive analysis develop. A wave mechanics discription of turbulence and the mechanics of the so called bursting process was developed by Landahl (1967). A

statistical theory for turbulence was developed by Libby (1975) with the aid of structural information. Using the Reynolds equations, Moin et al. (1978) used a large computer to predict instantaneous velocity profiles and the streaky structure in the wall layers.

Brown and Thomas (1977) indicate that a stagnation flow is created at the upstream face of the bulge or large scale motions in the boundary layer, where the stagnation point is located near the center of the bulge, with fluid above riding over the bulge while fluid below moves wallward between the bulges. They suggest that pairing of bursts creating large eddies (as indicated by Offen and Kline) may be wrong. They also give time relations for the large scale inflows.

Falco (1977) observed that Reynolds stress containing events in the outer and inner regions are scaled by inner variables. He observed high Reynolds stress events in the outer flow occurring on the upstream face of large scale motions. These 'typical eddies' are much smaller than the largest identifiable eddies in the boundary layer, and are of the order of the Taylor microscale. These 'typical eddies' might be the intermediate scale coherent structure existing in much of the boundary layer. Falco also

observed a stagnation flow on the upstream face of the large scale motions. Willmarth and Bogar (1977) used very small hot-wires and obtained similar conclusion.

Coles and Cantwell (1977) proposed that large scale structures produced in the later stages of transition sweep downstream passing over the wall layers. They suggest that the streaky structure arises from Taylor-Gortler instabilities from the passage of these large scale structures over the wall layers, leading to turbulence production.

Blackwelder et al. (1978) observed the existence of a sharp inclined shear layer on the upstream face of the turbulent bulges using temperature contamination as a marker. These studies suggest a dynamical relationship between the large structures in the outer region and the so called bursting phenomenon near the wall.

From the investigations of the outer flow, the evidence indicates that active coherent structures of a scale much less than the boundary layer thickness exist in the outer regions. The data suggest that the interaction between these structures and the wall region flow is important, however this process has not been satisfactorily identified. Some investigators have observed large scale

wallward motions associated with the outer flow, mostly involved with the upstream side of the bulge, which could provide the motive force for the interaction of the coherent structures in the outer flow with the wall region flow.

The first big steps in understanding the dynamics of the wall layers in bounded turbulent shear flows began with the Stanford group investigations headed by Kline. While studying diffuser flows at Stanford University, Kline first observed a streaky structure in the wall layers which led to the several Stanford investigations. This group of boundary layer studies was the first evidence that the intermittent Reynolds stress is closely correlated with visually identifiable coherent events in the wall layers.

Rline and Runstadler (1959) first observed a repeated pattern of motions in bounded turbulent shear flows which was termed 'bursting'. This series of motions began with the appearance of a slow speed region or 'streak' on the wall orientated in the streamwise direction. Next was the migratory growth of this region, followed by an oscillatory lift-up of this low speed structure from the wall. Last was the ultimate break-up of this structure as it interacts

with the outer flow, with no observable coherency. Schraub and Kline (1965) verified the 'bursting' observation for turbulent boundary layers with adverse and favourable pressure gradients. The identification of this 'bursting' phenomenon is probably the most significant structural observation of the current information.

Kline et al. (1967) suggested that vortex stretching of an upward tilted streamwise vortex may be the cause of the low speed streak lift-up seen during the bursting sequence. Bakewell and Lumley (1967) used an orthoganal decomposition of the velocity field combined with a mixing length approximation to explicitly calculate the 'large eddies' and observed that the dominant large scale structure in the wall region consisted of randomly distributed counter-rotating streamwise eddy pairs, where vortex stretching governs their evolution.

Employing a small volume element near the wall of a pipe for observation, Corino and Brodkey (1969) observed that an element of accelerated fluid moving toward the wall, which they termed a 'sweep', entered their field of view following the appearance of a slow speed streak. They suggested that the interaction between this accelerated fluid and the retarded fluid of the streak was responsible

for the 'ejection' of low speed fluid from the wall. They used the term 'ejection' to represent the observation of low speed fluid moving away from the wall, which was generally observed to occur rapidly. They state that this ejection of low speed fluid developes an inflexion in the instantaneous velocity profile, with unstable sharp shear layers observed on the upstream face of the ejected low speed fluid, which possibly results in separation of the wall layers.

Kim, Kline and Reynolds (1971) studied the lift-up stage of the bursting process. Their results showed again the oscillatory growth and migration away from the wall of the low speed streaks. Hydrogen bubbles were used for visualization, and they observed the motion of the bubbles assumed a cylindrical shape or S-shaped kink in the time lines. They suggested the existence of vortex lines with components in all three directions. Their results showed that the turbulence production (Their results showed that the turbulence production in the boundary layer occurs during the ejection phase of the bursting process, reinforcing the bursting phenomenon as a major mechanism for turbulence production.

Supta, Laufer and Kaplan (1971) used conditional sampling and their results supported fairly coherent structures existing in the sublayer from studies of the streaky structure. Grass (1971) conditionally sampled the streamwise momentum and observed that low speed fluid moving away from the wall and high speed fluid moving towards the wall contributed equally to the turbulence production. Also, their data indicated that the average production during these events was 1.4 times the long-time average production.

Laufer and Narayanan (1971) found the period of intermittent drops in the wall shear stress was the same as that of the bursting period. Willmarth and Lu (1972) used a detection scheme based on velocity gradients, and their results showed that the Reynolds stress was large during detection, which was to be representative of a burst.

Offen and Kline (1973) observed sweeps which originated in the inner zones, first observed by Corino and Brodkey when they visually marked both outward motions and inward motions. They advocated that bursting involved motions in the logarithmic region that propagate the disturbance, which half the time set-off a new sequence of bursting. They state that the complete process appears to

be quasi-cyclic over time and space. Their data indicated that the low speed momentum deficient lift-up is triggered by high speed momentum excess sweeps, appearing to be related to one event. Furthermore, the sweeps appeared to be involved with two counter-rotating transverse vortices as visualized with hydrogen bubbles created in an x-y plane. The data showed a high shear layer above the wall as the disturbance to the sublayer fluid began. The data also showed high Reynolds stress in the break-up stage made up of small scale motions, but not in the oscillatory stage.

Lee, Eckelmann and Hanratty (1974) using electro-chemical techniques observed that a transverse counter-rotating eddy pair exists before the stabilization of streamwise vorticity leading to lift-up. They present a wall eddy model. Blackwelder and Kaplan (1976) used the short-time variance of streamwise velocity fluctuations for a burst detection scheme. They observed again an inflexional velocity profile before detection of a burst, but it must be noted that here a burst means the lift-up and subsequent break-up of the low speed fluid. This quasi-steady inflexion is unstable and could cause the burst through instability. They also observed a momentum

excess after detection.

Zilberman et al. (1977) describe a characteristic eddy as an arch, and advocate that sweeps may be faster moving fluid underneath this arch which they observed at one stage. Oldaker and Tiederman (1977) investigated the effects of long-chain polymers on the observed streaky structure of the sublayer, which caused the streak spacing to increase. They suggest that the polymer inhibits vortex stretching.

Eckelmann, Nychas, Brodkey and Wallace (1977) applied a pattern recognition technique based on du/dt and showed that the production of turbulent energy is principally involved with the ejection motions. They also state that the interesting dynamics occur during the acceleration phase.

Falco (1977) observed small scale coherent disturbances in the sublayer of a turbulent boundary layer which occurred randomly with respect to the streaky structure. Using a mineral oil smoke for visualization, he observed the structural feature termed the 'pocket' in the viscous sublayer. Blackwelder and Eckelmann (1978) confirmed the existence of streamwise vorticity in the sublayer suggesting counter-rotating vortex pairs attached

to the wall. Falco (1978) proposed that the production mechanism may be dominated by vortex ring/wall interactions. Doligalski and Walker (1978) calculated the effect of a two-dimensional vortex on the wall layer flow as the vortex convected parallel to the wall in a laminar boundary layer. The results showed stagnation flows were created by certain conditions, which in turn generates new vorticity. The reaction is to lift the new vortex off the wall which would supply lifting motions.

Hogenes and Hanratty (1979) investigated the wall layers with arrays of wall probes and hot-wires and found the dominant flow structure to consist of inflows and outflows. They observed inflected velocity profiles from inflows followed by outflows, as well as outflows followed by inflows.

Falco (1979) identified the 'pocket flow module' as being related to the sweep and ejection phenomena. He observed the presence of a transverse vortex of the same sign as the mean along the upstream boundary of the pocket. The pockets formed in groups where the time scale of the formation is too small for one pocket to be the generator of another. Falco suggested that the lift-up along the vortical legs of a pocket will appear oscillatory when

viewed in two-dimensions. Like Offen and Kline (1973) the Reynolds stress was not observed to be relatively large there.

Falco (1980) classified the evolution of the 'pocket' into five stages of development. From hot-wire measurements above the pockets which were visualized with mineral oil smoke, some charcteristic signals associated with the pocket were presented. Falco proposed that the interaction of a vortical sweep with the wall creates new vorticity on the wall of opposite sign to the sweep vortex. These two vortices then induce each other away from the wall, providing lift-up and appearing oscillatory when viewed in two-dimensions. He submits that the vorticity in the sweep is organized in a ring configuration as suggested by the shape of pockets and the existance of counter-rotating transverse vortices.

There are many observed similarities in the investigations concerning the structure and dynamics of the wall region in turbulent boundary layers. Of course, significant differences also exist between observations. Most of the observations agree concerning the importance of the 'ejection' motions and the 'sweep' motions as

relatively coherent mechanisms for momentum and energy transfer between spatial locations in the wall regions. These motions contain the major contribution to the Reynolds stress and turbulence production, and are closely related to the overall 'bursting' process.

In large, some of the studies point to certain characteristic flow conditions being involved with the events which contain high Reynolds stress and turbulence production, in the form of local accelerations, decelerations, wallward and outward motions. Through instability of the inflected velocity profile, breakdown into small scale motions or local separation has been regarded as the mechanism for these events.

Many of the wall layer studies suggest that the sweep and ejection processes are governed by interactions of concentrated vorticity with the wall and neighboring flow. With the assumption of the existence of this vorticity they explain the interactions leading to the production events, namely the sweep and ejection motions. Some of these studies suggest that the vorticity is redistributed into concentrated regions in the outer layers of the boundary layer, while others suggest that flows toward the wall create concentrated vorticity which in turn causes the

production events. It is certainly possible that this structural form could include the instability phenomenon also.

At this time there is no clear evidence as to the evolutionary details of the production mechanism. recent observations of Falco have uncovered details of the manner in which the sublayer fluid is disturbed, in terms of the small scale three-dimensional pocket feature. pocket appears to be correlated with the formation and destruction of the low speed streaks. The pocket feature forms clearly near the point of origin of visualization markers in the boundary layer, with the streaks apparently being formed by the redistribution of marker which indicates the pockets. The streak then exists until a pocket forms on top of the streak, ending its streamwise extent. The pocket appears to be directly involved with the streaky structure, and as stated above, closely related to the sweep and ejection events. Hence, the pocket is closely associated with the burst event.

Falco has shown that the pocket is closely associated with the occurrence of the large Reynolds stress producing motions, and therefore implicitly involved with the turbulence production process. He has suggested that the

coherent structure providing the sweep motion creating the pockets is in the form of a vortex ring.

This study is an initial attempt to identify the flow condition and structural form above the wall which creates the pocket feature observed in the sublayer fluid. In addition, this study was conducted to investigate the effectiveness of the experimental technique which was used here because of the intention to employ this technique to study several aspects of turbulent boundary layers.

This experiment involves flow visualization employing two orthogonal views, with simultaneous hot-wire anemometry measurements. The occurrence of the pocket feature is observed with a top plan view of the marked sublayer, and a planar slice through the boundary layer in the x-y plane using laser light illumination is observed in the other view, providing information on the structure above the wall when the pocket forms on the wall.

The experiment is described in detail in the next chapter. Considerations involving the effectiveness and execution of the experiment are also included. The results contain detailed information on the boundary layer parameters and the analytical techniques employed, for use as an information base for the experiments to be performed at a future time. A discussion of the results is followed by conclusions.

2 EXPERIMENT

2.1 Description

A simultaneous flow-visualization and hot-wire anemometry experiment was performed to study the vorticity and Reynolds stress content associated with the occurrence of the 'pocket flow module' phenomenon. In particular, to gain information about the flow conditions and structural content of the region above a pocket during the appearance and evolution. The simultaneous visualization of pocket occurrences and the associated structure in the x-y plane, along with measurements of the important flow conditions provides a thorough investigative technique for studying the turbulence production process. This study represents the first in a series of experiments of this type which will be performed to determine information regarding the production of turbulence in the wall regions of wall bounded turbulent shear flows. The following is an

overview of the experiment and the reader is asked to refer to the next section on Equipment for more details.

The flow conditions for this experiment were a zero pressure gradient fully developed turbulent boundary layer, which was artificially tripped and developed along the floor of a low speed air tunnel also described in the next section of this report. The free-stream velocity was 3.02 ft/sec and the momentum thickness Reynolds number $(U_{\infty}\Theta_{\Sigma})$ was 679. This relatively low speed was used in order that the large scale structure of the boundary layer be physically as large as possible to facilitate the visual study of the coherent structures involved with pocket occurrence. Also the hot-wire probe occupies a finite volume, therefore spatial derivatives determined from the probe signals are more accurate if the boundary layer structure is large compared to the probe volume. friction velocity calculated with the Clauser method in the log region was 0.145 ft/sec from a friction coefficient of 0.0046. The friction velocity determined using the wall shear stress, and the value used for all non-dimensional quantities, was 0.131 ft/sec. The temperature of the air was 84 degrees Fahrenheit, the barometric pressure was 29.84 inches of mercury and the kinematic viscosity used

was 0.0001712 ft**2/sec.

The experiment employed a split-view high speed motion picture utilizing notch pass filters, which recorded the two separate views simultaneously on each movie frame, as described in the following section. The pockets were visualized with oil smoke injected from a slit in the wind tunnel wall providing a sheet of marker in the x-z plane on the wall, shown in Figure 1a. The slit has an injection angle of 9 degrees and was 300 mm long in the z direction with a gap of 1.8 mm in the y direction, which is equivalent to a gap of 4.5 y+ and length of 750 z+. The slit injector has been employed in many Turbulent Structures Laboratory experiments. Flood lighting equipped with red filters provided the illumination for the x-z plan view in this experiment.

The smoke was also injected upstream of the slit at a pre-determined location under the developed boundary layer, which partially filled the boundary layer as shown in Figure 1. A x-y plane of green argon laser light illuminated the structure in the boundary layer above the wall. The laser plane was created from a laser beam incident on a cylindrical mirror. The mirror arrangement shown in Figure 2, directed the light from the two views in

such a way, to allow them to be simultaneously captured on a single movie frame. This method is described in detail in the Equipment section of this Chapter. A computer controlled LED clock indicated the sampling of the hot-wire signals and was also captured on the film to allow correlation of the hot-wire data with the visual data.

In order to prevent the two light sources from interfering with each other a notched pass filter arrangement was developed to separate the frequencies of light in the two views. The x-z plan view was illuminated with red light in the frequency range of 600nm-900nm. green laser light used to illuminate the x-y plane is strongest between 488nm and 514nm. The view containing the x-z plane passed through a red filter which passed all light with wavelengths above 625nm and therefore eliminated all the green laser light while passing the red flood light. The view containing the x-y plane passed through a green filter with notch pass of 460nm to 580nm and therefore eliminated all the red flood light while passing the green laser light. The result was simultaneous but separate views. These two views along with the computer controlled clock were recorded with a high speed 16mm motion picture camera.

A four hot-wire probe developed by Dr. J. F. Foss was used consisting of two u-wires arranged in parallel which measured the streamwise velocity at two y locations giving the spatial gradient du/dy, and a X-wire arrangement consisting of two 45 degree slant wires orientated in the x-y plane providing the measurement of the streamwise velocity component 'U', and the normal velocity component 'V'. Comparison of the u velocities from the different wires gives the spatial gradient du/dz. A simple backward difference time derivative was calculated for both u and v, and then using a Taylor hypothesis, based on the local mean velocity, the spatial gradient dv/dx was deduced. parallel wires and also the slant wires were separated by 2.5 l+, and the x-wire center was separated by 12.7 l+ from the center of the parallel wires. The hot-wire signals were simultaneously sampled in time at 750 samples per second. This corresponds to a sample rate of one every 0.133 t+.

Velocity profiles were measured using the same data acquisition system at the downstream position where the hot-wire probe was located. The boundary layer was fully developed at this position and free-stream velocity, the boundary layer parameters are discussed in Chapter 3. The

universal log law was satisfied, although discrepancies between the friction velocity determined with the log law and the wall shear existed. This phenomenon has been observed for low Reynolds number boundary layers by other investigators as well, see Purtell et al. (1981). In order to match the law of the wall the friction velocity determined with the wall shear was used for all non-dimensional quantities because velocity measurements were acquired in the buffer layer. The experiment was performed on a different day from the day when the velocity profile was measured. During the experiment the momentum thickness Reynolds number was matched with the value which was measured on the day when the velocity profile was done, which determined the free-stream velocity for the experiment.

The injection rate for the downstream slit used to visualize the pockets had to be very carefully controlled in order to eliminate instabilities in the shear layer between the injected fluid and the boundary layer fluid caused the difference in velocity, which cause waves in the injected smoke sheet. These waves were eliminated by matching the velocity of injection and the local boundary layer velocity as explained in section 2.4.

The probe measurements were acquired outside the viscous sublayer in the buffer layer at a height of y+=24.2. Because downward motions appear to create pockets, the hot-wire probe was placed at this location in order to measure flow quantities associated with these motions before the strong viscous effects of the sublayer significantly altered their state. As the smoke marker leaves the downstream tangential slit it initially fills only the lower level of the viscous sublayer and only strong disturbances from the outer layers create pockets in the smoke. There is a finite time involved with the movement of the smoke and as the smoke travels downstream it begins to fill the sublayer and the frequency of pocket occurrence increases until a point where the frequency is independent of downstream location. Farther downstream the smoke marker is too severely disturbed by the previous pockets to allow good observation of the pocket phenomenon. This was observed by Falco and Lovett (1982). They found the frequency of pockets to be independent of downstream position after x+ of about 100. The position of the probe must then be in the interval where the frequency of occurrence is independent of x position, and it was desired to be at a location were pockets in all stages of evolution

can be observed clearly. The probe was located downstream of the slit at a distance of x+=181 where these conditions were satisfied.

The hot-wire signals were simultaneously sampled in time during the experiment, digitized with a 12 bit analog-to-digital converter and stored directly on computer. The digitally stored hot-wire signals were converted to velocities using calibration parameters on the computer. The velocities were then used to determine the Reynold stress and several time and spatial derivatives. These signals were then plotted on paper with the sample time indicated via the computer controlled clock included in the motion pictures. The signals were used to determine the flow structures by comparing the signals with the visual data on film.

The four-wire probe was calibrated in the wind tunnel using a fixture which allowed for rotation about the sensing point. The probe axis was aligned with the wind tunnel axis and using the same data acquisition as mentioned above, the voltage outputs were recorded for eight speeds over the operating range. The free-stream velocity was determined with a high quality pressure transducer. The Collis and Williams parameters were

determined by a least squares curve fit to the data recorded. The procedure for calibrating the X-wire assumes the Collis and Williams relation between velocity and wire voltage holds for wires at an angle, and determines the actual angle between the 'X' wires using the voltages observed when the probe is rotated at a small angle. The calibration procedure was suggested by Dr. J. F. Foss and developed by Dr. R. E. Falco, with some changes implemented in this study. The calibration procedure is described in detail in Appendix A.

2.2 Equipment

The actual experiment contained six basic sub-systems to be operated simultaneously. These six systems were:

- 1) Low speed wind tunnel
- 2) Visualization marker injection
- 3) Laser plane light source
- 4) Flood light source
- 5) High speed photography system
- 6) Velocity data acquisition system

Low speed wind tunnel

The wind tunnel is a low speed open circuit

visualization tunnel. The top and side walls are made of clear plexiglass to allow visualization from both directions. The wind tunnel exhausts into a plenum room that ultimately empties outside into the atmosphere allowing for the continuous use of the oil smoke visualization marker. For the present experiment the entrance to the test section was filled with one bank of 1/4 inch diameter plastic straws, followed by 1/16 inch mesh aluminum screen to further lower the free-stream turbulence level and increase low speed steadiness. The free-stream turbulence level is 0.35 %. The flow facility is described in detail by Falco (1980a).

Visualization marker injection

The visualization marker was white mineral oil type N.F. which was vaporized in small oil droplets of the order of 1/2 to 5 microns in diameter. This was done using a C. F. Taylor model 3020 smoke generator, which consists of a heated coiled capillary tube which raises the temperature of the mineral oil before it passes through a convergent nozzle which vaporizes the oil into droplets. The oil smoke then passes through a heat exchanger to lower its temperature.

In this experiment the marker was injected at two locations. A 'Y' connection fitted with two globe valves allowed adjustment of the smoke injection for each of the two locations. A portion of the smoke was injected through a tangential slit in the wind tunnel wall providing a dense sheet of smoke on the wall in the x-z plane to mark the occurrence of pockets. The tangential slit was 300 mm long in the z-direction, with a 1.8 mm gap in the y direction and an injection angle of 9 degrees.

The remaining smoke was injected upstream through a hole in the wind tunnel wall covered with a fairing. The fairing deflects the entering jet causing the smoke to enter the flow tangentially. The location of the injection hole was 84 inches upstream of the tangential slit and 3 inches in the positive z-direction from the x-y view plane. The smoke was injected at this location so that the smoke only occupied the regions of the boundary layer near the wall, causing very high concentration gradients of the smoke marker in the flow structure up to about 150 y+. As the turbulent motions entrain fluid from regions above the wall regions which contain the smoke marker, the flow structures become filled with both the dense marker and clear fluid resulting in very high concentration gradients.

This provided high visual contrast in the structure near the wall which was required by the 16mm high speed film for proper exposure and contrast. High concentration gradients are required for photographic contrast in order to obtain information about the boundaries and the dynamics of these structures. The difficulty of capturing high contrasts on film was a major obstacle of this technique.

Laser plane light source

A plane of laser light provided illumination of the x-y plane to visualize the flow structure above the wall as pockets formed. A Coherent CR-8 Supergraphite argon ion laser supplied a laser beam which incident on a 200 mm diameter front silvered cylindrical mirror produced a plane of coherent laser light. A double convex 100 mm focal distance lens was used to focus the laser beam and hence make the laser plane thinner. This provided more concentrated light in the plane enhancing the contrast of the smoke marker. The distance between the focusing lens and the cylindrical mirror determined the thickness of the laser plane and the angle at which the plane of light spread. High quality front silvered laser mirrors were used to direct the laser beam into position. The beam

entered the wind tunnel test section by passing perpendicularly through a glass plate. The beam then passed through a one inch tube sealed to the wind tunnel wall guarding the beam from the smoke, so that the supply beam would not lose power passing through the smoke in the boundary layer.

Flood light source

Flood lighting of the smoke sheet injected via the tangential slit provided the plan view to indicate the occurrence of pockets on the wall. To achieve the light intensity required for good photography of the smoke filled sublayer, three projection lamps with parabolic mirror reflectors were used. Each projection lamp was mounted in an enclosure equipped with a cooling fan to keep the lamp at optimal operating temperature. Attached to the enclosure was a red Rubilith filter so that the exiting light was filtered red. Each of the three projection lamps were connected to one leg of a three phase 220 volt line. Because of the high speed at which the photographs were taken, a lamp on each leg ensured that at least one lamp was illuminated at all times. A Variac power transformer in series allowed adjustment of the voltage supplied to the

lamps with all three lamps recieving the same voltage.

High speed photography system

A Redlake Locam Model 50-0002 16mm intermittent pin registered high speed motion picture camera equipped with a MAR-KIT 75mm f/1.9 lens was used to record the flow visualization. The film used was Kodak High Speed 7250 Tungsten color reversal film. The view frame contained both the x-y plane view and the x-z plan view as well as a clock run by the computer. The dimensions of the view frame are shown in Figure 4. A mirror and filter arrangement developed at the Turbulent Structures Laboratory to capture both views simultaneously and to eliminate the illumination of the companion view was optimized for this study. The method of capturing each component of the view recorded on film will now be described in terms of the view path shown in Figure 2. This means along a path from camera to object, which is directly the opposite of the direction which the light travels.

The movie camera was located above the wind tunnel with the lens axis in the z direction. A front silvered mirror inclined at 45 degrees to the lens axis was employed

to split and direct the lower half of the view frame downward. Another mirror at 45 degrees to the z axis directed the view in the direction of the z axis through the plexiglass side wall and hence recorded the x-y plane view illuminated with the laser plane. A Kodak Wratten No. 40 green filter was placed between the splitting mirror and the camera lens. This filter allowed the green light from the laser plane to pass to the camera but eliminated the red flood lighting for this half of the view frame. The lower half of the view frame therefore contained only the x-y plane view.

The upper half of the view frame passed above the splitter mirror and then a portion of this view is directed with a mirror at 45 degrees to the lens axis, to a computer controlled clock. This clock indicates the sampling of the hot-wire signals which enables the velocity data to be correlated with the visual data. The remaining view is directed downward through the plexiglass top in the direction of the negative y axis by a mirror inclined at 45 degrees to the lens axis. Thus the upper half of the view frame contains both the x-z plan view illuminated by the flood lights and the clock. A Kodak Wratten No. 92 red filter was employed after the splitting mirror to allow the

red light from the filtered projection lamps to pass to the camera, but eliminated the green line of the laser plane. Two small squares were cut out of the red filter to let small portions of the green line from the laser plane pass to the camera. These small lines were then used to determine the location of the x-y laser plane in the x-z plane when the data was reduced.

The geometry of the mirror arrangement guaranteed that the image distances for the top half view and the bottom half view be equal. All mirrors were adjustable, so that by using a right angle template at the image distance, fine adjustment could be made to assure right angles were created by the view paths.

Velocity data acquisition system

A four element hot-wire probe was employed to measure velocity components. This probe consisted of two single probes, one with two u-wires in a parallel configuration, and another probe with a two element 'X' wire. The two probes were mounted together using a fixture which allowed for the adjustment of one probe with respect to the other probe, which was stationary. The fixture was mounted to a traverse mechanism allowing adjustment in the normal

direction to the wind tunnel wall. Tungsten wire with a diameter of 5 microns was used as the sensing element. The construction of these wires was performed in-house. The hot-wire probe, designed by Dr. J. F. Foss, is shown in Figure 3.

The u-wire axes were in the z direction separated by 0.04 inches in the y direction. These wires then measured the streamwise component of velocity at two y locations from which the spatial derivative du/dy was determined. The 'X' wires were in the x-y plane from which the streamwise velocity component 'U', the component in the y direction 'V', and hence their product the Reynolds stress 'uv' could be determined. The center point between the parallel wires and the center of the 'X' wires were on the same z axis. By averaging the 'U' velocity from the two straight wires the 'U' component of velocity was measured at two z positions from which the spatial derivative du/dz can be determined. Also the time derivatives du/dt and dv/dt can be determined, then using a local Taylor hypothesis the spatial derivative dv/dx can be inferred.

The four hot-wires were operated using four DISA type 55M10 constant temperature standard bridge anemometers.

The four anemometer signals were digitized by a 12 bit

analog-to-digital converter and stored on a DEC PDP-11/23 computer. The four anemometer signals were simultaneously sampled and then digitized. The digitized signals are then sent through a parallel interface to the direct memory access board in the computer and consequently stored. The clock run by the computer consists of ten single LED's and four LED digital readouts. For each data point taken the LED's increment and for every ten data points the digital readouts increment. This enabled every data point to be matched with the events on film. The data acquisition system is shown in Figure 4.

The digital numbers stored on the computer were converted to voltages using computer programs which are part of the Turbulence Structures Laboratory data acquisition system. The hot-wire probe was calibrated in the wind tunnel using the same velocity data acquisition system with an additional channel used for the velocity reference. Appendix A contains a detailed description of the calibration procedure. The velocity reference was the dynamic pressure measured with an impact tube and a static pressure tap in the wind tunnel wall using a pressure transducer. The pressure transducer was a MKS Baratron sensor head model 146H-O.1 and a MKS Baratron signal

conditioner model 170M-6b. The sensor head consists of a diaphram and variable capacitor unit which measures the differential pressure, and the signal conditioner converts the signal to a voltage linearly proportional to pressure in torr. The accuracy of this unit is approximately 0.00001 torr. The hot-wire voltages and pressure transducer voltages were determined with the above data acquisition system and then averaged with the computer. From this data a relation between hot-wire voltage and velocity for each of the hot-wires can be derived as explained in Appendix A describing the calibration procedure. These voltage velocity relations were then applied to the experimental data to determine the velocity components.

2.3 Procedure

The following represents the procedure used for performing this experiment. A list of the items that were checked prior to running the experiment is also included.

The experimental data was taken in eighteen seperate runs. The amount of raw data which could be sampled and stored continuously determined the length of a single run.

The data was then saved and the analog-to-digital converter recycled before the next run started. The time associated with the exposure of a roll of movie film allowed for six data runs during a roll of film. Three rolls of film were taken with eighteen corresponding data sets.

INITIAL CHECKS:

- 1) Clean all surfaces concerning visualization.
 - a) laser mirror
 - b) cylindrical mirror
 - c) focusing lens
 - d) glass plate in wind tunnel floor
 - e) top and side plexiglass
 - f) splitter mirror and 45 degree mirrors
- Check equipment grounds.
 - a) computer on same line as A/D
 - b) clock on same line as A/D
 - c) pressure transducer on same line as A/D
 - d) movie camera on seperate line
- Turn on cooling fans.
 - a) projection lamps
 - b) clock
- 4) Check Variac transformer setting.
- Fill smoke generator with mineral oil.
- 6) Adjust filter positions.
- 7) Set computer default assignments.
- 8) Check computer hard-disc for storage room.
- 9) Monitor hot-wires with oscilliscope for clear signals.
- 10) Record temperature and barometric pressure.
- 11) Check camera settings.
 - a) aperature
 - b) shutter speed
 - c) framing rate
- 12) Check for proper cable connections.
- 13) Adjust projection lamp aim.

- 14) Zero pressure transducer.
- 15) Calibrate A/D.
 - a) run up to speed and record average and range voltages
 - b) set gain
 - c) set offset
 - d) set scanning order

EXPERIMENTAL PROCEDURE:

- 1) Position fixture to shade probe from laser in place.
- 2) Turn laser power up.
- 3) Position laser plane location template in place.
- 4) Adjust location of laser plane.
- Position right angle template in place.
- Focus movie camera on x-y face of right angle template. 6)
- 7) Check lens aperature.
- 8) Remove right angle template.
- 9) Remove laser plane location template.
- 10) Remove shading fixture.
- 11) Bring tunnel to operating speed.
- 12) Turn on smoke injection system.
- 13) Make any necessary adjustments in smoke injection.
- 14) Turn on projection lamps.
- 15) Turn on movie camera.
- 16) Start A/D sampling after camera reaches steady speed.
- 17) Turn off camera when A/D sampling is complete.
- 18) Turn off projection lamps.19) Turn off smoke injection.
- 20) Save data file created by run of A/D.
- 21) Return to step 12 until film ends.
- 22) Turn down laser power.
- 23) Remove camera and reload film.
- 24) Replace camera and plug back in.
- 25) Repeat from step 1.

2.4 Considerations

This investigation involved several systems each of which had to be developed in order to achieve the desired goals. The experiment was a difficult one to perform because all systems had to be operated simultaneously, and because of the complexity of visualizing the proper region in the boundary layer with two seperate methods of marker injection. The following considerations were made in developing this experiment in order to achieve a successful investigation.

Visualization marker injection

The mineral oil smoke used as the visualization marker was injected at two locations with different methods. As with any flow visualization the marker must not disturb or alter the flow in which it is marking. The smoke marker for both injection locations was supplied by the same smoke generator. A globe valve on each injection line allowed individual adjustment.

The tangential slit injection rate was very important because unless the injection velocity was matched to the local flow velocity a shear layer existed between the viscous sublayer of the boundary layer on the wind tunnel

wall and the sheet of smoke marker leaving the tangential slit. This shear layer would become unstable and longitudinal waves would be observed in the smoke sheet. This of course would alter the flow field at the measuring position.

The injection rate was adjusted with a globe valve and the condition of the smoke sheet was observed using a polaroid camera with a high shutter speed. Only when these local velocities were matched did the waves induced by shear layer instability disappear, indicating the proper injection rate. Acoustic disturbances had to be eliminated in order to allow these instability waves to be eliminated. The cooling fan for the computer controlled clock and the fan equipped projection lamps were suspended from the ceiling so that fan vibration would not be transmitted to the wind tunnel. A carraige was used to mount all mirrors, filters and the movie camera, which was connected at the top of the wind tunnel and extended over one side. A tripod was employed under the carraige to support the weight and remove the lower frequency vibrations of the high speed movie camera that would otherwise be transmitted to the wind tunnel by a cantilever effect.

The smoke marker injected upstream of the tangential

slit was also controlled with a globe valve. The criteria for this injection was to have the highest density of smoke marker to provide high scattered light intensity for the x-y plane view. The limitation was that if too much smoke was injected the smoke marker would leave the fairing as a strong jet which would possibly alter the flow conditions downstream. With the injection rate low enough the marker was redistributed immediately upon leaving the fairing, indicating that the injection would not effect the flow conditions downstream. High concentration gradients are required for photographic contrast in order to obtain information about the boundaries and the dynamics of these structures. Still photographs at high shutter speeds and test motion pictures were taken to determine the optimum smoke marker density, i.e. the optimum injection rate.

High speed photography

Many test films were run to develop a working photographic technique for this study. The following discussion describes the factors and limits which were investigated to arrive at these results.

The short time scale involved with the motions of the smoke marker required high speed motion pictures, i.e. high

camera shutter speeds and high framing rates. This in turn requires high light levels for proper exposure of the film. A portion of the experiment involved investigating the trade-offs between forcing the film to achieve higher sensitivity to light and supplying higher light intensity. Forcing the film was an adequate method for raising the sensativity of the film and hence achieving the proper exposure level. To achieve proper exposure 400 ASA film needed to be forced 2 stops and this amount of forcing caused the grain size of the film to be very large. density gradients in the smoke marker indicate the structural properties and must be photographed; these gradients often occur over short spatial distances. increased grain size eliminated much of the contrast created by these density gradients and therefore forcing the film to this level was unacceptable.

The flood lighting was originally supplied by four large quartz halogen lamps. The reflectors with these lamps were poor, the result being only a small percentage of the light output was directed towards the object to be illuminated. Using a light meter one of these lamps were compared with a tungsten filament type projection lamp equipped with a parabolic mirror reflector. The light

intensity was 2 f stops higher for the projection lamps than for the quartz halogen lamps. This added intensity was enough to eliminate one stop of film forcing using only 3 projection lamps. Of course the density of the smoke marker played an important role in the amount of light required for proper exposure, but the density of the smoke was dependent upon the volume output of the smoke generator. Because the injection rates at the two locations were determined by the flow conditions, little adjustment was available for exposure control.

The intensity of the laser light scattered by the smoke marker in the boundary layer depended on the laser output intensity, smoke marker density and the degree to which the laser plane was focused. The laser output was variable but was normally operated at full power because obtaining high enough light intensities was the difficulty. A focusing lens was used before the cylindrical mirror to focus the laser beam before it was spread into a plane. The intensity of the laser plane could be varied by simply changing the distance between the focusing lens and the cylindrical mirror. However, the smaller the diameter of the beam the thinner the laser plane would be and the smaller the angle of spread had to be

large enough to illuminate the majority of the boundary layer in the cameras view, and this became a limiting factor. As it turned out the thickness of the laser plane could be varied to some degree, which in turn varied the light intensity, therefore the positioning of the focusing lens was used to control the light intensity in the x-y plane view. A globe valve allowed adjustment of the injection rate of the smoke marker while the density was dependent on the smoke generator output. As mentioned earlier the tangential slit injection rate was fixed so that the range of boundary layer injection also indirectly determined the smoke density.

The computer controlled clock was operated at higher than recommended voltages to produce higher light intensity output from the LED's. A small fan was used to direct cooling air on the LED's so that they would not fail. The light level worked out very well and no further adjustment was required.

The geometry of the mirror arrangement for directing the images to the camera guaranteed that the distance from the wind tunnel wall to the camera via the top view path was equal to the distance from the x-y plane to the camera via the bottom view path. The computer controlled clock

was placed at this same distance. All three images were then at the same distance from the camera and were all in focus simultaneously. A template with a 90 degree angle was placed with one side in the x-z plane and one side in the x-y plane. Viewing through the camera lens the mirrors were adjusted so that the sides of the template from the two views formed a straight line. Since the thickness of the template was equal in both planes, when both sides created a straight line it assured that the focal distances were equal.

The axis of the view path containing the x-z plane had to be in the same plane as the laser plane in order for the view to be directed straight down the x-y laser plane, thus assuring equal focal distances and perpendicular image reflections at all mirrors. This was accomplished by adjusting the mirrors until the x-y plane of the template appeared as a line in the top view. After these adjustments a final focus was made concentrating on the x-y plane view because the detail of the structure visualized with the laser plane was more important than the x-z plane view. The x-z plan view of the pockets illuminated with flood lights was much less sensitive to focus and depth of field than was the x-y plane view, containing the marker

density gradients and detail of the boundary layer structure.

A relatively large focal length lens was used (75mm) to make the physical image fill the movie frame. The distance from the image to the film plane was relatively large for this large of lens, which meant the actual light creating the image occupied very small cross-sectional area as it passed through the plexiglass side walls, filters and reflected off mirrors. The small area of plexiglass which this light passed through had to be finely polished and mirrors well cleaned prior to the experiment. Care was taken to assure that all filters were planar and perpendicular to the image axis to eliminate distortion in the image.

An additional consideration regarding the flood lighting of the plan view was that the projection lamps would heat the surface of the wind tunnel wall in a relatively short time. The projection lamps were turned on only during the actual data run in order to eliminate this heating which could cause buoyancy effects in the flow.

Hot-wire Anemometry

A four element hot-wire probe was used that consisted

of two seperate probes installed in an adjustable fixture. One probe consisted of two u-wires in parallel and the other probe consisted of two wires inclined at 45 degrees to give an 'X' configuration. The 'X' probe mounted directly in the fixture while the parallel probe could be adjusted for the distance between the probes and the distance from the hot-wire to the fixture. The probes were adjusted in the fixture so that the centers of the sensing volume for each probe were both on a line normal to the probe axes in the z-direction. The distance between the probes was set at twice the thickness of the laser plane to allow some margin of safety with respect to the laser plane contacting the probes during the experiment as discussed below.

A test was performed to determine the effect of having the focused laser plane incident on a hot-wire. The first test resulted in the hot-wire burning up immediately upon exposure. Another test was performed with a new hot-wire which did not fail immediately. The operating anemometer output voltage dropped immediately upon exposure and the cold resistance of the hot-wire increased following exposure. Repeating the test caused the cold resistance to increase futhur. This indicated that the hot-wire was

recieving heat from the laser plane and further, the hot-wire was fatiguing and would probably fail. The thickness of the laser plane was very small, therefore the experiment was performed with the laser plane located between the hot-wire probes. This of course was very difficult to do because the spacing between the probes needed to be as small as possible in order for the spatial derivatives determined from the hot-wire signals to be accurate.

A fixture was created which blocked the portion of the laser plane that would strike the probe. The laser plane was then adjusted into position and the blocking fixture removed. The probe was essentially centered about the laser plane. Hence a favorable condition resulted in that the visual information was acquired from a position centered between the two hot-wire probes, therefore the spatial derivatives obtained from both probes are as highly correlated with the visual information as possible.

An interesting phenomenon was observed during some test runs involving the zero velocity voltage output from the anemometers after the probe was exposed to the smoke marker. The zero velocity voltage was lower after the probe was exposed to the mineral oil smoke. However, after

a long period of time, the next day for example, the voltage would return to the previous value. A study by W. Burkhardt (1979) concluded that the smoke marker did not affect the response or velocity measurement of the hot-wire when operated with an overheat ratio of 1.8, which was used in this study. With two injections of the smoke marker, including the tangential slit injection only about three inches upstream of the hot-wire, the density limit of Burkhardt's investigation was being approached.

A test was performed with the experimental condition for smoke marker injection to investigate the effect of the oil smoke on the hot-wire. The signals were visualized with a storage oscilliscope and average voltages determined with a TSI model 1076 averaging voltmeter. As was concluded by Burkhardt, the response and velocity measurement of the hot-wire was unaffected by the smoke marker. It was concluded that with the velocity other than zero the oil coating the hot-wire was shed from the wire at the same rate as it was deposited, i.e. a steady state situation was created. The effect of the oil smoke was then negligible. When the velocity is brought to zero however, the oil on the hot-wire remains and acts as an insulator causing the zero velocity voltage to be less than

for a clean hot-wire. After some relatively long time the oil evaporated as well as spread out along the supporting structure via surface tension, and the zero velocity voltage returned to the clean hot-wire value. This phenomenon requires more investigation, but the operating conditions were unaffected by the smoke marker. Therefore zero velocity output voltages were obtained before exposing the hot-wire probes to the smoke marker.

Velocity data acquisition system

The anemometers were calibrated prior to this experiment to eliminate amplifier instabilities which could cause ringing in the signal or bad frequency response. The internal square wave generator was used along with a high speed oscilliscope. The high filter was stepped down first, then the gain was increased, followed by decreasing the high filter again, and so forth, until a point was reached were the amplifier became unstable. The gain was then decreased by one setting to assure stability.

The inductance and capacitance of each cable was corrected with settings on the anemometers. The resistance of each cable was measured and this was subtracted from the cold resistance of the cable probe combination. The

overheat ratio of 1.8 was applied, and then the cable resistance added back on, making the overheat ratio more accurate.

The hot-wire anemometers were operated at the flow conditions to be used during the experiment. Using an averaging voltmeter and a storage oscilliscope the average and fluctuating range voltages were determined. The analog-to-digital converter allows for adjustment of an offset voltage to be subtracted from the total voltage supplied, and for the true gain over the response range. The offset was set at the anemometer average output voltage. The range in voltage supplied by the anemometer was about 200 mv either side of the average. The range of input on the A/D was set over this value at 250 mv to compensate for any change in the average voltage that might occur due to changes in the average flow speed, and also to ensure that any unuasally large fluctuations in the signals would not be clipped in the conversion process.

The analog to digital conversion was checked by supplying a known voltage to the A/D converter input channels, and converting the sampled voltage to see if the known value is returned. An uncertainty of 3 millivolts in a 3750 millivolt signal was observed.

2.5 Data reduction techniques

This section describes the techniques involved with reducing the data for this investigation. The listings of computer programs that were developed to be used for this investigation are located in Computer Programs Appendix B. The listings of computer programs which are part of the Turbulent Structures Laboratory data acquisiton system can be obtained through the Turbulent Structures Laboratory.

Calibration data reduction techniques

The four-wire probe was calibrated in the wind tunnel using a fixture which allowed for rotation about the sensing point. The probe axis was first aligned with the wind tunnel axis and using the same data reduction techniques as mentioned below, the voltage outputs were recorded for eight speeds over the operating range. The free-stream velocity was determined with a high quality pressure transducer. The relation used for calculating the velocity from the pressure transducer is derived from Bernoulli's equation and is discussed in Appendix A. The Collis and Williams parameters were determined by a least squares curve fit to the data recorded using the Turbulent

Structures Laboratory program CALFIT. CFCR was the program used to determine the calibration parameters CF and CR for the X-wire, which assumes the Collis and Williams relation between velocity and wire voltage holds for wires at an angle, and determines the actual angle between the 'X' wires using the voltages observed when the probe is rotated at a small angle. The calibration procedure is described in detail in Appendix A, and a listing of program CFCR is included in Appendix B.

Hot-wire signal data reduction techniques

The four hot-wire signals were simultaneously sampled in time, then digitized with a 12-bit analog-to-digital converter. The converted binary numbers were stored directly through parallel interface to the direct-memory-access board of a DEC PDP-11/23 computer. The A/D had to be calibrated where the offset voltage to be subtracted from the input voltage, and the voltage range for the signal were set. During calibration, coded numbers representing this offset, and the gain value to accommodate the range, were stored on the computer by the calibration program ADCAL. The calibration program ADCAL is property of the Turbulent Structures Laboratory. Another Turbulent

Structures Laboratory program called CONVOL was used to convert the binary numbers representing the sampled voltages into the voltage values using the coded numbers representing the offset and gain. The result was a binary file on the computer containing the actual sampled voltage numbers.

The program CONVEL was written by the author which used the hot-wire calibration parameters CF and CR described above, along with the Collis and Williams parameters for each of the wires determined with program CALFIT, also described above. CONVEL accepted the binary voltage files and converted these voltages to velocities using the calibration parameters for the hot-wires, and stored them as binary numbers in another file. In addition the velocities were ensemble averaged over the entire record and the averages stored on computer. The result is files containing the velocity for each individual data point and another file containing the ensemble averaged velocities.

A Turbulent Structures Laboratory program called HARVY, which is a lexical analyzer, allows on line operations to be performed on data sets using macro programs defining the operations. A macro program called

REDUC1 was developed by the author to calculate the following quantities; uv, du/dy, du/dt, dv/dt, duv/dt, dv/dx, and du/dz. After verifying that these operations were performed correctly by HARVY, a Fortran subroutine REDUC2 was written to perform these operations which ran a factor of 6 times faster than did the macro version. The result was an output file containing these quantities in binary numbers to conserve storage space.

The program SEPPTS developed by the author, accepts a binary output file from HARVY and outputs intervals of the data specified by the user, into another binary file.

These intervals of data represent a time interval when an interesting event takes place. Then using program SEP4CH, four of the quantities are output into another ASCII file for input into the plotting program PLOT4S, which plotted these four signals on a Tektronix screen. The listings of programs SEPPTS and SEP4CH are included in Appendix B.

The program PLOT4S developed by the author and now property of the Turbulent Structures Laboratory, uses

Tektronix Plot 10 graphics software to draw plots of the four signals on a Tektronix storage screen. PLOT4S draws these signals and prints the number of the data points at the beginning and end of the interval. Tick marks are made

every ten points on the plot allowing any single data point to be easily determined on the plot. This plot also contains the date of the data, film roll number and movie take number. A copy of each plot was made on paper using a Tektronix Hard Copy Unit. These plots were then used with the movies to determine the structural features of the flow.

Statistical calculations were performed on the data after the quantities of interest were determined using HARVY and REDUC2. The statistical program STSTCS developed by the author, determines the mean, standard deviation, skewness factor and flatness factor of any input data, as well as calculating histogram frequencies.

The program ENSMBL, developed by the author using the Turbulent Structures Laboratory programs DRSYSM, SCALE and MAVRG, was used to create ensembled signals of conditionally sampled events. This program consisted of three parts. The first section separated the samples of data. The second section scaled the data so that every signal contained 50 data points between the two conditional data points. Finally, the data points from each sample were ensemble averaged to create an ensembled signal 50 points long. In addition, 100 points before and after the

event were recorded and scaled with the same factor as the internal signal, and then ensembled also.

The uv quadrant analysis was performed with the program AVGINT, developed by the author. This program separates each data point into a uv quadrant, and then ensemble averages all the data points.

Visualization data reduction techniques

Each frame on the movies contained the x-y plane side view, the x-z plan top view and the computer controlled clock. Small squares were cut out of the red filter used with the top plan view so that small portions of the laser plane would pass through (as small lines) permitting identification of the laser plane location in the x-z plane view. When a pocket was observed to form in the smoke injected via the tangential slit, information about the structure above the wall involved with the pocket formation was available via the planar slice through the boundary layer structure by the laser plane, captured in the side view.

The computer controlled clock consisted of ten LED lights and four LED digital readouts. For each data point sampled the LED lights would increment with a one-to-one

correspondence between the first data point and the first LED light, through the tenth data point and tenth LED light. Every ten data points then caused the LED digital readouts to increment. This allows the exact data point which is being sampled during the time that the camera shutter opens to be identified. The framing rate of the movie camera was set at 100 frames per second, and the sampling rate of the analog-to-digital converter was set at 750 samples per second. Hence, there were 15 data points taken for each two movie frames.

Combined data reduction techniques

The objective of this investigation was to gain information regarding the flow conditions and structural coherency above the wall when pockets were observed to form. The films were analyzed with a L-W Optics Motion Picture Analyzer allowing single frame advancing in either forward or reverse directions. This provided the ability to thoroughly analyze the dynamics and phasing of the visual data. Because of the complexity of turbulent motions in the wall regions, and the observed difficulty in discerning the structures involved due to the manner in which the smoke marker was distributed, the hot-wire

signals became essential in concluding the structural features. The paper plots of the hot-wire signals were used while analyzing the films, providing a clear method of determining structural information from the visual data.

The vorticity component of most interest was 'wz'. To determine the presence of coherent vortices above the wall, the necessary response in the normal velocity component 'v' provided the easiest means of initially identifying substantial vorticity. As discussed in the Results section of this report, the response of the normal velocity when passing through a vortex with substantial 'wz' component is qualitatively independent of the location in the vortex that the measuring probe passes through. For example, if the probe passes through a vortex with vorticity of the same sign as the mean in the boundary layer, the normal velocity will first become negative and then smoothly increase. If the vortex is coherent the signals would have a significant degree of smoothness and symmetry.

The technique used to initially identify coherency in the structure, was to identify a structure which appeared to be associated with the occurrence of a pocket. Next, we would determine the data points by number, that corresponded to the maximum and minimum normal velocity in

the neighborhood of time when this structure passed the measuring probe, and mark them on the paper plot of the signals. With this information the presence of isolated vortices in the structure observed visually, would either be verified by the normal velocity signal or contradicted.

Verification was made when the visual structure showed high correlation with the normal velocity signal with respect to the shape and boundary locations of the structure. Then checking the other important signals for consistancy regarding the vorticity indicated by the normal velocity signal, the vortex would either be supported of disproved. Of course, the other signals were considered to try and identify these isolated vortices when the normal velocity signal was not understood.

Sketches of the vortices identified were made on the signal plots and configurations of these vortices making up the structures were hypothesized. With the presence of coherent vortices determined, and with the structural indications of the visualization, coherent structures above the wall associated with the occurrence of pockets were identified.

2.6 Accuracy

An estimate of the accuracy of the hot-wire probe measurements is described below. The accuracy involved with the visual data is in many ways undefined because the determination of boundaries, for example, is subjective in itself. The accuracies stated below were determined by calculating a result with an input value in the range of the experimental values, and then adding an error value to the input. The resulting output value was subtracted from the output value without error, and then divided by the output value without error to obtain the percentage error in the output.

The analog-to-digital converter was tested for error by supplying the input with a known voltage of 3.75 volts, which is in the range of the anemometer output voltages. This voltage was sampled, stored and converted, with the converted output being 3.75 volts plus or minus 0.003 volts. This represents an error of 0.08 % in the converted voltages.

Using the Collis and Williams parameters determined for the hot-wires and an error of 0.08 % in the converted anemometer voltages, the result was no more than 1.25 %

error in the streamwise velocities and 0.76 % error in the normal velocity.

The error involved with the pressure transducer used to determine the free-stream velocity was 0.0001 torr in 0.0037 torr, or 2.7 %. This results in an error of 1.3 % in the velocity.

The largest standard deviation associated with the curve fit of (volts)**2 vs. (Vel.)**n was 0.0181 volts**2. This corresponds to 0.05 % in the velocity.

Hence, by adding all these possible errors we obtain at most 2.6 % error in the streamwise velocities and 2.1 % error in the normal velocity. This results from direct addition, so the velocities should be in error by about 2 % or less.

All the quantities of interest were determined with the computer, so that the error involved with calculations is negligible. The error in the sampling rate of the analog-to-digital converter is about 0.01 %, so this error will be neglected. Therefore the only additional error involved with the spatial derivatives is that associated with the measuring of distances and the use of the Taylor hypothesis.

The estimated error involved with measuring the

distance between the parallel hot-wires (as well as the distance of the probe from the wall) is at most 0.0025 inches. The wire separation was 0.04 inches. This represents an error of 6.25 % in the measurement. This would contribute an error of 5.9 % in the spațial derivative du/dy at the average value of 25 l/s. If we then add the error in velocity to this error in measurement we have at most an error of 8.5 %.

The average streamwise velocity at the probe position was used in the Taylor hypothesis to convert time derivatives into spatial derivatives. The results of this investigation largely involve quantities which are determined from conditionally sampled events of small scale. Therefore, the proper velocity to use in the Taylor hypothesis is the convection velocity of the events. Certainly the average velocity during these times will not be identical to the long time average, nor will this average velocity necessarily represent the convection speed of the structures. However, the average velocity during the events differed by only 9 % from the long time average, and no certain method was available for determining the convection speed that would not involve error of near the same degree. Hence, the long time average streamwise

velocity was used in the conversion to spatial derivatives.

The error involved with the Taylor hypothesis will now be discussed. The average streamwise velocity at the probe location was about 1.87 ft/sec. The standard deviation in the streamwise velocity fluctuation was 0.461 ft/sec, or 24.6 % of the mean velocity. If we accept a pessimistic 25 % error in the convection speed, then the error introduced in the spatial derivative dv/dx is at most 33 % for an initial dv/dx value of 20.0. The added error in the normal velocity of 2.1 % gives roughly 35 % error at most.

The above error analysis for dv/dx was chosen to illustrate that the measurement error could not account for the observed difference in magnitudes between dv/dx and du/dy seen during the passage of vortices. This observation is discussed in Chapter 3. Basically, the absolute magnitude of the fluctuations in dv/dx was observed to be a factor of two to four lower than the fluctuations in du/dy, which are of the order of 20.0 1/s. From the above results we see that in the worse cases the measurement error can not acount for this difference.

It should be noted that the errors stated above are indeed the worse case. The errors expected in this investigation are about 50 % of the stated errors.

3 RESULTS

The results of this investigation involve the very important results regarding the flow fields responsible for turbulence production near walls as well as the overall effectiveness of the experimental technique. The Reynolds number of the flow in this experiment was extremely low so that the scales of interest in the boundary layer would physically be as large as possible. Because of the low Reynolds number, it was necessary to verify that the boundary layer was fully developed. The first three sections of the results address this point and the reader may wish to skip these sections. Section 4 describes an analytical technique employed to identify isolated vortices in the boundary layer. The results of the detailed flow fields identified are then presented in Section 5. The results are presented in the format listed on the following page.

- 1) Fully developed turbulent boundary layer (pg. 69).

 The measured boundary layer parameters are discussed.
- 2) Data set consistancy (pg. 74). The statistics of each data set used to make up the total data base are discussed with regard to internal consistancy.
- 3) Velocity averages (pg. 80).

 The average quantities at the measuring point are compared with standard values.
- 4) Determination of isolated vortices (pg. 85).

 The technique developed for determining the presence of isolated vortices in the boundary layer is discussed.
- 5) Experimental results.
 - a) Experiment quality (pg. 94).

 The overall quality of the visual and hot-wire results are discussed with regard to their coordinated use.
 - b) Structural configurations (pg. 102).

 The coherent structures which have been identified are discussed as well as other observations.
 - c) Example data (pg. 119).

 Characteristic data is presented.
 - d) Length scales (pg. 123). Discussion of the non-dimensional length scale of the different structures.
 - e) Ensembled signals (pg. 131).

 Ensembled velocity signals are presented and discussed.
 - f) Quadrant analysis (pg. 153). Discussion of the results of a uv quadrant analysis on the signals observed during the passage of the structures.

1) Fully developed turbulent boundary layer.

This investigation required that the experiment be performed using very low Reynolds number turbulent flow so that the flow structure would physically be as large as possible to facilitate the visualization. Falco and Lovett (1982) observed that the pocket feature and the associated evolution process remained very similar between Re of 738 to 2728, and the length scales and time scales followed a power law. Hence, it appeared that the phenomena associated with the pocket feature remained unchanged in nature at low Reynolds number. Because of the extremely low Reynolds number used in this investigation, the flow was checked initially to be certain an equilibrium state was achieved. By injecting the smoke marker at the beginning of the wind tunnel test section, it was determined that the artificially tripped flow would not stay turbulent for free-stream velocities below 2.5 ft/sec. Visually a free-steam velocity of about 3.0 ft/sec produced a tripped boundary layer which appeared to be fully turbulent, and was then checked as discussed below.

A velocity profile was measured using the data acquisition system and a single hot-wire to check that the

flow was fully developed and to obtain the flow parameters at the experimental measuring location. A high quality pressure transducer was employed to monitor the free-stream velocity. A free-stream velocity of 3.02 ft/sec created a boundary layer which was fully developed with standard flow parameters, and a momentum thickness Reynolds number of 679. The profile is shown in cartesian coordinates in Figure 6. The boundary layer thickness is 5.25 inches. The first six data points closest to the wall had to be discounted because it was observed that the wall had an effect on the hot-wire measurements when the hot-wire was closer than 0.06 inches.

A test was performed to determine if the wall effect on the hot-wire was the result of the flow field being changed because of the presence of the probe or was it the result of heat transfer with the wall. The hot-wire voltage was recorded with three different surfaces under the wire; a flat black wood surface, a thin aluminum sheet and a flat black coated aluminum sheet, all equidistant from the hot-wire, with the leading edge taped down and with the wind tunnel at the same flow conditions.

The hot-wire voltage was higher for the aluminum sheets than for the wood, implying an alteration of the

flow field was not the cause, for the voltage would be independent of the type of surface. It was concluded that radiation was not significant because the effect of the flat black coating appeared no different than the semi-reflective coating of the aluminum sheet. The fact that the aluminum resulted in higher voltages than the wood implied that heat transfer by conduction was taking place, because aluminum conducts the heat transferred to it from the hot-wire throughout the sheet much quicker than the wood transfers the heat it recieves. The aluminum sheet then has a lower local temperature under the wire resulting in a higher temperature potential and hence more heat conducted between the hot-wire and the surface.

Figure 7 shows the velocity profile plotted as the average velocity versus the log of the Reynolds number based on y ($U_{\bullet}Y/_{\bullet V}$). From this Figure we see that a semi-logarithmic region exists as expected for a fully developed turbulent boundary layer. By choosing the Clauser line which best fits the data we obtain a friction coefficient of approximately 0.0046 and hence a friction velocity of 0.145 ft/sec. This friction velocity is different from the value of 0.131 ft/sec determined using the wall shear stress which was approximated by the slope

of the velocity gradient at the wall. This discrepency has been observed by other investigators studying low Reynolds number turbulent boundary layers (Schraub and Kline (1965), Purtell, Klebanoff and Buckley (1981)). If the friction velocity based on the velocity gradient at the wall is employed the U+ versus Y+ profile appears as shown in Figure 8. From this Figure we can see that the log law is satisfied when this friction velocity is used.

Figure 9 shows the points near the wall used to determine the wall shear stress. Using the seven velocity profile points shown in Figure 9 a least-squares fit requiring passage through the point 0,0 was performed, resulting in line A. The resulting shear stress at the wall was 100 1/s. The corresponding friction velocity was 0.131 ft/sec. The line marked B in Figure 9 is a least-squares fit to the seven velocity profile points used. The corresponding friction velocity was 0.142 ft/sec, which represents a difference of 8 %. The model requiring passage through point 0,0 was preferred because of the no-slip condition.

Since the measurements were made in the buffer layer the friction velocity obtained from the shear at the wall was used for all calculations. Using the wall shear

friction velocity, the velocity profile plotted with U+ and log Y+, shown in Figure 10, indicates that the relationship u+ = y+ is satisfied. The boundary layer parameters are listed below.

Boundary layer parameters.

Reo	0(in.)	5 *(in.)	Н	G	u _æ (ft/sec)
679	0.471	0.727	1.54	7.50	0.145 log law
					0.131 wall shear

The value for the shape factor H suggested in the low Reynolds number boundary layer study by Purtell et al. (1981) is about 1.53 in good agreement. The friction velocity determined with the log law and determined with the wall shear differ by 10 % compared to 7 % observed in Purtell et al. (1981). The results of the velocity profile confirm that the boundary layer is similar to that which has been observed by other investigators. For the experiment, which was performed on the following day, the momentum thickness Reynolds number was equated with that of the velocity profile.

2) Data set consistancy.

The experimental data used was contained in 17 separate data sets each covering 5.67 seconds which total 96 seconds of data. More than 38 boundary layer thicknesses pass in 5.67 seconds so that good averages are determined over the time covered by each separate data set. The averages of the total velocities U and V were calculated during their determination with program CONVEL, and are listed in Table 1. The quantities of interest (UV, dU/dy, dV/dx, etc.) were calculated using the total velocities with the computer program REDUC2 described in the Data Reduction Techniques section of this report. The quantities of interest were averaged and are listed in Table 2.

The average streamwise velocity of all data sets from the X-wire was 1.866 ft/sec, with a standard deviation in the averages of each data set of 0.0883 ft/sec or 5 %, as shown in Table 1. The average streamwise velocity of all data sets for the top and bottom parallel wires was 1.954 ft/sec and 1.872 ft/sec respectively, both having standard deviations in the averages of under 4 %. The average

normal velocity \overline{V} for all the data sets was -0.0251 ft/sec with a standard deviation in the averages of 0.0096 ft/sec or 38 %. The value of the average normal velocity \overline{V} should be slightly positive, indicating that the X-wire probe was not aligned with the true mean streamline in the boundary layer, causing this average to be negative. The average value of the normal velocity is small enough that this misalignment is not significant. The average UV of the data sets was -0.0659 ft**2/sec**2 with a standard deviation in the averages of 30 %. This large standard deviation is due to the large variation in the average normal velocity \overline{V} . The variation in average velocities appears acceptable for considering the flow conditions equal for the 17 data sets.

The average streamwise velocity $\overline{\mathbb{U}}$ determined with the X-wire was expected to be between the average streamwise velocities determined with the parallel wires, because the X-wires were located midway between the parallel wires. The averages listed in Table 1 show that only for 6 of the 17 data sets was the proper relationship observed. Ten of the data sets have the X-wire average streamwise velocity below both of the average velocities from the parallel wires. Only data set number 3 has the average from the

X-wire above that of the parallels. It is felt that the discrepancy is not the result of the accuracy in measuring the velocities, but rather 5.67 seconds is not a long enough time to average out motions in the z direction. This is substantiated by the observation that the average du/dz in individual data sets (see Table 11) was both negative and positive with a large standard deviation. The average streamwise velocity from the top parallel wire was above that of the bottom parallel wire for all data sets as expected.

The fact that the time interval of 5.67 seconds does not appear to be long enough to average out the fluctuations of velocity in the z-direction can explain the large variance in the normal velocity average as well. The effect of velocity in the z-direction on the parallel u-wires is of second order. However, the effect on the X-wires would appear as an increase in u and v velocity. That is, the normal velocity fluctuation v will contain the unsteadiness of the transverse velocity fluctuations.

The fluctuating quantities used in the analysis of the data were determined by using the fluctuating velocities to calculate the quantities of interest. The fluctuating velocities for each data set were determined by subtracting

the average velocity for each data set from the total velocity signal of the data set. Using the statistical program STSTCS in Appendix B, developed by the author, the mean, standard deviation, skewness factor and flatness factor of the data was determined for each separate data set. Tables 3 - 13 contain a listing of the statistics of the different quantities for each data set. The calculated statistical values for each data set were then averaged and the standard deviation in the values between the data sets was determined to check the consistancy between data sets before considering all the data as having the same flow conditions.

Referring to Table 3, we see that the average of the standard deviation in the fluctuating streamwise velocity u for all data sets was 0.461 ft/sec, with a standard deviation between data sets of 0.031 ft/sec which represents a 7 % variation in the averages, while the average standard deviation in the fluctuating normal velocity v was 0.0879 ft/sec with a standard deviation of 0.0097 ft/sec or 11 % (see Table 4). The average skewness factor for the streamwise velocity fluctuations was -0.43 with a standard deviation in the skewnesses of 0.26. This is compared to the classical value of zero. Also, the

average flatness factor was 2.49 with a standard deviation in the flatness facctors between data sets of 17 %. This shows good agreement with the classical value of 2.5.

The average \overline{uv} (see Table 5) for all the data sets is -0.0185 ft**2/sec**2. The standard deviation in the averages was 0.004 ft**2/sec**2 or 22 %. The average standard deviation in uv was 0.0381 ft**2/sec**2 which is over twice the average \overline{uv} , with a standard deviation between data sets of 14 %. The standard deviation in the skewness factor was 30 % with an average of -1.6, and the standard deviation in the flatness factor was 26 % with an average of 7.68.

The average spatial derivative $d\overline{U}/dy$ for all data sets was 24.5 l/sec. The standard deviation in the averages was 3.345 l/sec, or 14 % (see Table 2). The average standard deviation in du/dy was 21.1 l/sec for all data sets with a standard deviation of 7 % (see Table 8). The average skewness factor is 0.83 and the average flatness factor is 4.5 (note that similar to the statistics of the uv data that set number 8 has a very large flatness).

The spatial derivative dV/dx was essentially zero when averaged over all data sets but with a standard deviation in the averages of 0.0092 l/sec (see Table 2). The average

standard deviation in the spatial derivative was 3.44 l/sec on average with a standard deviation among data sets of 7 % (see Table 9). The average skewness factor was 0.24 and the average flatness factor was 6.38.

The average of all data sets for the time derivative duv/dt was essentially zero with a standard deviation of 0.00808 ft**2/sec**3 in the averages (see Table 12). The average standard deviation was 3.09 ft**2/sec**3 with a standard deviation of 0.4 ft**2/sec**3. The average skewness factor for all data sets was -0.018 with standard deviation of 0.349, indicating possibly that if a longer time average was performed the skewness would be zero. The flatness factor was interesting, the average for all data sets was a large 10.6 with a standard deviation between data sets of 3.26. The statistics of other quantities calculated are listed in Tables 6 - 13.

In conclusion, the statistical data indicates that the time interval of 5.67 seconds, which corresponds to the passage of 38 boundary layer thickenesses, is sufficient time to determine averages in the two velocity components U and V. The variation in averages over this time was small enough to combine the data sets. The averages involving the normal velocity component V are less accurate (for the

reasons stated above) than those involving the streamwise velocity component U for this time interval. The streamwise velocity averages between data sets have variations of the order of 5 % while the normal velocity averages vary by the order of up to 40 %. The standard deviations in the velocities vary by the order of 15 % between data sets for both velocity components.

The spatial derivatives involving the steamwise velocity show variations in the averages of the order of 15 % between data sets, and 10 % in the standard deviations. The spatial derivatives involving the normal velocity show very large variations in the averages between data sets, and 10 % variation in the standard deviations. Hence, a longer time is suggested if convergence of the averages involving the normal velocity V are required.

Velocity averages.

The Reynolds number for the boundary layer in this experiment was very low; therefore, the value of standard quantities describing the boundary layer were determined to confirm that the flow had reached the fully developed turbulent state at the measuring station. The mean shear

at the probe measuring location was compared with that of the velocity profile to confirm that the conditions between the velocity profile and the actual experiment were equal as discussed below.

The Reynolds number based on the momentum thickness was 679. The measurement of the boundary layer thickness δ had some uncertainty involved with it due to an apparent overshoot in the measured velocity profile. The boundary layer thickness was approximately 5.25 inches which gives a Reynolds number based on δ of 7718.

The position of the probe for the experiment was at y+=24.2 or in the outer portion of the buffer layer. The mean shear at this location determined with the average velocities of the parallel wires was 24.5 l/sec with a standard deviation between data sets of 3.35 l/sec.

The velocity values in the neighborhood of y+=24.2 were plotted on a linear scale as shown in Figure 11. The points were curve fit by eye and the tangent to this curve determined. From this Figure we note that a mean velocity gradient of approximately 16 l/sec. was determined. The scatter in the velocities is certainly substantial enough to make the curve fit process difficult. We do not expect to obtain the exact mean shear sensed by the parallel

probe, which measures velocity at two locations separated by 2.45 y+, because the velocity profile has a very strong change of slope at this location. A distance of 2.45 y+ can account for an error of 4.0 l/sec. at this location. The error in the measurement of the distance from the probe to the wall can also account for about 4.0 l/sec in the mean shear value. Considering these sources of error, we feel that the agreement between the mean shear values determined from the velocity profile and the mean shear measured by the probe is acceptable.

The average Reynolds stress \overline{uv} is a standard variable for describing turbulent boundary layers. The average Reynolds stress for all the data sets was -0.0185 ft**2/sec**2 with a standard deviation in the data sets of 0.004 ft**2/sec**2 or 22 %. If this value is non-dimensionalized with the square of the friction velocity we have 1.08. This non-dimensional value approaches unity for high Reynolds number boundary layers as shown by Klebanoff (1954), where for y+=24 he finds the non-dimensionalized Reynold stress to be 0.98. This serves as an indication of the uncertainty in \overline{uv} , indicating up to 10 % uncertainty in this measurement.

The root-mean-square of the streamwise velocity fluctuation was approximately 0.462 ft/sec.

Non-dimensionalizing we obtain

 $u'/U_{\infty} = 0.153$

 $u'/u_{\pi} = 3.53$

The last value was determined using the friction velocity calculated with the wall shear stress which is appropriate for this wall region study. To compare these results with other investigators, the friction velocity calculated with Clauser lines in the log region was used for non-dimensionalizing the value, because the other investigators used Clauser lines to determine their friction velocity. There is about a 10 % difference in the friction velocity, and the non-dimensional value becomes 3.19.

The results of Klebanoff (1954) suggest that the root-mean-square streamwise fluctuation divided by the friction velocity at y+=24 is 3.08. This was for a relatively high Reynolds number boundary layer. A more recent study of low Reynolds number boundary layers (Purtell et al. (1981)) suggests a value of 2.25. The RMS value in this study was apparently determined with an

analog device and linearized anemometry. The RMS value in this study was calculated with the computer from velocity information that was digitized at 750 Hz with a highly accurate 12 bit A/D. The accuracy of this measurement is exceptional although the time interval over which the continuous signal was recorded may be too short, possibly explaining the discrepancy (see section 2).

The turbulence intensity scaled with the free-stream velocity was 0.153. The value suggested by Klebanoff (1954) is about 0.114. The turbulence intensity of the normal velocity scaled with the free-stream velocity for this study was 0.030 (or scaled with the friction velocity gives 0.70). In a boundary layer study by Eckelmann (1970) the value of 0.027 is suggested. In general the turbulence intensity of the velocities measured in this study is higher than cited by other investigators. It is felt that the discrepancy lies in either Reynolds number affects for low Reynolds number boundary layers, or possibly the high resolution of the data acquisition system used in this study allows for a more accurate measurement.

The differences between the measured intensities and those of the other studies referenced above, along with the details discussed in the previous sections are acceptable

confirmation that the boundary layer in this investigation is fully developed and of classical form. The Reynolds number of the boundary layer is so low that exact agreement can not be expected. The large thickness low Reynolds number boundary layer provides excellent opportunities for this type of visual study, allowing physically large structural scale. The sublayer was very large with 0.25 inches equal to 16 y+. In addition, the relative intensities of the velocity signals were large which allows for cleaner signal conversion and strong signal coherency and smoothness.

4) Determination of isolated vortices.

The important component of vorticity in this investigation was 'wz' because if pockets are created by concentrated vorticity in some way, then the shape of the pocket feature implies that along the centerline of the causal structure substantial 'wz' must be present. An important result of this investigation was the development of a data reduction technique to identify isolated vortices with vortex lines having a component in the z-direction.

Since coherent vortices in the boundary layer with

significant 'wz' exist in an environment with strong mean vorticity in the same direction, the identification of their presence was not as simple as first expected. The difficulty arises from simply subtracting the two spatial derivatives, du/dy from dv/dx, to calculate the vorticity at a point as suggested by the definition of 'wz'. There are two problems with analyzing the data in this way.

First, it was observed that as the probe passed through coherent vortices which appeared strong both visually and with regard to the anemometry signals, the absolute magnitude of the fluctuations in dv/dx were a factor of two to four lower than those of du/dy. Therefore simply subtracting the values resulted in the defined vorticity being strongly dominated by the response of du/dy alone. This is indeed a difficulty because du/dy does not have a characteristic fluctuating quality for a given vortex when measurements are being made at a single point in space. The fluctuating quality of du/dy when measured in a Eulerian sense is problem two. The interpretation of Eulerian hot-wire measurements will be discussed first and then the observed difference in the fluctuation magnitudes will be discussed.

Consider a vortex rotating with vorticity of the same

sign as the mean in the boundary layer. If we move with the vortex, we see a velocity distribution of the form shown in Figure 12. As a measuring probe passes through different positions in this vortex the normal velocity 'v' and the streamwise velocity 'u' will appear weaker than observed if the probe passes directly through the vortex center. The spatial derivatives determined from these signals would then appear as shown in Figure 12. Here the signals labeled 1,2 or 3 represent the response as the probe passes through the core of the vortex with position 2 representing passage directly through the center. signals labeled A and B represent the response as the probe passes above and below the core region respectively. spatial derivative dv/dx will have a strong negative peak as the center of the vortex is passed, regardless of the measuring location. This signal provides a necessary condition for identifying the rotational sense of the vortex.

The spatial change in the streamwise velocity du/dx will be identically zero if the probe passes directly along the centerline of the vortex. If the probe passes anywhere above the centerline of the vortex, the du/dx signal will first be positive and then become equally negative for a

vortex of this rotation. Likewise, if the probe passes anywhere below the centerline of the vortex, the du/dx signal will first be negative and then become equally positive. Therefore, this signal indicates whether the probe passes above or below the center of the vortex. The du/dt signal will be qualitatively the same but of opposite sign as the du/dx signal.

The velocity distribution outside the core of the vortex must relax to the ambient conditions, which effectively causes the spatial derivative du/dy at a point such as a in Figure 12, to be of the opposite sign of that found anywhere within the core, such as point b. For a vortex of this rotation the spatial derivative du/dy will be positive as the center of the vortex is passed if the probe passes anywhere in the core. If the probe passes outside the core of a vortex of this rotation, the du/dy signal will be negative as the center is passed. Hence, the spatial derivative du/dy is dependent on the position where the measuring probe passes.

The implications of this signal description are two-fold. First, the spatial derivative du/dy at a point can not be used uniquely to determine the rotation, size or strength of a vortex. The observed dominance of this du/dy

signal in the experimental data, as discussed below, is therefore misleading when trying to identify isolated vortices in the boundary layer by simply subtracting the two spatial derivatives, and observing the response of wz.

Second, the du/dy signal can be used in conjunction with the other spatial derivatives to determine the rotational sense of structures observed visually, when due to the complexity of the turbulent motions and the marker distribution, the rotation can not be discerned in frame by frame analysis. That is, observing the location in the visualized structure which the probe passes through, and considering the sign and phasing of the spatial derivative signals one can deduce the rotation and relative strength of vorticity. In fact, in conjunction with the visualization, the spatial derivatives dv/dx and du/dy can be used to conclude the vorticity, and the spatial derivative du/dx serves as a futher diagnostic in the discrimination.

The observed difference in the absolute magnitude of fluctuations between the spatial derivatives du/dy and dv/dx is not fully understood. It is important to remember that these magnitudes differ by a factor of two to four. The error involved with assuming a Taylor hypothesis in

determining the spatial derivatives was discounted as the source because of the size of this factor. In Chapter 2 the error in the Taylor hypothesis was estimated to be no more than 35 %. This of course, would not account for the factor of four difference. The true convection speed of the vortices is certainly different than the long time mean, but again it is felt that this difference in local speeds would not account for the factor of four. Visually the vortices did not appear to convect very much faster than the total flow on average.

The volume over which the probe measures velocities, determined by the physical space which the hot-wires occupy is a possible source of measurement error. The characteristic length scale associated with the hot-wire sampling rate, which represents the distance which the fluid has passed through between sampling of the hot-wire signals, is 1.94 l+. The spatial derivative dv/dx is determined from the time derivative of 'v', so that 1.94 l+ represents the spacial increment which the derivative is determined. The parallel hot-wires were separated by 2.5 l+. Therefore the spatial derivatives are effectively measured over about the same length and would not be a source of the discrepancy. The size of the vortices are of

the order of 50 1+ and the sensing element of the X-wire is of the order of 2 1+, so that velocity averaging over the length of the wire would also not be a substantial source of error.

Another possibility is that the presence of the wall reduces the fluctuations in the normal direction. This appears to be contradicted only by visual observations of nearly circular and apparently very strong vortices passing the probe which should locally have normal velocity fluctuations of the same order as in the streamwise direction. Again, the hot-wire signals during the passage of these vortices did show a factor of four difference in the absolute magnitude of the spatial derivatives.

The standard deviation of the normal velocity signal was 0.0879 ft/sec on average. The standard deviation of the streamwise velocity signal was 0.461 ft/sec, or a factor of 5.2 larger than that of the normal velocity. This suggests that the fluctuations in the streamwise velocity are a factor of five larger than those of the normal velocity, most probably because of the presence of the wall. This difference might be reflected in the spatial derivatives of the two quantities.

The distribution of the du/dy signal is skewed in the

positive direction, mainly because of the occurence of high shear layers in the boundary layer near the wall, as seen by many investigators (e.g. Corino and Brodkey (1968), Offen and Kline (1973)). This means that the average shear with which vortices 'exist in' may not be represented by the long time mean. It is felt that this is the source of discrepancy between the spatial derivative absolute magnitudes. The other possibilities discussed above appear to be unlikely. The possibility of the skewness being the cause of the quantitative difference is discussed further in Chapter 4.

The data show that the range of fluctuation in the spatial gradients du/dy and dv/dx during interesting events differ at most by a factor of two. That is, if a short time average of the fluctuating signal centered around the event is used as the mean, then the fluctuations in du/dy and dv/dx are near the same order. This observation suggests that the long time mean of du/dy may not be the correct average to apply when trying to identify isolated vortices in the boundary layer.

In conclusion, it is not known why a factor of up to four was observed between the absolute fluctuation magnitudes in the two spatial derivatives du/dy and dv/dx.

The measurement dimensions indicate that this severe discrepency would not be the result of the hot-wire probes measuring ability. The author feels the skewness in the distribution of the du/dy response is the most likely source of the difference.

5) Experimental Results.

5.a) Experiment quality

This investigation was the result of a large amount of preparation to achieve the highest quality of visualization with the equipment available. Many test films were made and several different light sources and filters were investigated to arrive at the final working arrangement. It was apparent from the test films that the flow structure near the wall was extremely complicated and the information provided by the hot-wire probes was needed for a reliable interpretation. The refining of the marker injection techniques was necessary to provide optimum visual data.

The major limiting factor was the output power of the laser. The rated output of the laser was 8.0 watts. The highest output power which could be achieved was 5.6 watts. This indeed jeopardized the experiment severely. Several methods were employed to get the maximum power possible. The output power was observed to decrease slightly as the laser tube became hot, so that the power was set at a low level until a short time prior to the experiment. The

power was then turned up, the mirrors allowed to heat up to a stable temperature and then the laser mirrors were adjusted to obtain maximum power. Also, the passages between the laser tube ends and the end mirrors would contain dust particles which reduce the output power. By filling these passages with clean air, from a bottle of compressed air, the power output could be increased by the order of 0.5 watts.

Another limiting factor was the 16 mm format of the high speed motion picture camera. The short time involved with the turbulent motions requires that a significant number of frames be taken during the time these motions remain coherent, so that the nature of these motions and likewise the flow structure can be comprehended. The framing rate that was necessary was of the order of 100 frames/sec. The motion picture camera available with this capacity employed a 16 mm format. The desired field of view was about 125 mm which required an 8-to-1 reduction in image size, from the physical dimensions to the film. The scale of the density gradients in the smoke marker often approached the resolution of the 16 mm film resulting in the loss of visual resolution in the flow structure.

The minimum shutter speed necessary to sharply capture

the rapidly evolving turbulent motions was 1/1000 sec, requiring high light levels to properly expose the 400 ASA film available. The intensity of the laser source after passing through the filter was not high enough to properly expose the side view. The film had to be forced one stop during developing which increased the grain size of the film and decreased the resolution still further.

The structural coherency of the flow was on average of larger scale than the resolution limit of the film.

Therefore, in the majority of the cases the dynamics in the flow structure was clearly observed. Only when the turbulent motions and/or the marker distribution appeared very complex, or the size of the structure appeared very small, did the resolution of the films become a problem when trying to interpret the visual data. In other words, when the flow structure was easily identifiable the resolution of the film was not a significant factor, but for the cases when the structure and dynamics were hard to define, requiring that the visual data be studied very closely, the resolution would become a limiting factor.

Another limiting factor in the interpretation of the visual data involved the boundary layer marker injection technique employed to visualize the flow structure with the

side view. The boundary layer had to be partially filled with the smoke marker in order to achieve high density gradients of smoke in the flow structures. This was necessary because of the nature of the turbulent boundary layer near the wall, in that the flow structures of interest are not isolated from other structures which contain marker. If too much marker is injected into the boundary layer the entire region near the wall will contain marker with varying density, but not strong enough gradients in the density to provide good photographic contrast. The partial injection technique employed provided satisfactory contrast for exposure of the film. One difficulty with partially filling the boundary layer with marker was that structures from the outer regions of the boundary layer which were sometimes involved with the pocket feature, but did not contain enough marker to be identified. There were often times observed when large spans of the flow, of the order of 200 x+, contained very little marker in the regions above the wall due to the lack of sufficient mixing of the marker upstream by the turbulent motions. The result was that when sufficient marker was present in the wall regions up to about y+=150, the technique worked very well to visualize the

structural features. The times when the smoke marker density was low the flow structure was very difficult to ascertain.

The data were recorded on three separate rolls of film. The first roll had the brightest side view and the third roll the dimmest. The first three data runs on roll three had a very weak side view because the oil reservoir level of the smoke generator was low. The generator was filled with oil for the remaining data runs.

As discussed in section 5b of this Chapter, only the pocket events with satisfactory visual quality in the side view were used for concluding the structural features. The result of the difficulties discussed above, as well as the general complexity of the flow near the wall, was that approximately 50 % of the pocket occurrences were not linked to a conclusive causal flow field. The similarity in velocity response and visual observations suggest that the flow conditions associated with the pocket occurrences involving bad visualization or other problems, did not significantly differ from those identified in this investigation. It is felt that the results presented in this report represent flow fields responsible for the formation of the pocket flow feature. Futher investigation

with improved visualization needs to be conducted to obtain a larger number of samples.

The hot-wire signals were converted digitally with a 12 bit A/D and stored on computer. The initial data were then converted to velocities using the computer programs discussed in Chapter 2. The conversion of these velocities was in general very good. The velocity signals were very clean with a noise level of under 5 %. The sampling rate of 750 samples/sec provided approximately 15 data points over the strongest changes in velocity observed. Hence, the quality of the signals was excellent.

The spatial derivative du/dy was determined directly from two velocity signals so that the noise in the du/dy signal was low as compared to the other derivative signals. The time derivatives were calculated with the simple backward difference method with the resulting signals containing substantial noise, but with the strong changes in the derivatives easily identified. The absolute fluctuations in the streamwise velocity U were about a factor of 5 larger than the normal velocity V fluctuations. Therefore the signal to noise ratio of the quantities involving V were higher. The noise in the du/dt signal was

observed to be up to 10 % of the largest fluctuations. The noise in the dv/dt signal was at most 20 % of the largest fluctuations. The noise in the ensembled signals (see Figure 16b) discussed in the next section are characteristic of the individual signals.

The hot-wire data combined with the visual data provided a powerful technique for determining the flow structure involved with the formation of pockets. As a pocket was observed to form with the top plan view, the side view provided information on the flow structure above the wall. The hot-wire signals indicated the flow direction and strength at the measuring location, which integrated with the visual information allowed the coherency and strength of the flow structures to be determined. Information on the flow fields associated with the formation of pockets was obtained using the two data sources.

The result was a method for determining the flow field which involved a fairly complete data base on which the interpretations were based. The measurement of the actual flow conditions at a point in the field allowed much of the speculation involved with interpretation of the visualization to be removed. The observed response of the

hot-wire signals was used as a necessary condition when interpreting the visual data. The author feels that the results of this study describing the flow conditions associated with the formation of the pocket feature represents an objective observation of the phenomenon. course the results are not void of personal interpretation, but the completeness of this experimental technique provided a high degree of confidence in the interpretation. The combination of the split-view motion picture and the four wire probe provided several describing quantities to confirm or contradict the interpretation of the data. Usually all these quantities were observed to agree with the visual observation, or more than one signal would contradict the visual indication. Studying the data further often resulted in a unanimous descision for a different interpretation.

This study represents the first attempt to obtain information on the flow fields responsible for the formation of pockets and hence turbulence production near walls. The number of identified events for each configuration is not large enough to conclude the relative importance of these configurations. Also the complexity of the flow and the limitations of the visual data restricted

the investigation of the later stages of pocket occurrence. Therefore, this study presents the qualitative features of the flow fields responsible for the formation of the pocket feature. The Turbulent Structures Laboratory is in the process of obtaining a larger format motion picture camera, and the available power output of the laser has recently been increased. The author recommends that this experiment be repeated with the new movie camera to obtain a sufficiently large number of data samples to determine the relative contribution of each structural configuration to the formation of pockets.

5.b) Stuctural configurations.

A result of this study is the identification of coherent structures which are associated with the occurrence of the pocket flow module in the viscous sublayer of a zero pressure gradient turbulent boundary layer. The formation of the pocket feature was observed in the top plan view of the split view movie. The side view illuminated with the laser plane provided information on the structure above the wall. As the pocket feature was observed to form in the sublayer fluid the structural

features above the wall were identified.

The high shear of the turbulent boundary layer near the wall must be considered when attempting to discern the causal structures of pocket occurrence. The fluid regions above the wall when a pocket is first observed to form convect past the pocket relatively quickly, due to the difference in convection speeds between the sublayer fluid marking the pocket and the fluid in the outer regions. Considering the fluid volume above and around the pocket when it first appears in early stages of its evolution as the source of the disturbance, it was observed that once the pocket disturbance is initiated the evolution which follows is in some ways independent of this source.

The general observation is that the flow conditions above the wall provide a disturbance in the sublayer fluid which appears as a coherent depression in the marked sublayer, indicating downward motions, with boundaries that develop into a wishbone shape. The evolution of the pocket is described in terms of five stages by Falco (1980). The structures that appear to initiate the formation of pockets are involved with approximately stages 1 through 3 as described by Falco (1980). As time progresses the causal structure convects downstream and out of the neighborhood

of the evolving pocket. It then appears that the later stages of pocket evolution are the result of the interaction of the disturbed sublayer fluid with the approaching fluid above the wall.

To isolate the causal structures, attention was given to the pockets occuring in early stages at the probe. In addition, pockets which were roughly centered with the probe axis were focused upon, to limit three dimensional effects. Furthermore, when the data was analysed, note was made of the cases where the visual data was not conclusive due to complexity or bad visualization. The events with good visualization were used to conclude on the flow structures and the noted events were compared with these.

The observations discussed above were considered with the criteria discussed in section 4 to arrive at the following results. The results of the visual data are classified below and then some qualitative descriptions of visual observations are presented.

In many cases, the visualization suggested that two vortices existed, as observed in the x-y plane, and that these vortices appeared to be correlated in some way. As discussed in the introduction, it is quite possible that a pair of counter-rotating vortices observed in a plane could

in fact be a vortex ring type structure. With this hypothesis in mind the following classification was determined. The vortices observed in pairs were termed vortex 'rings'.

Six structural configurations were identified as being associated with the occurrence of pockets. Referring to Figure 13 we have

- 1) POSITIVE ORIENTATED RINGS A vortex pair visualized in the X-Y plane where the flow induced between the vortices is in the mean flow direction. The line connecting the centers of the vortices usually makes an angle between 0 and 60 degrees with the wall. The pocket forms initially underneath this structure, and sometimes slightly downstream.
- 2) NEGATIVE ORIENTATED RINGS A vortex pair visualized in the X-Y plane where the flow induced between the vortices is opposite the mean flow direction. The line connecting the centers of the vortices usually makes an angle between 60 and 135 degrees with the wall. The pocket forms initially

- under the bottom vortex, and sometimes slightly upstream of this bottom vortex.
- 3) TYPE 1 STRUCTURES Characterized by good visualization of a vortex with the same sign as the mean, but with the smoke boundary turning upward at the downstream end and then turning downstream, as illustrated in Figure 13. The pocket forms slighly downstream of the mean rotating vortex. The type 1 structure was often observed to be created in the wall regions just a short time before the pocket formed. The mean rotating vortex appears strong. Incomplete visualization was often associated with the type 1 structure.
- 4) SINGLE VORTEX ROTATING IN THE MEAN SENSE A single vortex rotating in the same direction as the mean vorticity with the pocket forming downstream of the vortex center. Incomplete visualization was often associated with mean rotating vortices.
- 5) SINGLE VORTEX ROTATING OPPOSITE TO THE MEAN A single vortex rotating in the opposite direction of the mean vorticity with the pocket forming slightly upstream of the vortex center. Incomplete visualization was associated with opposite rotating

vortices.

6) LARGE SCALE SWEEPS - A relatively irrotational downward sweep of much larger scale than the structures described above, which redistributes the marker in the sublayer on a much larger scale than the pocket dimensions. Small scale fluctuations and vorticity exists within the large scale sweep.

The illustrations of Figure 13 are idealized. The actual shapes of the smoke boundaries which identify the isolated vortices were usually distorted and elongated in the streamwise direction. Although many of the structures appeared as very distorted shapes, most of the vortices appeared as ellipses with the major axis close to the mean flow direction but at a slight angle to the wall, with the downstream end above the upstream end.

The small scale structures create pockets because of the downflow induced at the wall by the concentrated vorticity they contain, when they are in close proximity to the wall. The flow fields responsible for the creation of the disturbances in the sublayer fluid, and hence the formation of the pocket features, are illustrated in Figure 14 for the positive and negative rings. The vorticity induced downflow creates a stagnation flow field at the wall, and therefore a disturbance to the sublayer fluid which initiates the pocket evolution. This induced flow involves high-speed fluid moving toward the wall creating high Reynolds stress.

The total number of the above events identified was 152. Of this 152 there were 43 identifications which involved low certainty due to complexity or bad visualization. Although the hot-wire signals were quite similar to the characteristic signals of the configuration they were classified into, they are not included in the results that follow.

Positive rings accounted for 51 % of the events identified. Negative rings accounted for 13 % and type 1 structures accounted for 11 %. Also 10 % of the events were single mean rotating vortices, 6 % were opposite rotating vortices and 10 % of the events were large scale sweeps.

Observations associated with positive rings.

Several observations associated with positive rings will now be discussed. The line between the centers of the vortices for positive rings makes an angle between 0 and 60 degrees with the wall or positive X-axis. As predicted by vortex image theory, the rings with this orientation will induce themselves wallward as they convect downstream. This was observed, but many cases involved rapid downward motion, implying that some driving force was involved with the downward trajectory.

The high shear causes these rings to stretch and rotate toward smaller angles as they convect downstream. For rings with larger angles the point of maximum negative normal velocity, and maximum disturbance to the sublayer fluid, was located just downstream of the upstream vortex. As the ring rotated, the position of the maximum negative normal velocity moved downstream with repect to the upstream vortex. Hence, the pocket feature was initially observed closer to the upstream vortex for the rings with larger angles, and basically under the ring for rings with shallow angles. Rings with zero angle were observed a few times.

As the positive rings stretched from the shearing

environment, it was observed in several cases that the upstream vortex would become stronger, indicating the two vortices belong to a closed ring where the vortex line is being stretched causing increased rotational velocities. In some cases the pocket did not appear until this stretching occurred, giving sufficient strength to the upstream vortex. There were two cases where the vortices became separated by a relatively large distance and each vortex created a separate pocket. The pockets then merged as they evolved.

Some of the rings with larger angles were observed to move towards the wall very rapidly. The ring then pushed fluid downward in front of it. The initial pocket depression would then start a significant distance downstream of the ring due to the projection of the stagnation streamline, and as the ring became closer to the wall the pocket would develop under the ring. Many times as the positive rings 'contacted' the wall the convection rate of the upstream vortex appeared to decrease and the ring therefore stretched. The downstream vortex would then move downward slightly and then break-up shortly thereafter, while the upstream vortex became stronger or other times decayed.

Another interesting observation concerns the mean rotating vortex which forms the upstream boundary of a pocket, or the horseshoe vortex described by Falco (1980). It often appeared that this mean rotating vortex was created during the later stages at the upstream end of the pocket, as the velocity defective fluid from the stagnation flow creating the pocket interacted with the oncoming flow. This vortex would quickly appear, and sometimes appear to coalesce with the upstream vortex of the positive ring.

Observations associated with pockets in general.

The next four observations were associated with all pockets, not just those created by positive rings. After the initial disturbance was created corresponding to stage 1, the causal structure would begin to pass the depression in the marked sublayer fluid. As the structure moves downstream the downward motions associated with the structure continue to disturb the sublayer fluid causing the pocket depression to become longer in the streamwise direction. That is, the open downstream end of the pocket feature appears to be the result of the location of maximum downward velocity, associated with the causal structure, convecting faster than the pocket, hence drawing this

boundary with it and making the pocket longer. A high correlation was observed between the movement in the downstream boundary of the pocket and the convection of the causal structure.

It should be noted that the visual shape of these vortices was in general elliptical in nature. The major axis was in the streamwise direction and usually inclined at a small angle to the wall. Vortices which appeared very strong were visualized as near round, but mostly this circular marker distribution was confined to the core of the vortex. The use of the hot-wire signals was essential in determining the existance and boundaries of these vortices. Some of the vortices would become extremely distorted after interaction with the wall, but amazingly the velocity signals would still show relatively strong coherency. Furthermore, there is no guarantee that the visually marked center of a vortex coincides with the true center, so again the hot-wire signals become invaluable.

The size of the pockets in general cover a very large range, with the largest pockets being as much as three times the size of the smallest pockets at this Reynolds number. In general the smaller pockets appear strong and evolve relatively quickly.

The visual observation of the pocket feature using the visualization methods of this experiment differs qualitatively from pockets observed by Falco (1977). The smoke marker was injected at two locations in the present experiment so that the boundary layer marker exists above the sublayer marker which identifies the pockets. The pockets are visualized in the top view after the light passes through about a half boundary layer thickness of smoke. The result is that the boundaries of the pocket feature appear much less sharply.

Observations associated with negative rings.

Several observations associated with negative rings will now be discussed. The line between the centers of the vortices for negative rings makes an angle between 60 and 135 degrees with the wall. For negative rings with angles between 60 and 90 degrees the pocket was observed to form initially underneath or slightly upstream of the bottom or opposite rotating vortex. The downward motion upstream of the bottom vortex center was usually very strong and often over a large spatial distance. The pocket was located under this region. Sometimes the lifting of low speed fluid associated with this vortex was strong and at other

times it appeared to be very weak. This is in conjuction with the observation that sometimes the bottom vortex appeared visually to be created during the time that the pocket was forming. That is, the top mean rotating vortex was cleary seen but the bottom vortex appeared only when the pocket feature began to form.

For the negative rings with angles between 90 and 135 degrees, the location of maximum negative normal velocity and hence the initial pocket depression, was farther upstream from the bottom vortex center. Associated with rings of these angles was an observation similar to that described above for positive rings. This is the creation of a mean rotating vortex on the wall at the upstream end of the pocket, apparently caused by the interaction of the oncoming flow with the velocity defective fluid on the upstream side of the stagnation streamline created by the downflow.

Some of the negative rings were observed to rotate in the mean direction due to the mean shear. It should be noted that no negative rings were visually observed moving toward the wall. Vortex induction theory suggests that rings of this configuration should propel themselves away from the wall if orientated with angles between 60 and 90

degrees. This outward movement was observed in about one third of the cases. The motion of the ring will depend on the relationship between the self-propelling force and the applied forces on the ring by the environment in which the ring exists.

Observations associated with type 1 structures.

Several observations associated with type 1 structures will now be discussed. The term 'type 1 structure' represents the general observation of a vortex with sign of the mean vorticity which is visually strong and often very young, which has a smoke boundary shaped like that of Figure 13, and is located very near the wall. In Figure 13 the curve represents the boundary between high marker-density fluid below, and low marker-density fluid above. The mean vortex is indicated by a 'finger' of smoke in a spiral which makes one or more revolutions. The smoke gradient line marking the vortex extends downstream for a short distance, then curves up.

Most type 1 structures looked as shown in Figure 13.

There were cases when the smoke turned up and back upstream similar to the boundary of a positive ring. It is possible that some of these observations are the effect of positive

rings where only the upstream vortex is marked. However, in several cases there existed thin strands of smoke in the regions where the top vortex would be expected, but no sign of rotation was observed. It is also possible that the rotation of the vortex is canceled by the mean rotation of the shear field. In some of the cases, the bottom vortex appeared very dynamic, but there was no sign of rotation in the region where the top vortex would be located.

The type 1 structure often appeared to form in the time it took for the smoke to pass from one end of the field of view to the other. This corresponds to about 25 t+. There existed a relatively horizontal density boundary which began to kink up as it convected downstream. The boundary would start to wrap around in the shape of a mean rotating vortex, as it moved horizontally over the wall. The 'finger' would begin to increase in rotational velocity, and appeared to be entraining clear high speed fluid from above. The density boundary would then start to be induced wallward, indicating that possibly the vortex was moving wallward. A pocket would then begin to form under this downflow induced possibly by the mean rotating vortex. This observation indicates that the concentration of vorticity originates within this time.

There is the possibility that the type 1 structure is created by the flow field set up by a negative ring. The velocity defective fluid upstream of the stagnation streamline could interact with the oncoming flow to create motions similar to the type 1 structure. There were cases where the visualization indicated that a negative ring might be associated with the type 1 observation, but in general no clear observation was seen.

The lift-up of low speed fluid on the upstream side of the mean rotating vortex was very strong. The pockets produced by type 1 structures were strong also. The probe often indicated an inclined shear layer at the boundary between the high smoke density fluid and the clear high speed fluid being entrained by the vortex.

Observations associated with the single vortices.

The single vortices observed showed many of the same characteristics discussed above associated with the ring configurations. Incomplete visualization was involved with the observation of these vortices, implying that the single vortex could belong to a pair of vortices, where the other vortex is not visualized. In general the scale of the single vortices observed was of the same order as the scale

of the vortices in the rings, although a few mean rotating vortices were observed which were quite large. The visualization indicated that an entire region contained significant rotation and a large pocket formed underneath this region. Also there were a few very small mean rotating vortices seen. All the opposite rotating vortices were of the same size as those observed in pairs.

Observations associated with large scale sweeps.

The large scale sweep observations differ from the other observations described above because the sweep events do not cause pockets as defined by Falco (1980). The sweeps do indeed create a depression or disturbance to the sublayer fluid, but the scale of this disturbance is a factor of four times larger and the early stages of evolution are quite different.

An interface is observed between low marker-density fluid from the outer regions and high marker-density fluid from the wall regions. This interface is inclined at about 30 degrees to the wall and moves wallward strongly.

Following this interface, a relatively irrotational large scale downward sweep of fluid is seen. The marker in the sublayer redistributes very quickly into a clear depression

of the same scale as the sweep. Sometimes the upstream end of the sweep was seen to rotate with large scale in the mean direction in later stages. Small scale fluctuations were 'superimposed' on the signals, but the normal velocity remained negative throughout the passage of the sweep.

The observations discussed above are characteristic of the flow phenomenon observed, but larger ensembles, higher resolution photography and more complete visualization are needed for strict confirmation.

5.c) Example data.

The brightness of the motion picture films was low for the reasons described in Chapter 2. This did not present a problem because by viewing the movies in a totally dark room the needed detail was observed. However, this did present a problem in the reproduction of the films for this report. The photographs included here have dark side views which make it difficult to see the structural detail. They are included however, because it is felt that the important characteristics of the structure can be seen.

The dimensions associated with the view frame are shown in Figure 5. The horizontal axis of the signals

represents the long time mean, except for the uv product where the axis represents zero. Time is from left to right, with the corresonding flow direction from right to left.

Figure 32 shows a clear example of a positive ring type structure moving toward the wall with a steep trajectory. The top half of the photo shows the marked sublayer in the x-z plane, the bottom half of the photo shows the x-y plane side view. The two small blue lines in the top half of the photograph indicate the location of the laser plane illuminating the side view. The hot-wire probe can be seen in both views at the left.

The first photo shows the structure approaching the probe. In the second photo we see that the structure is beginning to intersect the probe, and the normal velocity signal starts to decrease strongly as the induced downward motion within the structure is sensed. In addition, the pocket disturbance is beginning to appear in the marked sublayer. It appears, from both the signals and the visual data, that the core of the downstream vortex has missed the probe in this case. Notice the strong downward trajectory of the structure.

In the next photo the probe is inside the structure.

The following photo shows the probe in the center region of the structure, and the signals indicate a maximum negative velocity. The pocket has opened further. The last photo visually indicates that the probe is leaving the structure, and the normal velocity is observed to increase strongly as the induced upward motion occurs. The structure is moving wallward so that the average normal velocity within the structural boundaries is negative.

The signals indicate that the Reynolds stress observed within the structure has a maximum value of over three times the long time mean value. We see a strong response in dv/dx as the upstream vortex is passed indicating that the probe may have intersected the core region. The signals indicate an increase in du/dy as the probe passes through the upstream vortex. However, the du/dy signal does not reach a positive value as expected. We believe that this is caused by the local average of du/dy being different from the long time average. That is, if the local average is much lower (e.g. the dotted line) than the long time average indicated by the horizontal axis, then the proper response in du/dy is observed. This point is discussed in detail in the discussion, as well as concerning the ensembled signals presented in section 5.e.

Figure 33 shows another example of a positive ring, where the probe is located in the center of the structure. We observe a strong sweep with corresponding Reynolds stress of over two standard deviations from the mean. In this case we find that du/dy does become positive during passage of the upstream vortex, and the vorticity becomes significantly negative there.

Figure 34 shows a negative ring case, where the structure is nicely isolated. The probe passes under this structure, but the signals indicate that strong downward flow exists upstream of the structure. In the first photograph, the probe is beginning to pass under the bottom vortex of the structure, and we observe that the pocket has already formed at this time. In the second photo the probe is entering the region behind the structure.

The signals show that a very strong downward motion exists behind the structure. The maximum negative normal velocity is over three times the standard deviation in v. We also observe very strong Reynolds stress, of over three standard deviations away from the mean. The probe passed under the structure so that low du/dy from relatively irrotational flow is sensed outside the structure.

Another example of a negative ring is shown in Figure

35. The bottom vortex of the structure appears to be small and close to the wall. A small pocket forms upstream of the structure and slightly off-center of the laser plane. The smoke marker indicates that fluid is being wrapped under the bottom vortex very near the wall. A large region of high speed fluid is observed moving wallward upstream of the structure, from the u and v signals.

An example of a type 1 structure is shown in Figure 36. The upstream vortex is seen very clearly, and the smoke boundary turns up and downstream at the downstream end. A pocket forms under the structure. The vertical lines on the signal correspond to the boundaries of the structure along the probe axis. This example is presented for its visual clarity. The probe passed under the upstream vortex, so the signal is observed to be weak as the structure passes. However, the strength of the normal velocity and the uv product are substantial.

5.d) Length scales.

The determination of the boundaries of the coherent structures in the wall layers is subjective because of the complexity of the smoke marker distribution. For example, the injection technique employed often produces stratified layers of high and low smoke-density fluid. Determining which layer is the boundary of a structure or the core of a vortex is certainly difficult. A more deterministic method involves using the velocity signals to identify boundaries of vorticity and flow structure. The normal velocity V can be used to determine the time when the probe enters the core of a vortex with a major component in the z direction, because the maximum tangential velocity, and hence normal velocity occurs near the boundary of the core. For an 'wz' vortex the normal velocity V is representative of this tangential velocity as illustrated in Figure 15.

Figure 15 shows how the boundaries of the flow structures along the probe axis can be identified with the normal velocity signal. The time for passage of the structure is determined, and this time is converted into a non-dimensional length with a Taylor hypothesis. The conversion has the form

$$1^{+} = \overline{U} \left(\frac{u_{\tau}}{V} \right) t$$

This method is described below.

Figure 15a shows a characteristic normal velocity signal observed as a positive ring structure passes the

probe. The horizontal axis represents the mean of the normal velocity. Many of the structures identified were moving wallward which would shift the signal down with respect to the axis, but for illustration purposes this is ignored. The dashed lines indicate different signal responses that were frequently observed.

Point a , corresponding to an upward motion, is the effect observed as the probe enters the core region of the vortex with center at 1. If the probe does not intersect a significant portion of the core of the downstream vortex, the dashed signal is characteristic of the probe response. Here point b corresponds to the point where the maximum upward motion is induced by the vortex.

The points a and b represent the downstream boundary of the structure along the probe axis, with respect to the effect on the local flow field. As the probe enters the structure the time when the local minimum normal velocity is reached is shown as point c on the signal. When the probe leaves the structure another upward motion is observed from the upstream vortex, noted with point d. Frequently the normal velocity signal increased further to point e after the probe was observed to leave the structure, but with much less coherency and smoothness in

the signal. The signal contained small scale fluctuations between points d and e and generally appeared not to be associated with a single vortical structure.

The time between the boundary points a and d, or b and d, termed t2, marked the passage of the structure. This portion of the signal for each event identified was used in the ensemble averages discussed in section 5e and for the length scales discussed here. The time termed t1, between the downstream boundary and the minimum normal velocity was used to gain information on the location of this minimum.

The normal velocity signal in Figure 10b is characteristic of that observed when a negative ring passed the probe. Only one vortex passes over the probe in this configuration. The point a, again, represents the upward motion induced by the vortex at position 1. The minimum normal velocity is then reached at point c, near the boundary of the core of this vortex. The normal velocity signal then relaxes to the mean value without the substantial upward motions provided by the second vortex of the positive ring.

The time t2 for the negative ring identifies the time scale for the effects of the vortex, but the time tl represents the passage of the vortex and is then

representative of the length scale of the structure along the probe axis. These time scales are then converted into length scales as discussed at the beginning of this section.

To confirm that the length scale determined in this manner was meaningful the dimensions were measured on the movie film for many of the events. The dimension measured along the probe axis was compared with the dimension inferred from the velocity signal for each separate event, and the percentage difference for each event was recorded. For the positive rings the length scale determined using the normal velocity was on average 5 % larger than the length scale measured along the probe axis. The standard deviation of the differences was 21 %, meaning the length scales differ by either plus or minus about 20 % but average to 5 %. The length scale determined from the time scale might be expected to be larger because the positive rings were observed to stretch as they interacted with the wall, and the time scale measurement takes place over a finite time. The dimensions measured on the film were made from the frame where the structure first contacted the probe.

For the negative rings the length scale determined

with the normal velocity was on average 8.2 % smaller than the length measured along the probe axis. The standard deviation in the differences was 28 % for negative rings. Hence, we can expect to see from 20 to 30 % difference in the length scales between the methods for any one event, but the average length scales should differ by at most 10 %.

In Table 14 the length scales for the structures identified are listed. The standard deviation in the length scales are also included. The length scale determined with time t2 is of the order of 100 viscous lengths for all the structures which involve concentrated vorticity. The corresponding length scale for the sweep event was 240 viscous lengths on average.

The length scale determined using time tl is of the order of 50 viscous lengths for all the structures involving concentrated vorticity. This indicates that the point of maximum negative normal velocity for the positive rings is approximately midway within the structure boundaries on average. The standard deviation in this length scale is 35 viscous lengths. This indicates that the position of the maximum negative velocity occurs both upstream and downstream of the center, corresponding to the

angle of the ring, but on average is near the midpoint.

The true length scale of the negative rings along the probe axis is represented by the length determined with time tl. This length is of the order of 45 viscous lengths. We see here that the standard deviation in this length scale was 15 viscous lengths, which is lower than the variation in the positive ring lengths. This might be expected because the positive rings involve two vortices separated by some varying distance, whereas the length scale of the negative rings only involves the variation in the single vortex length scale.

The length scale for the type 1 structures is similar but slightly larger than those of the positive rings. The length scales for the mean rotating vortices are also similar to the positive ring scales. The length scales for the opposite rotating vortices are more similar to the scales of the negative rings than those of the positive rings, because the lengths are smaller and the standard deviation of the length scale determined with the same as for negative rings.

In general all the structures involving concentrated vorticity have similar orders in the length scales compared to the relatively large scale sweep event. The length

scale of the sweep is about 240 viscous lengths with a standard deviation of only 54 viscous lengths.

For further length scale information, the dimensions of the vortices making up the ring configurations were measured on the films. Again it must be stressed that the measurement of the structural boundaries from the visual data was difficult and can be in error of up to 25 %. The downstream vortex in the positive ring structure was 45.1 viscous lengths on average, the upstream vortex was 41.9 viscous lengths on average. For the negative rings the bottom vortex was approximately 38.6 viscous lengths on average and the top vortex was 39.3 viscous lengths.

The average width of the pockets as visualized in this experiment was determined for comparison with Falco and Lovett (1982). The average width non-dimensionalized with wall layer variables was 63.1 which is above the average found by Falco and Lovett (1982), but within the uncertainty bounds of the investigation. The average non-dimensionalized length was 74.8. This value is again above the average of Falco and Lovett (1982) but within the error bars. The pockets appear qualitatively different in this study, as explained in section 5b, which could explain the larger values.

5.e) Ensembled signals.

The velocity and derivative signals observed as the positive rings, negative rings and type 1 structures passed the probe were ensemble averaged to obtain signals representative of the structures identified, and are called ensembled signals here. The ensemble was created with the upstream and downstream boundary of the structures fixed.

The identification of the upstream and downstream boundaries of the structures were determined with the normal velocity, as discussed in section 5d. With these two points fixed, the individual signals were stretched or compressed so that the boundary points were matched for all the signals. The signals between the boundaries were also converted into 50 points, so that each signal contained 50 points between the boundaries. In addition, one hundred points before and after the boundary points were included. These external points were scaled to the same factor as the signal between the boundaries, for each individual signal. The 100 points before and after the structures corresponds to 13.3 the before and after. The points from all the signals were then ensemble averaged to create the

representative velocity and derivative signals shown in Figures 16 - 22.

All the ensembles are determined from events with higher certainty in the visual data. A further classification of events where the pocket was centered with respect to the probe axis was also made. This constraint should remove three-dimensional effects. Still further, events corresponding to pockets in the early stages of evolution (stages 1 and 2) were grouped. This was done to investigate the signal characteristics of the causal structures before they interacted strongly with the wall.

The vertical lines in Figures 16 - 29 represent the boundaries of the structure. The horizontal axes in all the Figures which follow represent the mean value for all the quantities except the uv product where the axis represents zero.

The ensembled signals for all the positive rings with high visual certainty are shown in Figure 16. From Figure 16a we can see that the normal velocity signals were very well correlated. The shape of the ensembled signal appears as expected for the response of the probe as it passes through a pair of coherent vortices. The maximum negative

normal velocity is over a standard deviation in v. The streamwise fluctuating velocity u shows that high speed fluid is observed during the passage of the positive rings. The maximum u velocity is more than 40 % of the standard deviation in u. The velocity signals outside the boundaries of the structure are essentially the mean value. This indicates that the signals are uncorrelated outside the boundaries of the structure.

The ensembled uv signal in Figure 16a indicates substantial negative uv or positive Reynolds stress in the center region of the structure, which has a maximum value about the mean of about 70 % of the standard deviation.

Outside the structural boundaries the uv product is near the average value. For this case a relatively large number of samples were used in the ensemble, therefore the average uv outside the structure approaches the mean value of -0.0185 ft**2/sec**2. In some of the following cases the sample size is small enough that outside the boundaries the mean value is not reached and in fact the signals do not appear uncorrelated. This is most likely the consequence of small sample size, as shown by the cases with a larger number of samples.

The ensembled uv signal also shows two local maximum

points corresponding to the boundaries. From the individual signals it is seen that these peaks correspond to positive uv peaks for many of the samples. These peaks represent high speed fluid moving upward, internal to the core regions of the vortices in the positive rings. But again, because there are many samples in this ensemble the curve is essentially shifted to be centered about the mean causing the ensemble values to be entirely negative.

The ensembled vorticity signal can be seen to be highly influenced by the du/dy signal shown in Figure 16b. This observation is discussed in section 4 of this Chapter. Notice that positive vorticity is indicated in conjunction with the downstream vortex of the structure. However, the ensembled vorticity is observed to decrease in association with the upstream vortex, but the vorticity does not become substantially negative in a quantitative sense as expected for a vortex with the same sign as the mean (note: relative to the local mean within the structural boundaries it is lower than the downstream peak).

The signal also indicates that a significant positive peak in du/dy exists just outside the downstream boundary.

As the structure moves wallward it must push the fluid in front of it in the streamwise direction. This acceleration

in the streamwise direction along with the close proximity of the wall, results in a region of increased shear and vorticity. Notice that dv/dx is also negative in this region but in a weak sense compared with inside the structural boundaries. Hence, the signals indicate a high shear region of the same sign as the mean shear, with significant rotation existing in front, or downstream of the structure.

In Figure 16b we see that the dv/dx signal has a smooth positive and negative peak coinciding with the vortices of the structure, where both peaks are of the same order as the standard deviation in dv/dx. As discussed in section 4 of this Chapter, the magnitude of the dv/dx signal is significantly lower than the du/dy signal, which is also complicated. Notice that the du/dy signal contains only a small negative peak in phase with the positive peak in dv/dx. This indicates that some of the signals containing the proper derivative response to the vortex may be in the ensemble, but all the signals aren't of this nature.

There is a negative peak in the ensembled du/dy signal near the center of the structure. It is believed that the vortex pairs are sometimes separated by a large enough

distance that a relatively irrotational 'slug flow' is induced between the vortices which causes the negative response in du/dy. This peak also shows up in the vorticity signal of Figure 16a.

The ensembled du/dt signal clearly shows that the probe passes through a region of increasing streamwise velocity at the downstream boundary of the structure, as the probe passes from fluid outside the structure into fluid of higher speed inside the structure. The correlation between this region and the downstream boundary of the structure is excellent.

The ensembled du/dz signal indicates that within the structural boundaries the flow has no significant lateral acceleration. Although the samples used in this ensemble are not constrained to being centered, we would not expect significant du/dz because pockets occur randomly in space

Figure 17 shows the ensembled signals for all the positive rings with the added constraint that the pockets be centered with respect to the probe axis. The normal and streamwise velocity signals are basically unchanged, although the upstream positive peak in the normal velocity is now slightly larger than the downstream peak. The angles observed for the line between the centers of the

vortices suggests that the upstream vortex should influence the velocity signals at the probe to a higher degree than the downstream vortex. However, the rings rotate as they interact with the wall, so that this observation should be stronger for the early stage events discussed next.

From Figure 17a we see that the vorticity signal is essentially the same, except for the positive peak at the downstream vortex which has disappeared. This is possibly due to the probe passing under the downstream vortex, which eliminates the negative response in du/dy as discussed in section 4 of this Chapter (see Figure 12). The spatial derivatives du/dy and dv/dx are shown in Figure 17b. These signals have become slightly more coherent than for the entire sample ensemble.

The ensembled signals for the further restriction of pockets in the early stages are shown in Figure 18. Note that the positive peak in the normal velocity at the upstream end is now substantially higher than at the downstream end. Here we see that the upstream vortex appears relatively stronger as expected because of the angle of the rings. The signals show a higher positive streamwise velocity region which extends further downstream of the boundary, having a maximum value of about 65 % of

the standard deviation. As these rings move toward the wall they must push the fluid in front of them, which accounts for the positive streamwise velocity region extending downstream.

From the ensembled uv signal we see that the strength of uv within the structure is relatively unchanged, but the uv signal has now a positive region at the downstream end. This positive uv results from high speed fluid moving upward. This is due to the flow field induced by the downstream vortex, which induces the fluid both upward and also in the streamwise direction.

The ensembled vorticity signal is essentially positive within the structure. The negative vorticity region downstream of the structure has become stronger in the early stages of the event. In Figure 18b the ensembled derivatives are shown. Here we can see that the dv/dx signal still indicates the presense of two counter-rotating vortices, but the du/dy signal is basically negative, which dominates the vorticity signal. This negative quality suggests that the core region of the vortical structures may be above the probe level when the pockets first form, so that the flow which the probe experiences is of a relatively irrotational nature, which gives negative du/dy.

The du/dy signal downstream of the structure is very strong and positive, while the dv/dx signal in this region is not comparatively strong. This implies that a strong shear region is created downstream of the structure in the early stages, as the structure pushes fluid in front of it. This is substantiated by the observation that the du/dy signal has become much stronger for the early stage ensemble, whereas the dv/dx signal has remained relatively constant. In addition, the negative dv/dx may be the response from the downstream vortex alone, in the manner illustrated in Figure 12.

Again, the du/dz is very near zero implying no lateral tendencies for centered early stage events.

The ensembled velocity and derivative signals for the negative rings are shown in Figures 19 and 20. Figure 19a shows the ensembles for all negative rings with the constraints of high visual certainty and centered pockets with respect to the probe.

The ensembled streamwise velocity is entirely positive, with maximums within the structural boundaries of about 75 % of a standard deviation. The fluid which is induced downward by the vortex on the upstream side, is

indeed high speed fluid. The streamwise fluctuation induced by the bottom vortex is positive anywhere under the vortex center. The observation that the streamwise velocity is completely positive within the structural boundaries suggests that on average the vortex centers were located above the probe level. This may not be entirely true, because the convection rate of the ring may be strong enough to balance an induced negative fluctuation.

A region of strong negative normal velocity is created by the vortex, which slowly returns to the mean level. The maximum negative normal velocity is about 1.7 times the standard deviation in v, appearing much stronger than in the positive ring cases. The smooth decrease from the positive value at the downstream end, to the maximum negative at the core boundary, indicates the presence of coherent concentrated vorticity. The high positive streamwise velocity in conjunction with mildly negative normal velocity upstream of the structure, suggests that a large scale region of high momentum fluid moving toward the wall exists upstream of the negative rings. This fits the suggestion by Falco (1977a) that compact vortical structures exist on the upstream face of the large scale motions in the boundary layer, where relatively

irrotational stagnation flow is moving toward the wall below the stagnation streamline.

The ensembled uv signal indicates that very high Reynolds stress is involved with the negative rings. The magnitude of the negative uv peak in this case is 1.5 times that of the positive rings. We also see a small positive peak in uv, which represents high speed fluid moving upward as induced by the bottom vortex.

The ensembled vorticity signal indicates the strong positive vorticity of the bottom vortex. The ensembled derivatives are shown in Figure 19b. The dv/dx signal has a strong positive peak corresponding to the bottom vortex of the structure. The ensembled du/dy signal has a substantial negative peak in phase with the positive peak in the dv/dx signal. This implies that the probe did indeed pass through the core of the bottom vortices, although as stated above, the streamwise velocity signal indicates that for most of the samples the center of the vortex was above the probe.

The ensembled du/dt signal also confirms that the vortex centers were above the probe on average, because the increasing-decreasing response in du/dt during the time when the vortex passes corresponds to this position. The

ensembled du/dz signal indicates that no substantial lateral motions occurred.

Figure 20 contains the velocity and derivative signals for negative rings with the additional constraint of the pockets being in early stages. The ensembled streamwise velocity signal is still entirely positive, and the maximum value reached during the passage of the vortex, is higher than for the previous case. This might be expected because we have suggested that this response is due to induction by the vortex, and one would expect the vortex to be strongest in the early stages before it looses energy from the wall interaction.

The ensembled uv signal remained unchanged with the additional constraint, suggesting that the Reynolds stress is relatively constant during the first 3 stages of pocket evolution. The positive peak in the vorticity has flattened slightly on the upstream side. Referring to the ensembled du/dy signal in Figure 20b, we notice that the ensembled signal is flatter in the center region of the structure, and the peak value is slightly lower than the previous case. This indicates that the negative rings responsible for early stage pockets may be higher off the wall, so that the probe passes farther under the vortex

centers. If this were the case then the peak value would be lower and a large relatively irrotational region would be sensed after the probe leaves the vortex, which is indicated by the flat negative du/dy in the center of the structure.

The ensembled dv/dx signal remained essentially the same with this extra constraint.

The ensembled velocity and derivative signals for the type 1 structures are shown in Figures 21 & 22. The type 1 structures which had higher visual certainty also corresponded to pockets in early stages, and the ensembled signals are shown in Figure 21. The ensembled streamwise velocity in Figure 21a shows a narrow high speed region in the center of the structure. The ensembled normal velocity has a strong negative region in the center of the structure, and the signal increases similar to what is expected for a vortex at the upstream end. These signals do not show a high degree of coherency with respect to the presence of a vortex at the upstream end.

The ensembled uv signal has a strong peak very near the downstream boundary. From the individual signals it was observed that the uv peak was in different positions for many of the samples. In several samples, a large region downstream of the visualized vortex was observed to accelerate downward and in the streamwise direction in an irrotational manner as the structure moved wallward, essentially being pushed in front of the structure. This motion provides negative uv which is sensed before the visual boundary of the structure. The visual boundary of the structure was used in connection with the coherency of the v signal in determining the boundary of the structure used in the ensemble. Basically the boundary used corresponded very closely with the visual boundary. The negative uv sensed downstream of the visual boundary contributes to the ensembled signal, and effectively shifts the peak toward the downstream end.

The ensembled vorticity signal has a strong negative peak at the downstream boundary which corresponds to an inclined shear layer which was often observed at the downstream boundary of the smoke marker. The vorticity signal during the remaining structure is essentially positive.

The ensembled derivatives are shown in Figure 21b.

The dv/dx signal has a weak positive peak at the downstream end. The ensembled du/dy signal has a significant positive

peak at the downstream end which is attributed to an inclined shear layer. A negative peak in du/dy occurs in the center of the structure.

The ensembled du/dz has a significant negative peak near the downstream end which implies that the off-centered samples may be significant.

The ensembled signals for type 1 structures with the additional constraint of centered pockets are shown in Figure 17. The ensembled streamwise velocity signal is entirely positive. The normal velocity signal is smoother with this added constraint, and has a larger negative peak. The peak in the uv signal is still near the downstream boundary.

The ensembled dv/dx and du/dy signals are basically unchanged except that the small negative peak in du/dy near the downstream end is removed. The magnitude of the peaks in du/dt have also diminished. There still remains a significant peak in the du/dz signal which should have been removed with this constraint.

The discontinuity in the ensembled signals near the upstream boundary is the result of using one sample which occurred at the very end of a data set. Therefore, no data points after the upstream boundary were contributed to the

ensemble. The ensembled values for the points that follow were determined with the proper sample number.

The results discussed above for the positive rings and the type 1 structures were not as expected. For the positive rings the ensembled signals indicate a significant sharp negative peak in du/dy which is located near the center of the structures. If the vortex pair is separated by a large distance the flow between the vortices would be relatively irrotational which would be sensed as negative in du/dy. What is surprising is that the negative du/dy appears as a sharp peak, which is not expected. Furthermore, the upstream vortex was seen to intersect the probe for the positive rings, but the ensembled du/dy does not show a substantial positive peak at this location.

In the case of the type 1 structure, the upstream vortex visually appeared very coherent and also intersected the probe. The ensembled du/dy signal does not indicate a positive peak corresponding to this vortex. In addition, the overall correlation of the type 1 signals appears to be low.

The visual data suggests that these structures contain concentrated vorticity. The signals used in the ensembles

were plotted together to investigate these discrepancies and to gain information on their overall correlation. The signals which are scaled to match at the boundary points were plotted together and are shown in Figures 23, 24 and 25.

In the scaling process the signals were converted such that there were 50 points between the two structural boundaries. The samples used in the ensemble included 100 data points before and after the boundary points. These external points were scaled with the same factor as was necessary to make the signal within the boundaries match at the two boundary points. The scaling factor for each sample was different, so that the external points end at different locations. This causes the discontinuities in the signals seen in Figures 23, 24 and 25. The ensembled signals in Figures 16 - 22 and 26 - 29 include only half of the signal external to the boundaries, so that these discontinuities are not shown.

The plots are scaled to accommodate the largest signals. The reader must remember that although the majority of the signals may combine to form a band which has some qualitative signature, this scaling may make the band appear very flat. This type of scaling does show the

relative difference in magnitudes between the norm and single uncommon signals.

In Figure 23 the scaled signals for centered positive rings are shown. The velocity signals in Figure 23a show substantial correlation. The uv signals have a large variation in the location of the peaks, but many negative peaks are seen in the center region. The large negative peaks near the upstream boundary correspond to the ejection motions observed with the positive rings.

The dv/dx signals are well correlated, and Figure 23b shows how the magnitude of dv/dx is indeed much lower than that of du/dy. From Figure 23b we can see that in general du/dz is higher outside the boundaries, indicating that the structures do not contain significant lateral motions.

The du/dy signals indicate that there are several samples with very high du/dy near the center of the structures. These samples have very large magnitude as well as sharp peaks. The six samples that contribute these large peaks were removed from the ensemble set to determine if they are responsible for the sharp positive du/dy peak centered between the boundaries in the ensembled signal.

Figure 26 shows the resulting ensembled signals with these six samples removed. The ensembled vorticity signal

in Figure 26a no longer contains the sharp peak in the center region. However, there is significantly more positive vorticity than negative vorticity within the boundaries. Examining the ensembled du/dy signal in Figure 26b, we note that there is still some indication of a negative peak near the center, but this peak is much less substantial. The du/dy signal does increase at the upstream end but does not actually become positive as might be expected if there was a mean rotating vortex at the upstream end.

The du/dy signal does suggest that the upstream vortex is present, if it is accepted that there exists a local mean indicated by the dotted line in Figure 26b. This is further implied by the fact that the local maximum near the upstream boundary is in phase with the minimum in dv/dx, as would be observed for a vortex at this location.

Three of the samples removed also corresponded to pockets in early stages. With these samples removed, the new ensembled signals are shown in Figure 27. Essentially, the signals are very much the same. The major difference is that the upstream positive peak in the normal velocity v becomes even larger compared to the downstream peak. As discussed above, this is expected for positive rings in

earlier stages, before the ring has rotated to a smaller angle.

The removal of the six samples did not alter the other ensembled signals significantly. Thus the influence of the strong events which were removed from the ensemble of early stage events, was not significant. This suggests that we have a sufficient number of samples in the ensemble to achieve a reasonable degree of statistical convergence. It is possible then, that the samples removed from the previous case, which involved a larger number of samples, were simply events which did not belong in the set.

Figure 24 shows the scaled signals used in the negative ring ensemble. The velocity signals shown in Figure 24a appear to be well correlated. Several very strong negative uv peaks are seen. The derivative signals are shown in Figure 24b, where again good correlation is indicated. The ensembled signals for the negative rings were in general very conclusive. Plotting these signals was done mainly to check the internal correlation. The only signals with significant deviation were in the du/dy signals. The two du/dy signals that deviate largely from the band of signals at the upstream end were removed from

the ensemble set. The resulting ensembled signals are shown in Figure 28.

The samples removed appear to be events where the probe passed under the vortex. This is suggested by the change in the streamwise velocity signal. We note that now the u signal decreases outside the vortex as expected, but of course the fluid is still high speed with positive streamwise fluctuation. The other significant change is in the du/dy signal which remains flat in the upstream side of the structure, indicating the relatively irrotational flow induced towards the wall by the vortex.

The scaled signals for the type 1 structures are shown in Figure 25. The velocity signals appear correlated, but the peaks in the uv signals are not in phase. Several strong negative peaks exist at the downstream boundary which causes the ensemble to peak there. Referring to the derivatives in Figure 25b, we see that dv/dx appears well correlated with a positive peak near the downstream boundary.

The du/dy signals indicate that several signals have a strong positive peak near the downstream boundary or center region of the structure. The two very large positive

signals alone could cause the positive peaks seen in the ensembled signal, so these were removed from the ensemble set. Also, the sample with the smaller but narrow positive peak was removed from the set because this signal fluctuated with much shorter wave length than the other signals, implying that it may not be appropriate to include this sample into the ensemble.

The ensembled signals for the type 1 structures with the three samples removed are shown in Figure 29. The ensembled streamwise velocity signal has changed remarkably, and now indicates high speed fluid throughout most of the structure. The normal velocity signal has a slowly decreasing region outside the downstream boundary. The type 1 structures were observed to move wallward rapidly, and this region could be from fluid being pushed down in front of the structure.

The samples that were removed from the original ensemble set contained the large negative uv peaks at the downstream boundary. Hence, the ensembled uv signal in Figure 29b now has a strong peak closer to the center of the structure.

The ensembled vorticity signal is largely positive within the structure, but decreases at the upstream

boundary. With the three samples removed, the ensembled signals for the type 1 structures are amazingly similar to the positive ring signals. Referring to the derivatives in Figure 29b, the dv/dx and du/dy signals are again similar in every way to the positive ring derivative signals. As discussed previously, if the local mean du/dy is at the dotted line in Figure 29b, then the ensembled signals suggest the presence of two counter-rotating vortices.

Hence, it appears that the type 1 structures have a high possibility of being the result of the same phenomenon that has been termed a positive ring. The visual indications support this speculation strongly, for the observation of the mean rotating vortex and the inclined marker boundary downstream in conjunction with the stated incomplete visualization, makes it clear that the type 1 structure could be a positive ring.

5.f) uv quadrant analysis.

To determine the contribution to the total Reynolds stress by the structures that cause pockets, the hot-wire signals observed only during the time that the structures passed the probe were ensemble averaged in each of four

quadrants based on the sign of the product uv.

The occurrence of positive fluctuating velocity u and positive v is termed quadrant 1. This would represent high speed fluid moving upward, and would give a positive uv product or negative Reynolds stress. The occurrence of positive u and negative v is termed quadrant 2. This indicates high speed fluid moving wallward, or a sweep motion as defined Corino and Brodkey (1969). Here the Reynolds stress is positive. Quadrant 3 describes negative u and positive v, which gives positive Reynolds stress and is usually defined as the ejection motion. Last, the occurrence of negative u and negative v is classified as quadrant 4, giving negative Reynolds stress. The hot-wire signals during the time the structures passed the probe were separated point-by-point into each of the four quadrants and then averaged together.

The coherency of the normal velocity signal v as these structures passed the probe provided a good method for determining the boundaries of the structures at the probe level needed to create the quadrant breakdown. The details of this method for determining the structural boundaries was described above in section 5d.

The characteristics of the uv product, or the Reynolds

stress, are important because it indicates the level of momentum transfer associated with these structures. If the Reynolds stress for these structures is substantially above that of the mean in the boundary layer, then the structures involved are responsible for a significant portion of the momentum and energy transfer in the boundary layer at the measuring location.

Traditionally the term $(-e^{i} \overline{w} + \frac{1}{3} \overline{y})$ has been defined as the turbulent kinetic energy production term in the balance equations for turbulent kinetic energy. The value of the average Reynolds stress gives information regarding the production of turbulence because the mean velocity gradient $(\sqrt[3]{3}y)$ is a constant at a given distance from the wall in the boundary layer. Although this velocity gradient does not actually exist at any instant in the flow, this term represents the average production of turbulent kinetic energy.

The product (\overline{uv}) is the long time average of the uv product. If one were to conditionally sample from the total signal, and ensemble these samples, another average denoted $\langle uv \rangle$ could be determined. If the number of samples used in the conditional ensemble is very large, then the product $\langle uv \rangle$ should approach the long time average \overline{uv} . If

the value of this average $\langle uv \rangle$ is significantly larger than \overline{uv} , then the implication is that the conditioned samples contribute significantly to \overline{uv} . In terms of the kinetic energy production term, sampled times which result in a relatively large conditionally sampled ensemble average of the Reynolds stress might be interpreted as important contributors to the overall turbulence production.

If we assume that the average Reynolds stress for the conditionally sampled events presented here will not change substantially as more samples are added, then the conditionally sampled ensembles discussed below indicate the turbulence production associated with the identified structures. The number of samples in the ensembles are certainly too small to attach much confidence to this approach, but the similarity in the velocity signals for the structures identified in this investigation does suggest some consideration. The intent of this investigation was to identify structures associated with the formation of pockets and not to determine their contribution to the turbulence production. However, the following results may be interpreted loosely in this manner as a qualitative result.

Several investigators (Brodkey et al. (1973), Townsend

(1956)) have attempted to define the instantaneous turbulence production, which is not the idea presented here. What is meant by the previous discussion is that samples with a large conditionally sampled ensemble average Reynolds stress can be thought of as events which contribute significant turbulence production to the average in the boundary layer. In other words, the average turbulence production associated only with these events must be part of the average over all time. If this conditional average is quantitatively large, then the contribution from these events is important.

The quadrant breakdown is in terms of the uv product, and the results presented below are in this form. From the negative sign in the definition of the Reynolds stress, we define positive Reynolds stress if the uv product is negative. The average \overline{uv} being negative in the boundary layer represents production in the turbulent kinetic energy equation. If the average uv product is positive we have 'negative production' or dissipation of turbulent energy into the mean or into irreversible forms.

Figure 30 shows the amount of time spent in each of the four quadrants during the time that the structures

passed the probe. The major amount of time for all the structural configurations is spent in quadrant 2, which represents positive Reynolds stress. The distribution of quadrant times is roughly the same for all configurations.

The existance of quadrants 1 and 4 in the time that the structures pass indicates that significant vorticity is present. For only through vorticity is the lifting of high speed fluid and the wallward motion of low speed fluid normally created. As might be expected, the large scale sweep event shows the largest amount of time in quadrant 2, and little time in the other quadrants. Again, we say the large scale sweep is relatively irrotational.

Note that the negative rings have uv in quadrant 3 only 1 % of the time. This might be explained if the center of the bottom vortex was above the probe on average, as suggested by the ensembled signals. Then the lifting contribution, on the downstream side of the vortex, would be inducing flow in the streamwise direction, so that even though the fluid originates from a lower momentum region near the wall, the effect of the induction by the vortex shows a positive fluctuation in the streamwise velocity. This motion then contributes to quadrant 1 instead of quadrant 3.

The ensembled Reynold stress values in each of the quadrants for the positive rings, negative rings and the large scale sweeps are listed in Table 15. Notice that the largest absolute Reynolds stress occurs in quadrant 2 for all three of the structures. As stated above, the most time is spent in this quadrant also, so that all the structures have a net positive Reynolds stress associated with them. Quadrant 3 also contributes significantly to the positive Reynolds stress for the positive rings and the sweeps, but not for the negative rings. Quadrants 1 and 4 contribute very little to the total Reynolds stress associated with the structures.

It is interesting to examine the magnitude of the Reynolds stress averaged over quadrant 2. The mean uv product in the boundary layer at the measuring location was -0.0185 ft**2/sec**2. The standard deviation in the instantaneous uv values was 0.0381 ft**2/sec**2. For positive rings the ensembled instantaneous uv product in quadrant 2 was -0.0418 ft**2/sec**2. Hence, the ensembled uv product was 61 % of the standard deviation about the mean. In the ensembled sense this represents significant uv, and as discussed above possibly significant turbulence production.

The negative rings have an ensembled instantaneous uv product in Quadrant 2 of -0.0588 ft**2/sec**2. represents an ensembled average which is over a standard deviation about the mean. Therefore the negative rings certainly have a significant uv product associated with them. In section 5e which dicusses the ensembled signals, the streamwise velocity was entirely positive when the negative rings passed the probe. It was suggested above that the probe had passed below the center of the bottom vortex in the negative rings causing the u signal to be entirely positive, even though fluid was being lifted from the wall. We see from the quadrant analysis that the contribution to the uv product from quadrant 3, which represents the lifting of low speed fluid, is very low. is possible that some of the uv product classified into quadrant 1 is actually lifted fluid with an induced positive streamwise fluctuation.

The main result here is that the structures which create the pocket feature appear to have a significant net negative uv product associated with them. The quadrant analysis suggests that the average negative uv product results from strong sweep motions occurring for a major amount of time within the structures. If the assumption

discussed above is accepted, then the results indicate that the structures have a significant turbulence production associated with them.

The individual signals indicate that for some of the samples substantial lift-up of low speed fluid is created upstream of the positive rings, creating a very strong uv product. It should be noted that the signals used in the quadrant analysis include only the time of passage for the structures and therefore does not include the turbulence production which is caused by the interaction of the structures with the environment, but only that associated with the structure itself.

4 DISCUSSION

The results of this investigation are discussed below with respect to the relationship between the observed results and the hypothesis that vortex rings are the central element responsible for the pockets. The results are then compared with evidence regarding the bursting events. Finally, the uv quadrant breakdown results are compared with information regarding the net turbulence production in the boundary layer.

The results presented above indicate that there are two types of events associated with the disturbance of the sublayer fluid. It is possible to group these events into two catagories; large scale sweep events and small scale vortical events. These two observations appear to be quite different in nature and evolution. The large scale sweeps were not observed frequently, and involved spatial scales of over 200 viscous lengths which are quite large in

comparison to the pocket pattern. The five vorticity containing structures associated with the occurrence of pockets, can be grouped into one family of structures characterized by a length scale of about 100 viscous lengths, and containing high vorticity.

As stated above, incomplete visualization was involved with the observation of the type 1 structure, and the single vortices with the same sign and opposite sign of the mean vorticity in the boundary layer. In addition to incomplete visualization, there exists the possibility that the rotation of a vortex opposite in sign to the mean, which is part of a structure, may be essentially balanced by the rotation of the environment in which the structure exists. The fluid would not visually be observed to rotate in this case, which would not allow the structure to be classified as a vortex pair. In many cases where the rotation due to the vortex was not observed (type 1 structures and single vortices), the hot-wire signals were observed qualitatively to be very similar to those of the so-called ring configurations. The ensembled signals for the type 1 structure after removing three of the samples appears very similar to the ensembled signals for the positive ring. Hence, it is felt that the type 1 structure and single vortices possibly belong to the same structural forms that were termed positive and negative rings.

In the positive ring case, the evidence offered by this investigation does not conclusively support that the vortex pairs observed are part of a ring configuration. Although the validation of this description was not the objective of the study, the hypothesis would have been supported had the strength of the paired vortices been relatively equal and/or had high correlation in their dynamics been observed. In terms of the negative rings, the signals conclusively show the existence of the bottom vortex, but the top vortex never intersected the probe axis, so that strict confirmation of this configuration is impossible.

The visual data was much too complex to determine visually if the stretching of a single vortex line associated with the two vortices was occurring.

Furthermore, the measurements were made at a <u>single</u> point in space so that the signals could not be used to address this question. Therefore, at this time the description of these vortex pairs as vortex rings will be discontinued. The convention employed for the terms positive and negative will be retained, but the structures will be called

positive and negative vortex pairs.

The individual and ensembled normal velocity signals show a substantial positive peak at the proper core boundary of the proposed vortices. Also, the signal within the boundaries of the structure has a very high degree of coherency. Therefore, the normal velocity signal conclusively suggests that vortices are present. Since the spatial derivative dv/dx results directly from the v signal, the proper response is observed.

The response of the spatial derivative du/dy does not suggest the presence of two vortices for the positive pairs in a quantitative sense. However, as discussed in the results, if we accept that the local average velocity gradient is substantially less than the long time average, then the signals suggest that counter-rotating vortices exist, and their strength is of the same order. From these results it would appear that organized pairs of concentrated vortices are associated with the occurrence of the pocket feature in the sublayer, if this discrepancy in the average spatial gradient can be explained. At this time no sure explanation is known, so that the change in descriptive terms seems necessary.

One possible explanation for the observed difference

between the local average and long time average in the spatial gradient dU/dy, is supported by the observation of strong shear layers by many investigators (Offen and Kline (1973), Corino and Brodkey (1969)). In this study, strong inclined shear layers were in general observed frequently. Focusing on the causal structures, an inclined shear layer was often observed at the interface between the high speed fluid being induced by the positive vortex pairs and the relatively low speed fluid under the structure. This shear layer was indicated by a very strong positive peak in du/dy in phase with a positive peak in du/dt, marking the passage of an interface between low speed fluid and high speed fluid. The strength of the du/dt peak was about 1 - 2 standard deviations, and usually little response in dv/dx was observed. This shear layer was well correlated with the visual boundary between the low marker density fluid of the high speed region, and the high marker density fluid of the low speed region. A strong shear layer was also seen at the interface of the type 1 structure, and a few times associated with the negative vortex pair.

In comparison to these shear layers, the strength of the vortices associated with the causal structures is low, by a factor of 2 or more in the du/dy response. In this study, the peaks in du/dy corresponding to the passage of inclined shear layers were sometimes of the order of 50 - 100 l/sec. This is from 2 to 5 times the standard deviation of 21.1 l/sec. observed in du/dy. The skewness factor in the spatial gradient du/dy was 0.83.

Because the fluctuation in vorticity associated with the vortical structures is relatively low, the distribution in du/dy is skewed in the positive direction by the shear layer responses. The result is that the average shear that the vortices exist within is actually lower than the long time mean, which is strongly effected by these large positive peaks in du/dy. The response in dv/dx was usually not effected by the shear layers.

If vortex pairs existed in an otherwise constant shear flow, the dU/dy distribution would appear as in Figure 31a. The mean dU/dy would remain identical to the constant shear value. If we now add strong positive peaks in dU/dy as created by the passage of a strong shear layer, then the mean of dU/dy is increased to the dotted line in Figure 31b, although the 'average' dU/dy which the vortices contend with is still at the solid line.

It appears possible that the strength of the peaks in du/dy associated with the shear layers are large enough to

make the long time mean substantially different from the local average. This could explain the observation that the vorticity determined by the simple subtraction of the spatial derivatives was dominated by the du/dy signal.

The data as it stands, indicates that very high levels of vorticity of the opposite sign to the mean vorticity would be associated with these structures. Therefore, even if the long time mean is considered to be representative of the background shear, the events identified in this study must be be classified as having concentrated vorticity.

With the local average in du/dy employed, the fluctuations in the spatial derivatives du/dy and dv/dx are seen to be of the same order. The fluctuations in the spatial derivatives associated with the structures identified would then indicate the presence of vortex pairs. This implies that these isolated vortices had significant strength and coherency during the times that they were sampled, adding weight to our hypothesis that vortex induced interactions with the wall region fluid are responsible for the formation of pockets, and reopens the consideration of what configuration they have.

It is also possible that due to this averaging effect, the identification of isolated vortices using probe

measurements has been corrupted in the past by the truncation of the signals with the long time mean. The interface between the high and low speed fluid is of small scale, so that the peak in dU/dy associated with the shear layer becomes very prominent, compared to the larger scale and weaker motions involved with the vortical structures. Hence, the dU/dy responses corresponding to the shear layers dwarf those associated with the vortical structures. In conclusion, the long time mean of dU/dy is not representative of the 'average' shear in which the coherent structures exist.

Offen and Kline (1973) investigated the relationship between the outer flow and the bursting events using visualization and measurements, concluding that nearly every burst is associated with a sweep. They observed that the lift-up of low speed fluid was preceded by a disturbance moving toward the wall, and that the ejection processes were triggered by this wallward moving fluid, or sweep. The sweeps move wallward ahead of the bursting fluid and proceed to spread out. In addition, they observed a high shear layer above the wall as the disturbance to the sublayer began.

They suggest the scale of the sweep is approximately 100 x+, and represent vortical motions. Furthermore, they observed that all lift-ups were associated with vortical patterns in the hydrogen bubble time lines. Their data suggests that a mean vortex causes the sweep motion. They state that they frequently observed vorticity opposite to the mean.

Hence, it appears that the data of this study is in agreement with that of Offen and Kline, in the sense that both their results and the results of this study, show that events with a scale of about 100 viscous lengths, containing concentrated vorticity, are involved with the disturbance of the wall region fluid.

Offen and Kline investigated the bursting process which heavily involves the lift-up of low speed fluid, so that it is not unreasonable to assume that their attention was focused on this lift-up. There is essentially little lift-up upstream of the vortex pairs in the initial stages. For several events observed in the later stages, the upstream vortex of the positive vortex pair strengthened, possibly due to stretching, and very strong lift-up of larger scale was observed, extending upstream of the structure. The Reynolds stress associated with this

lift-up was seen to be as large or larger than that associated with the sweep motion induced by the vortex pairs. As the process continued the Reynolds stress in the lifted fluid became much stronger than in the sweep fluid, as the strength of the vortices diminished. There was lift-up associated with some of the negative vortex pairs, but in general did not appear as strong as with the positive vortex pairs. However, this does not mean the pocket formed as the result of a negative vortex pair does not include lift-up in its later stages as it interacts with the oncoming flow.

The majority of events that would strike the measuring probe over a long period of time will be somewhere in the later stages. The events corresponding to early stage pockets were used in this study, so that we do not expect to observe this lift-up in our data. The observations described above suggest that the events we have identified would correspond to the observations of Offen and Kline if they were allowed to continue their development. Offen and Kline state that even events without observed lift-up showed vorticity near the wall.

As mentioned earlier, a strong shear layer was often observed at the downstream boundary of the positive vortex

pair structures, in agreement with Offen's observation of a high shear layer as the disturbance appeared.

In conclusion, the results suggest that the flow fields identified in this study may be responsible for the initiation of the bursting event.

Corino and Brodkey (1969) presented the results of detailed observations very near a wall in turbulent pipe flow using suspended particles for visualization, which gives information about the interaction between the wall layers and the flow above the wall. Their view extended from approximately the wall to y+ = 40, and covered about 63 x+. They stated that the sublayer was periodically disturbed by fluid elements which penetrated into the region from positions above the wall. They describe a series of events which are to be representative of the bursting process.

The observation began with a local decelerated region of the order of 30 y+, the extent of which varied from perceptably small to their entire view. Then an accelerated region moved towards the wall, entering at about y+=15. This fluid was usually seen to move roughly parallel to the wall at y+ = 15. Following the appearance of the accelerated region, the ejection of low speed fluid

from the wall (at 5<y+<15) was observed. They found that the ejection occurred immediately after the start of the acceleration and always occurred before the entire region was accelerated. They found that the ejection motions proceeded rapidly to the developed stage, in a varying amount of time, and then gradually ceased. Again, they also observed sharp shear layers on the upstream face of the ejected fluid.

The major difference between these observations and those of Offen and Kline is that the accelerated region or sweep occurs after, or at least simultaneously with the ejection motions. Falco (1979) offers an explanation of this observation. He proposes that if the side view employed in Corino's visualization is located through the sides of staggered pockets, then the events observed can be explained. That is, the decelerated region corresponds to the lifted side of a pocket, and the sweep motion corresponds to the wallward motions creating the second pocket, which is located upstream and staggered with respect to the first pocket. In support of this, is the observation that the majority of pockets occur in a staggered configuration.

As mentioned earlier, the pockets which were centered,

or quasi-centered with respect to the probe axis were concentrated on in the data analysis of this study. Again, this was done because of the observed complexity in the flow structure above the wall when pockets occurred off-center. Hence, the majority of events which were studied in this investigation would not contain the staggered effect. Therefore, it seems reasonable that lift-ups were usually associated with the upstream side of the vorticity containing structures in this study, which is correlated with the upstream boundary of the pockets. In addition, as stated in the results, lift-up of low speed fluid was at times observed at the downstream side of the positive vortex pairs, but lower Reynolds stress was associated with this lift-up.

Hence, we find that the observations of Corino and Brodkey do correlate to some degree with the observations of this study. The scale of the accelerated regions suggested by the view dimensions in Corino's experiment is of the order of 100 viscous lengths. The agreement here also implies that the structures identified are responsible for initiation of the ejection events and turbulence production process.

The above discussion shows that the observations of this investigation fit closely with the observations of Offen and Kline (1973) and Corino and Brodkey (1969), which are two of the major works involved with the interaction between inner flow and outer flow with respect to the burst event. In the last several years, the structural characteristics and processes involved with the pocket flow module have been investigated by Falco (1977b, 1978, 1979, 1980), and several closely related hypothesis have been offered. The average spanwise scale of the pocket pattern is 100 z+ (Falco 1977b) which agrees with the streak spacing of the sublayer (Kline (1965)).

Falco (1978) found that pockets were associated with large contributions of Reynolds stress when they formed in early stages. Falco (1979) discussed how the events associated with the occurrence of pockets explains the formation of low speed streaks, streamwise vortices, lift-up of sublayer fluid, oscillation or flapping of the lifted fluid and the following break-up. It then appears that the pocket is 'the footprint' of the bursting process. Kim et al. (1968) found that 70 % of the total production occurs during the ejection phase of the bursting process. Therefore, the pocket appears to be a feature of the major

mechanism associated with the production of turbulence in the wall layers of bounded turbulent shear flows.

Falco (1980) presented signals characteristic of those observed above pockets at y+ = 16, for the five stages of evolution of the pocket. He suggests that the appearance of a pocket begins with high negative uv resulting from the initial sweep. This is confirmed by the results of this study which are presented for the early stages, and also shows high negative uv above the pocket. In addition, Falco found very high correlation between the passage of the pocket and significant perturbations in the signals of uv, du/dx, du/dy and dv/dx. This is comparable to the results of this study, where a very high correlation was observed between the strongest responses in the signals v, uv, du/dy, dv/dx and du/dt, and the passage of structures which were identified with pocket occurrence.

The characteristic signals presented by Falco (1980) are in terms of the conditionally averaged quantity relative to the mean (e.g. $(\langle uv \rangle - \overline{uv}/\overline{uv})$). For his stage 1, he found a relative uv peak of about -10.0. The data of this study shows a relative uv peak of the order of -2.0. The data of Falco (1980) was measured at y+ = 16, so that the fluctuations which are caused by these structures might

be expected to be of a higher relative value. The relative fluctuating streamwise velocity peak found by Falco has a peak value of 0.4, and in this study we find about 0.2. Finally, the relative du/dy peak shown is about -0.8, and in this study we have about -1.0. These comparisons show that the relative intensity of the velocity fluctuations are smaller at our measuring location, but that the relative shear is larger.

Falco (1977c) showed that the interaction of a laminar vortex ring convecting at a shallow angle towards a wall marked with powder results in a pocket shaped pattern on the wall, and induces the wall layer fluid away from the wall. Falco (1977b) suggests that the pocket pattern in the boundary layer results from vortex ring/wall interactions.

There exists evidence of the presence of vortex ring-like structures in the boundary layer, which suggests that ring/wall interactions could be responsible for the formation of pockets in the boundary layer. Falco (1974, 1976, 1977a) found compact vortical structures termed 'typical eddies' in the outer region of the boundary layer, located on the upstream face of the large scale motions. Falco (1977a) found the length scale of the 'typical

eddies' to be approximately 100 l+. These eddies have the same visual characteristics and orientations as the negative vortex pairs identified in this study. The data also showed that a stagnation point flow field was created at the upstream face of the large scale motions, which would push the typical eddies located under the stagnation streamline toward the wall. Hence, there appears to be a mechanism for causing the vortical structures observed in the outer flow to interact with the wall.

The structures identified here, which are closest to the description of typical eddies are the negative vortex pairs. The ensembled signals for the negative vortex pairs indicate that the negative vortex pair structures may be associated with a relatively irrotational large scale downflow. The signals show a high speed region with significant wallward motion extending upstream of the structure for about 100 viscous lengths, with a low level of vorticity. This is what one would expect to see behind the structure if it was being forced downward by a large scale stagnation flow from above.

The objective of this investigation was to identify the flow conditions and structural features above the wall responsible for the formation of pockets. The results of this study clearly show that the presence of concentrated coherent transverse vortices above the wall, near the pocket centerline as observed in the x-y plane, are responsible for the formation of the pocket feature. This is shown by the strength and coherency of the normal velocity and the spatial derivatives dv/dx and du/dy. The data suggest that both positive and negative vortex pairs are associated with the pocket phenomenon.

The vorticity induced downward motion associated with these structures is seen to be the sweep motion directly responsible for the pocket pattern, and the sweep observed by other investigators. These sweeps are of the order of 100 wall layer units, and are small scale with respect to the large scale motions of the boundary layer. The vortices induce a stagnation point flow field at the wall, which produces the pocket pattern and creates high Reynolds stress near the wall. The ejection motions appear to be closely related to these structures, in that the ejetion motions appear to be involved with the interactions that the vortical structure initiates. The pocket has already been shown to be highly correlated with the production of turbulence in the wall layers (Falco (1980)), so that the results of this study show that the production process is

governed by interactions of vorticity on the microscale with the wall and surrounding flow.

As it became evident that vortex pairs were involved with the occurrence of pockets, the terminology used to describe the vortex pairs as vortex rings was adopted. discussed earlier in this Chapter, this terminology is discontinued, pending further investigation of the observed conditional average in the spatial derivative dU/dy, and further visual investigation of the structure. However, it is apparent from the visual data of this study, and the data of other investigations, that these vortex pairs as evidenced here, are most likely closed vortical structures. The aspect ratio of the pocket pattern is probably the strongest evidence of this. That is, if the vortices associated with the pockets had vortex lines extending in the transverse direction, then some pocket patterns would also have a correspondingly larger dimension in the transverse direction. This has not been observed.

The conditionally averaged Reynolds stress from the uv quadrant analysis indicates that the vortical structures identified in this investigation are a major contributor to the overall Reynolds stress in the boundary layer near the

wall. Brodkey et al. (1973b) present a quadrant breakdown of the uv signal in the wall regions measured over a long time in a turbulent boundary layer. Their data is compared with our results of a quadrant breakdown for the uv signal, observed only during the time that the identified structures pass the probe. The results of this comparison are tabulated in Table 16.

For reference, quadrant 1 corresponds to his outward interaction, quadrant 2 corresponds to the sweep motion, quadrant 3 the ejection motion and quadrant 4 to the wallward interaction. The number in parenthesis is the percentage of the value given in Brodkey et al. (1973b).

The comparison shows that uv during the sweep motions is over 3 times the long time average. This indicates that the induced sweep of these structures is a major contributor to the overall Reynolds stress associated with sweeps. Only the ejection motions associated with direct vorticity induced lift-up by the indentified structures is included in our results. In other words, the data used in our results includes the upward motion within the identified core only. From Table 16, we see that this contibutes significantly to the overall ejection average for the positive vortex pairs, but not for the negative

vortex pairs. Table 16 also shows that the identified structures contribute strongly to the io and iw motions, confirming the existence of substantial vorticity.

Comparison of the % time in each of the quadrants indicates the sweep motions are strongly involved with the identified structures, whereas the ejection motions are not. This corresonds to the observations mentioned above, where it was stated that the strong ejections occurred following the structure or as an indirect response to the disturbance created by the structures. Interestingly, the percent of time spent in the interaction quadrants, which suggests vorticity, is essentially the same as for the long time.

The next comparison represents the 'average uv signal only when the flow passing the probe is in a particular quadrant'. These results show that all the quadrants have a larger average that the long time average, implying that the contributions from these structures are important. The interaction quadrant results indicate that a substantial contribution to these motions is made by the identified structures. The observation of several forms of sweep motions, such as the large scale sweeps, explains the relatively lower average for quadrant 2. The maximum

upward normal velocity was usually reached at the core boundary of the vortices, meaning the small amount of ejection motion observed does quantitatively appear large, and then is divided by a small % time, which might explain the large average for quadrant 3. Finally, we see that the average duration for the sweep motions is longer than the long time average, and shorter for the ejection motions.

This comparison shows that the identified structures have substantial Reynolds stress associated with them, residing mainly in the form of sweep motions with strong Reynolds stress. The data indicates that a large portion of the interaction motions are involved internally with these coherent structures. Hence, the structures themselves contribute substantially to the turbulence production in the wall layers.

5 CONCLUSIONS

The results presented above show that concentrated vorticity on scales of the Taylor microscale is highly correlated with the occurrence of the pocket pattern in the wall region of turbulent boundary layers. The results indicate that concentrated vorticity contained within structures moving toward the wall, with length scales of approximately 100 viscous lengths, induce the sweep motions that are related to the initial phases of the burst event. The vorticity induces a downflow, creating a stagnation flow at the wall which initiates the pocket feature. Furthermore, the structures contain entirely high speed fluid, and there is significant positive Reynolds stress associated with the identified structures.

The fluctuating vorticity signal was observed to be dominated by the response in the spatial gradient du/dy during the passage of vorticity containing events. The response in du/dy was observed to be a factor of 2.0 or

more larger than the response in dv/dx when vorticity containing structures passed the measuring probe. It is possible that the skewed nature of the du/dy signal causes the long time mean in du/dy to be substantially different from the local mean in du/dy during passage of the vorticity containing events. This would explain the relationship between the magnitudes in the spatial gradients du/dy and dv/dx.

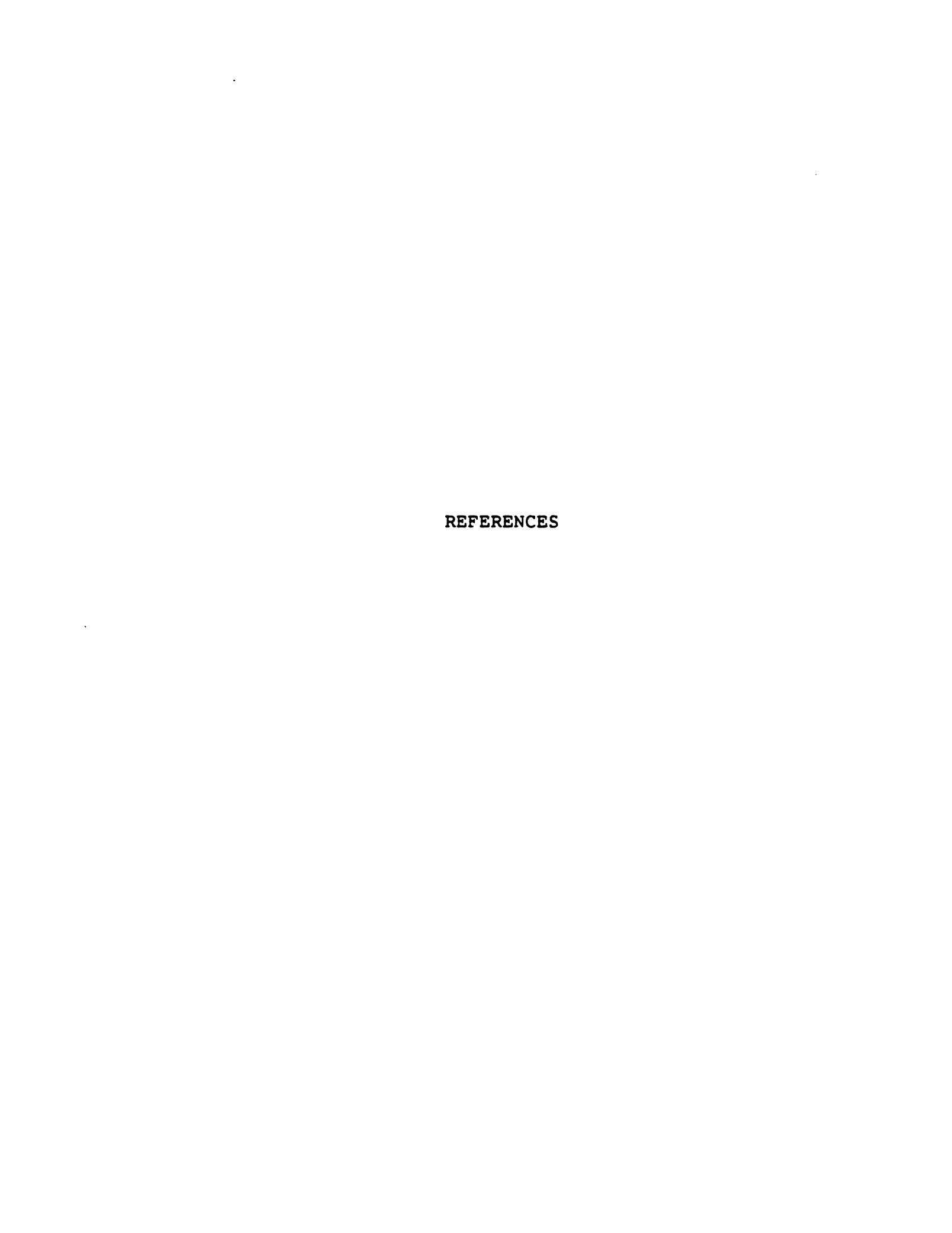
The results suggest that the vorticity is contained in counter-rotating transverse vortex pairs, observed along the axial centerline of the pocket. The vortex pairs are seen in two configurations, classified by the direction of the flow induced between the vortices. The vortex pairs with flow induced in the streamwise direction have, on average, an initial maximum Reynolds stress of about twice the long time mean. The maximum streamwise velocity fluctuation is, on average, approximately 0.75 standard deviations. The maximum normal velocity fluctuation is, on average, approximately 1.1 standard deviations. The vorticity associated with the structure is largely positive, with a maximum value of approximately 1.0 standard deviation on average. The spatial gradient dv/dx has, on average, two peaks of over 1.1 standard deviations,

corresponding to the vortices. The fluctuation in the spatial gradient du/dy observed between the boundaries of the structure, is of the same order as the fluctuation in dv/dx.

The vortex pairs with flow induced opposite to the streamwise direction have, on average, an initial maximum Reynolds stress of about 2.5 times the long time mean, or about a standard deviation about the mean. The maximum streamwise velocity fluctuation is, on average, approximately 0.85 standard deviations. The maximum normal velocity fluctuation is, on average, approximately 1.7 standard deviations. A strong positive peak in the vorticity is associated with the structure, with a maximum value of approximately 1.5 standard deviations on average. The spatial gradient dv/dx has, on average, one peak of over 1.4 standard deviations, corresponding to a single vortex with sign opposite to the mean vorticity in the boundary layer.

The intensity level of all the velocity and derivative signals associated with the structures were seen to decrease with time after the interaction with the wall and sublayer fluid began.

Ensemble averaging of the signals observed as the identified structures passed the probe indicate that sample sizes of the order of 20 provide significant statistical convergence for the initial stage events.



REFERENCES

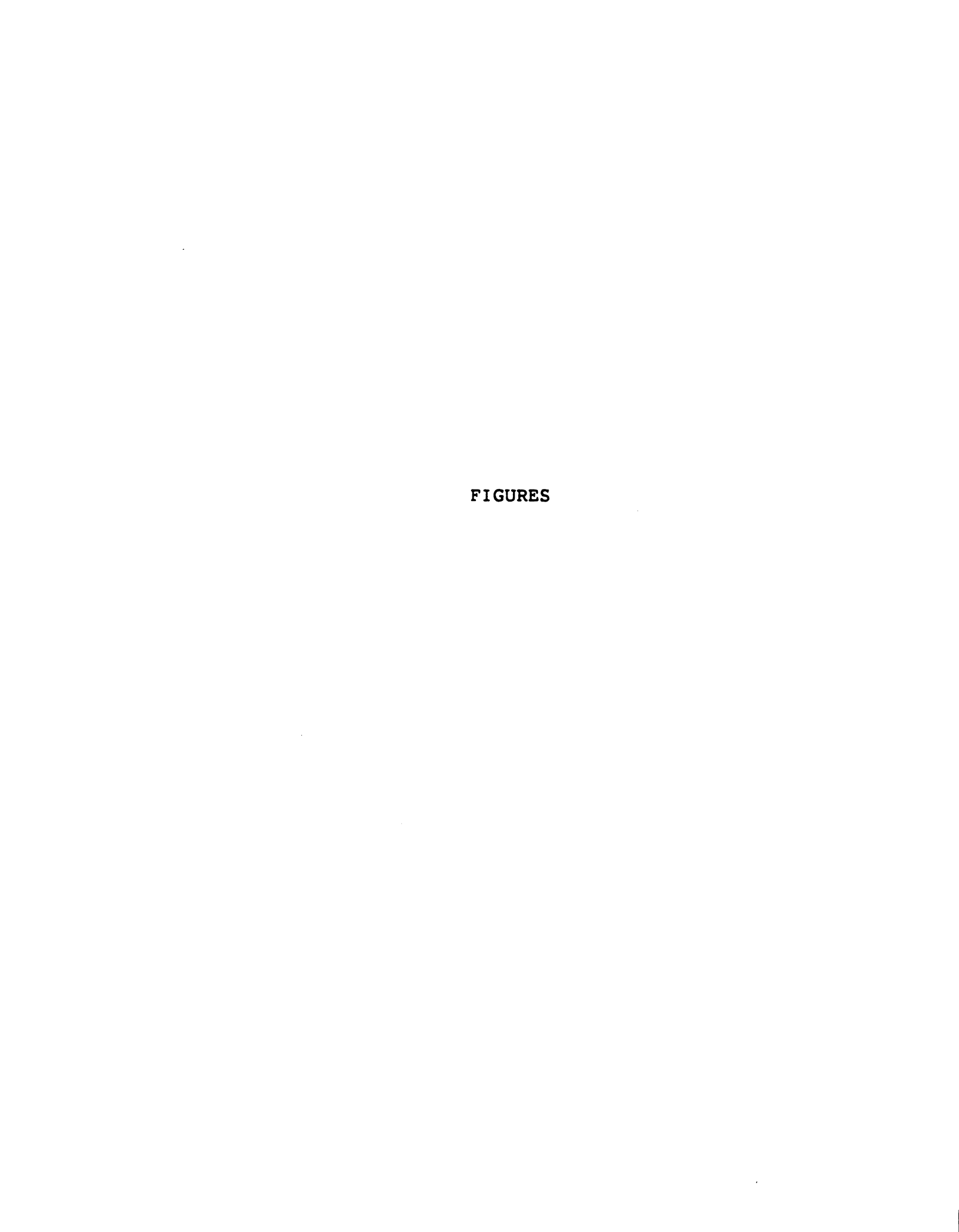
- 1. Bakewell, H. P., and Lumley, J. L., "Viscous Sublayer and Adjacent Wall Region in Turbulent Pipe Flow", Phy. of Fluids, 15, 1967, pp. 1880.
- 2. Blackwelder, R. F., and Kaplan, R. E., "The Intermittent Structure of the Wall Region of the Turbulent Boundary-Layer", Univ. So. Calif., Rep. USCAE 1-22, 1972.
- 3. Brodkey, R. S., Nychas, S. G., Taraba, J. L., and Wallace, J. M., "Turbulent Energy Production, Dissipation, and Transfer", Phy. of Fluids, Vol. 16, No. 11, 1973a, pp. 2010.
- 4. Brodkey, R. S., Wallace, J. M., and Eckelmann, H., "Some Properties of Truncated Turbulence Signals in Bounded Shear Flows", Max-Planck-Inst. fur Stromungsforschung, Gottingen, No. 113, 1973b.
- 5. Brown, G. L., Thomas, A. S. W., "Large Structure in a Turbulent Boundary Layer", Phy. of Fluids, 20, Pt. II, 1977, pp. S243.
- 6. Clauser, F. H., Advances in Appl. Mechanics, 4, 1956.
- Coles, D., and Van Atta, C. W., "Digital Experiments in Spiral Turbulence", Phys. of Fluids, Suppl., Part II, 10, 1967.
- 8. Corino, E. R., and Brodkey, R. S., "A Visual Investigation of the Wall Region in Turbulent Flow", J. Fluid Mech., Vol. 37, 1969, pp. 1-30.

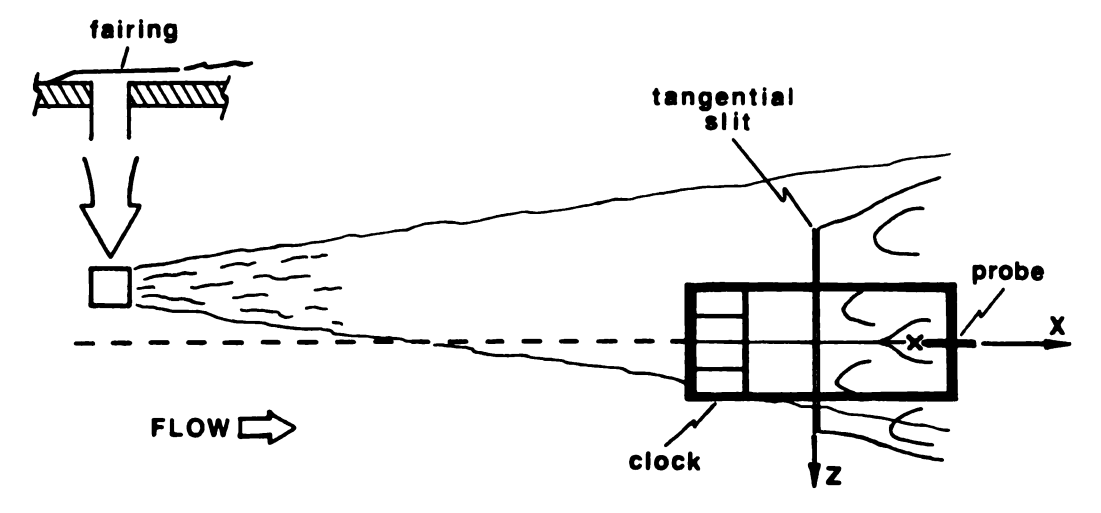
- 9. Corrsin, S., and Kistler, A. L., Natl. Advisory Comm. Aeronaut. Tech. Notes No. 3133, 1954.
- 10. Doligalski, T. L., and Walker, J. D. A., "Shear Layer Breakdown Due to Vortex Motion", Proc. Workshop on Coherent Structure in Turbulent Boundary Layers", Lehigh University, 1978.
- 11. Eckelmann, H., Mitteilungen Max-Planck-Inst. fur Stromungsforschung, Gottingen, No. 48, 1970.
- 12. Eckelmann, H., Nychas, S. G., Brodkey, R. S., and Wallace, J. M., "Vorticity and Turbulence Production in Pattern Recognized Turbulent Flow Structures", Phy. of Fluids, Vol. 20, No. 10, Pt. II, 1977.
- 13. Emmons, H. W., J. Aeronautical Sci., 18, 1951, pp. 490.
- 14. Fage, A., and Townend, H. C. H., Proc. Roy. Soc. London, 135, 1954, pp. 656.
- 15. Falco, R. E., "Large Scale Motions in the Inner Region of the Turbulent Boundary Layer", Bulletin Am. Phys. Soc., Vol. 20, No. 11, 1975, pp. 1430.
- 16. Falco, R. E., "Coherent Motions in the Outer Region of Turbulent Boundary Layers", Phy. of Fluids, Vol. 20, Part II, 1977a.
- 17. Falco, R. E., "A Structural Model of the Turbulent Boundary Layer", Proc. of the 14th Annual Mtg. of Soc. of Engrg. Sci., 1977b.
- 18. Falco, R. E., "Vortex Ring/Wall Interactions in Still and Moving Ambients", Bulletin Am. Phys. Soc. Series II, Vol. 22, 1977c, pp. 1277.
- 19. Falco, R. E., "Wall Layer Structure of Turbulent Boundary Layers", Bulletin Am. Physical Soc., Series II, Vol. 23, 1978, pp. 1000.

- 20. Falco, R. E., "Structural Aspects of Turbulence in Boundary Layer Flows", Proc. of Sixth Biennial Symposium on Turbulence, 1979.
- 21. Falco, R. E., "Combined Simultaneous Flow Visualization/Hot-Wire Anemometry fot the Study of Turbulent Flows", ASME Journal of Fluids Engrg., Vol., 1980a.
- 22. Falco, R. E., "The Production of Turbulence Near a Wall", AIAA 13th Fluid & Plasma Dynamics Conf., 1980.
- 23. Falco, R. E., and Lovett, J. A., "The Scaling of Wall Region Structure", To be submitted to Physics of Fluids.
- 24. Gupta, A. K., Laufer, J., and Kaplan, R. E., "Spatial Structure in the Viscous Sublayer", J. Fluid Mech., 50, 1971, pp. 493.
- 25. Hama, F. R., Soc. Naval Architects Marine Engrs. Trans., 62, 1954, pp. 333.
- 26. Kim, H. T., Kline, S. J., and Reynolds, W. C., "An Experimental Study of Turbulence Production Near a Smooth Wall in a Turbulent Boundary Layer with Zero Pressure Gradient", Report MD-20, Dept. of Mech. Engrg., Stanford Univ., Stanford, CA., 1968.
- 27. Kim, H. T., Kline, S. J., and Reynolds, W. C., "The Production of Turbulence Near a Smooth Wall in a Turbulent Boundary Layer", J. Fluid Mech., 50, 1971, pp. 133.
- 28. Klebanoff, P. S., Natl. Advisory Comm. Aeronaut. Tech. Notes No. 3178, 1954.
- 29. Kline, S. J., Reynolds, W. C., Schraub, F. A., and Runstadler, P. W., "The Structure of Turbulent Boundary Layers", J. Fluid Mech., 30, 1967, pp. 741.
- 30. Kline, S. J., and Runstadler, P. W., "Some Preliminary Results of Visual Studies of the Flow Model of the Wall Layers of the Turbulent Boundary Layer", J. Applied Mech., 26, 1959, pp. 166.

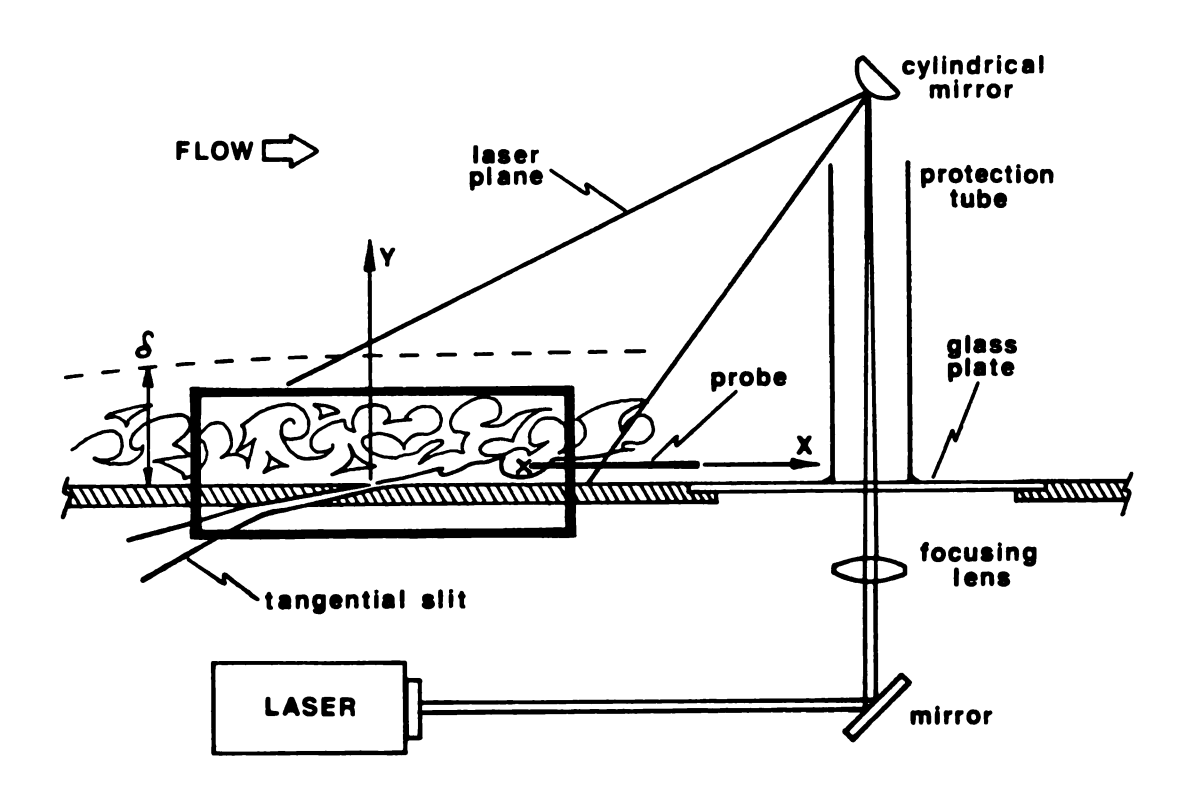
- 31. Kovasznay, L. S. G., Kibens, V., and Blackwelder, R. F., "Large-scale Motion in the Intermittent Region of a Turbulent Boundary Layer", J. Fluid Mech., 41, 1970, pp. 283.
- 32. Landahl, M. T., "A Wave-guide Model for Turbulent Shear Flow", J. Fluid Mech., 29, 1957, pp. 441.
- 33. Lilley, G. M., College Aeronaut. Cranfield, Co A Rep. 133, 1960.
- 34. Mitchner, M. J., J. Aeronaut. Sci., 21, 1954, pp. 350.
- 35. Offen, G. R., and Kline, S. J., "Experiments on the Velocity Characteristics of 'Bursts' and on the Interactions Between the Inner and Outer Regions of a Turbulent Boundary Layer", Report MD-31, Dept. of Mech. Engrg., Stanford Univ., Stanford, CA., 1973.
- 36. Offen, G. R., and Kline, S. J., "A Proposed Model of the Bursting Process in Turbulent Boundary Layers", J. Fluid Mech., 70, 1975, pp. 209.
- 37. Purtell, L. P., Klebanoff, P. S., and Buckley, F. T., "Turbulent Boundary Layer at Low Reynolds Number", Phy. of Fluids, Vol. 24, No. 5, 1981.
- 38. Runstadler, P. W., Kline, S. J., and Reynolds, W. C., "An Experimental Study of the Flow Structure of the Turbulent Boundary Layer", Report MD-8, Dept. of Mech. Engrg., Stanford Univ., Stanford, CA., 1963.
- 39. Schraub, F. A., and Kline, S. J., "A Study of the Structure of the Turbulent Boundary Layer with and without Longitudinal Pressure Gradients", Report MD-12, Dept. of Mech. Engrg., Stanford Univ., Stanford, CA., 1965.
- 40. Schubauer, G. B., "Turbulent Processes as Observed in Boundary Layer and Pipe", Journal of Applied Physics, 25, Part 1, 1954, pp. 188.
- 41. Schubauer, G. B., and Klebanoff, P. S., N.A.C.A. Tech. Note No. 3489, 1955.

- 42. Tennekes, H., and Lumley, J. L., "A First Course in Turbulence", The M.I.T. Press, London, 1972.
- 43. Townsend, A. A., "The Structure of Turbulent Shear Flow", second edition, Cambridge University Press, 1976.
- 44. Ueda, H., and Hinze, J. O., "Fine-structure Turbulence in the Wall Region of a Turbulent Boundary Layer", J. Fluid Mech. 67, 1975, pp. 125.
- 45. Wallace, J. M., Eckelmann, H., and Brodkey, R. S., "The Wall Region in a Turbulent Shear Flow", J. Fluid Mech., 54, 1972, pp. 39.
- 46. Wallace, J. M., Brodkey, R. S., and Eckelmann, H., "Pattern Recognized Structures in Bounded Turbulent Shear Flows", J. Fluid Mech., 83, 1977, pp. 673.
- 47. Willmarth, W. W., and Bogar, T. J., "Survey and New Measurements of Turbulent Structure Near the Wall", Phy. of Fluids, Vol. 20, No. 10, 1977, pp. 59.
- 48. Collis, D. C., and Williams, M. J., "Two-dimensional Convection from Heated Wires", J. Fluid Mech., 6, 1959, pp. 357.





a) Top View or Plan View



b) Side View of X-Y Plane

Figure 1. Two Views of Split View Motion Picture.

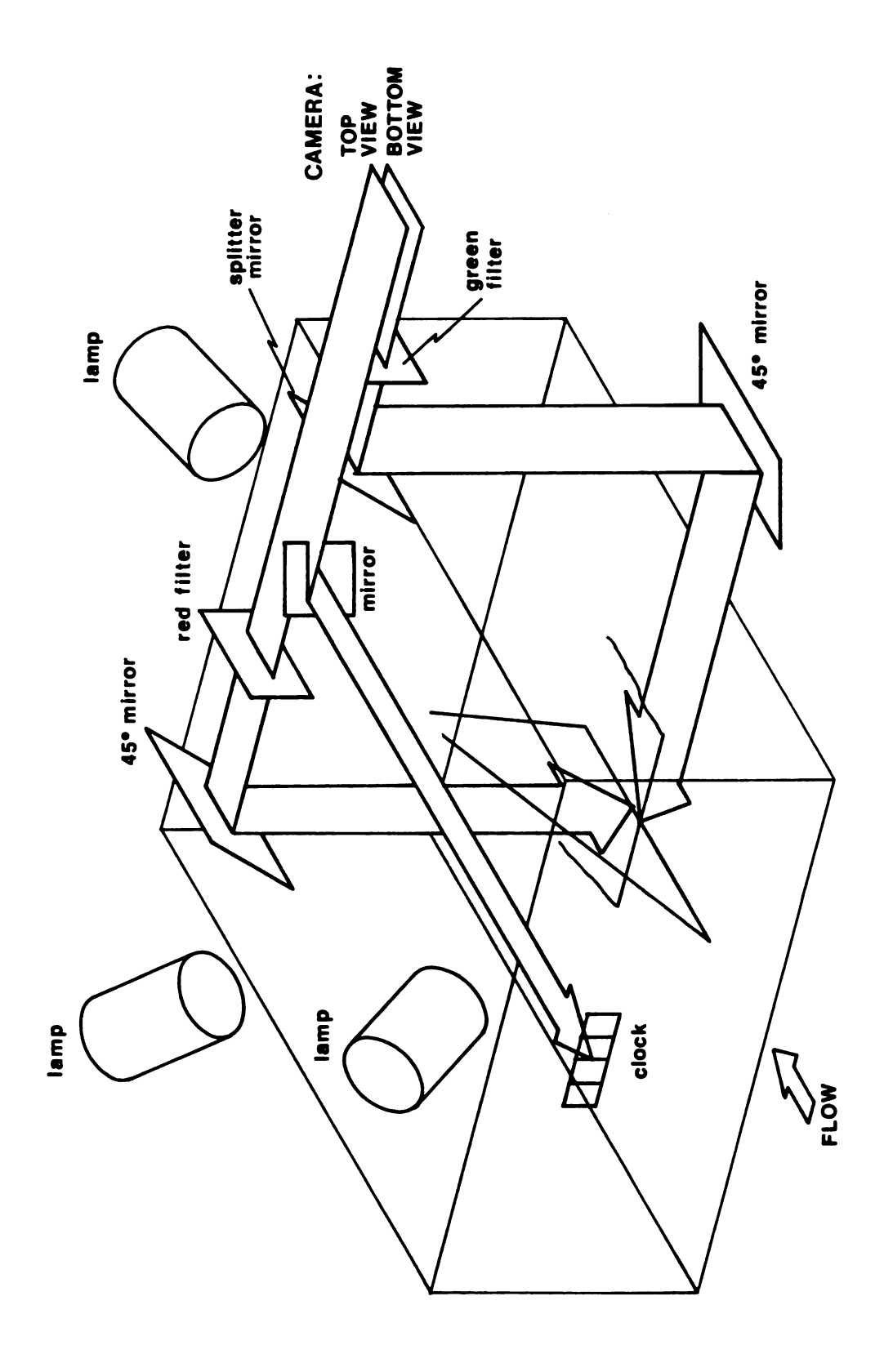


Figure 2. Mirror and Filter Arrangement.

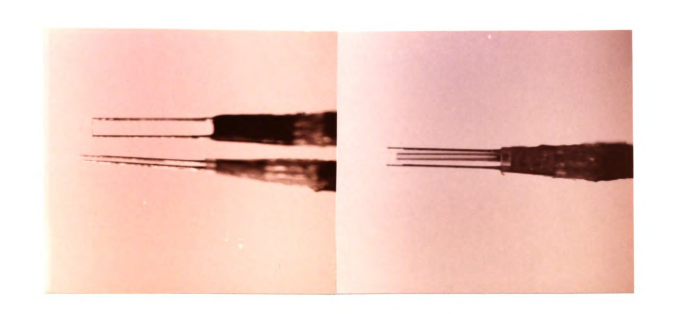




Figure 3. Four Element Vorticity Probe.



Figure 4. Experimental Equipment.

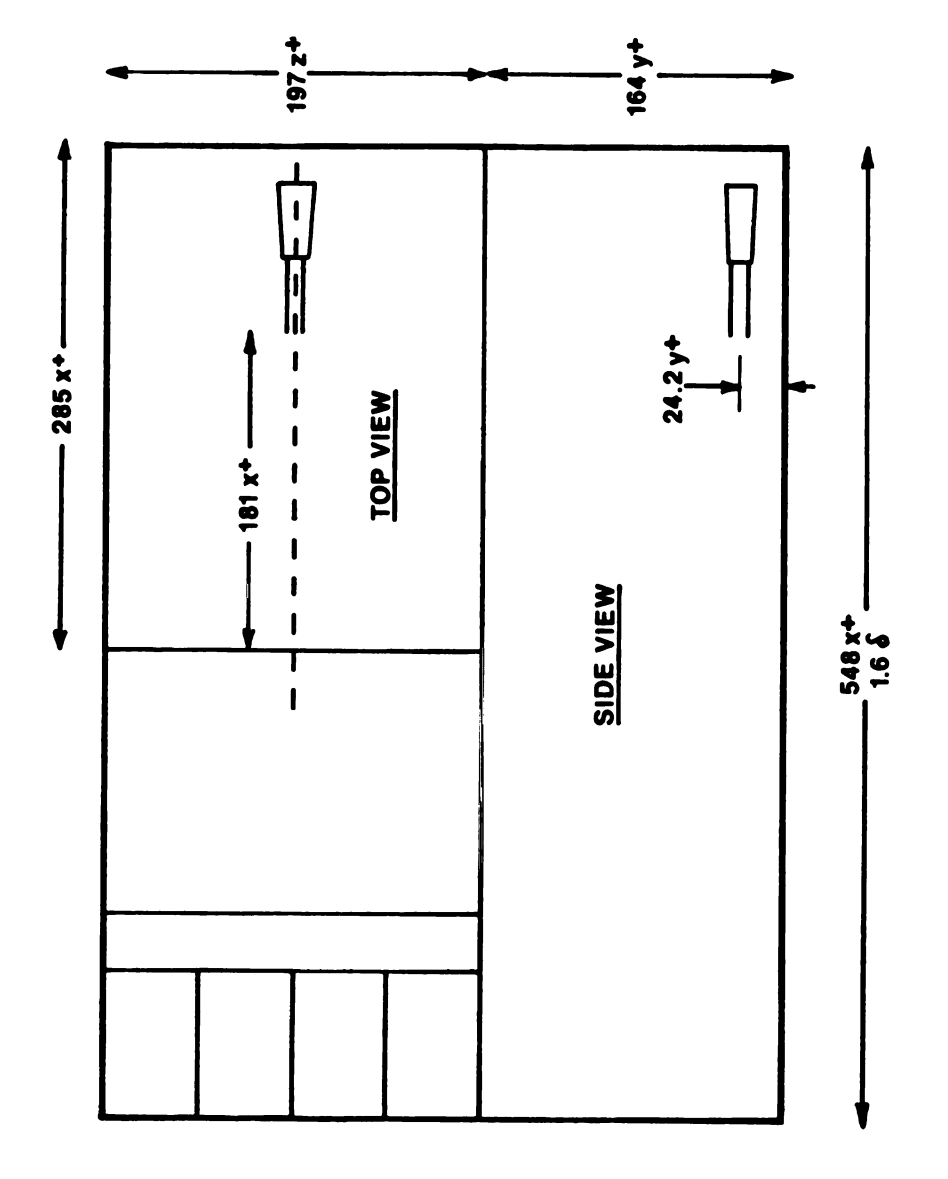


Figure 5. Motion Picture View Dimensions.

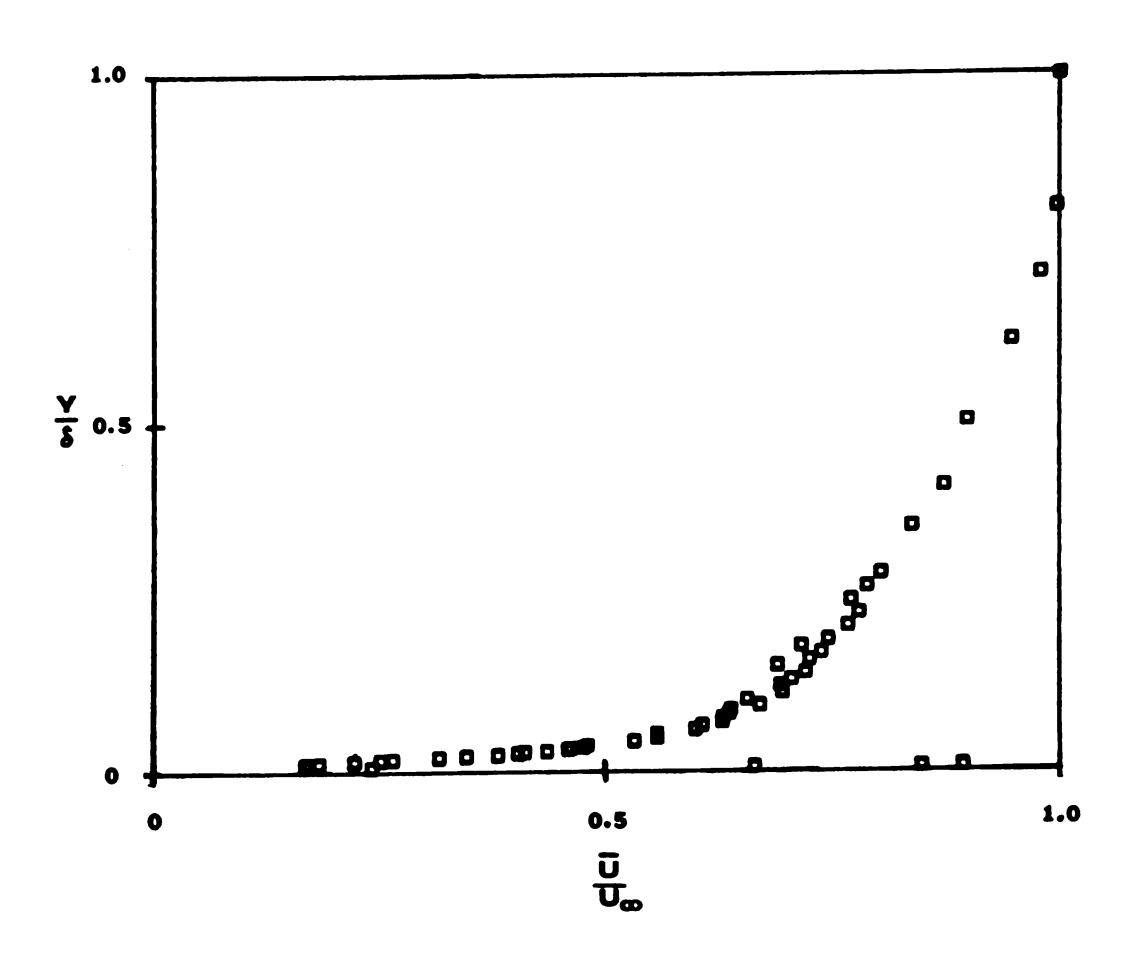


Figure 6. Linear Velocity Profile

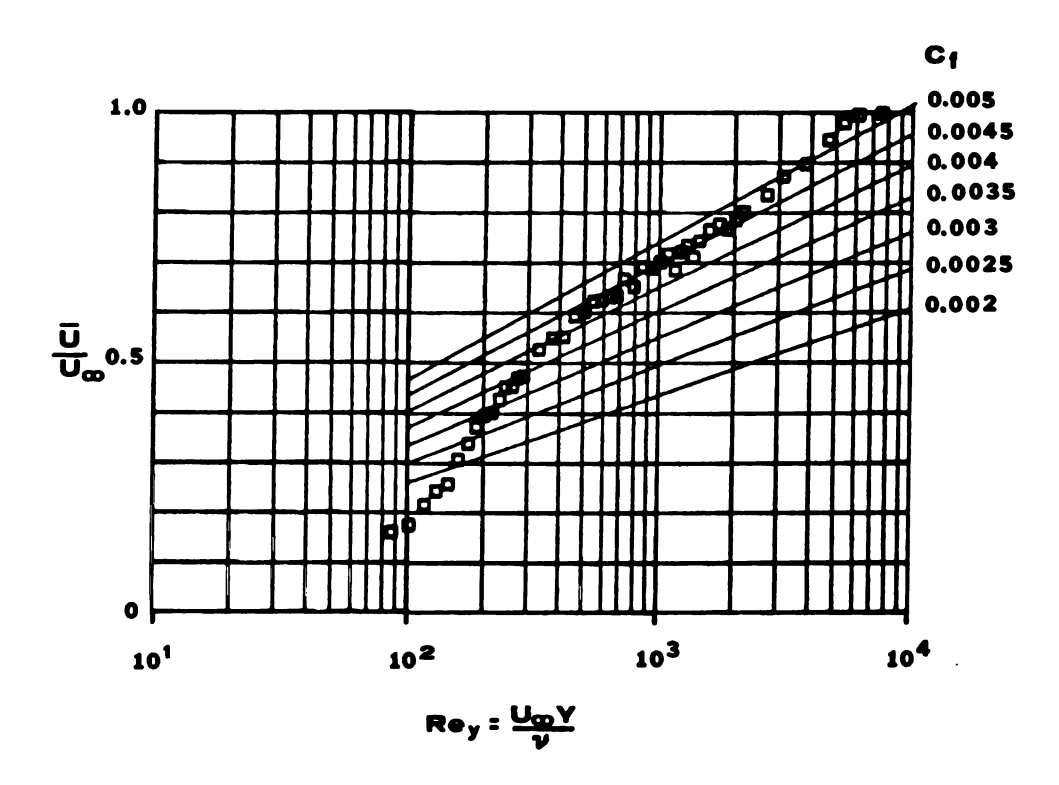


Figure 7. Average Velocity vs. Reynolds Number

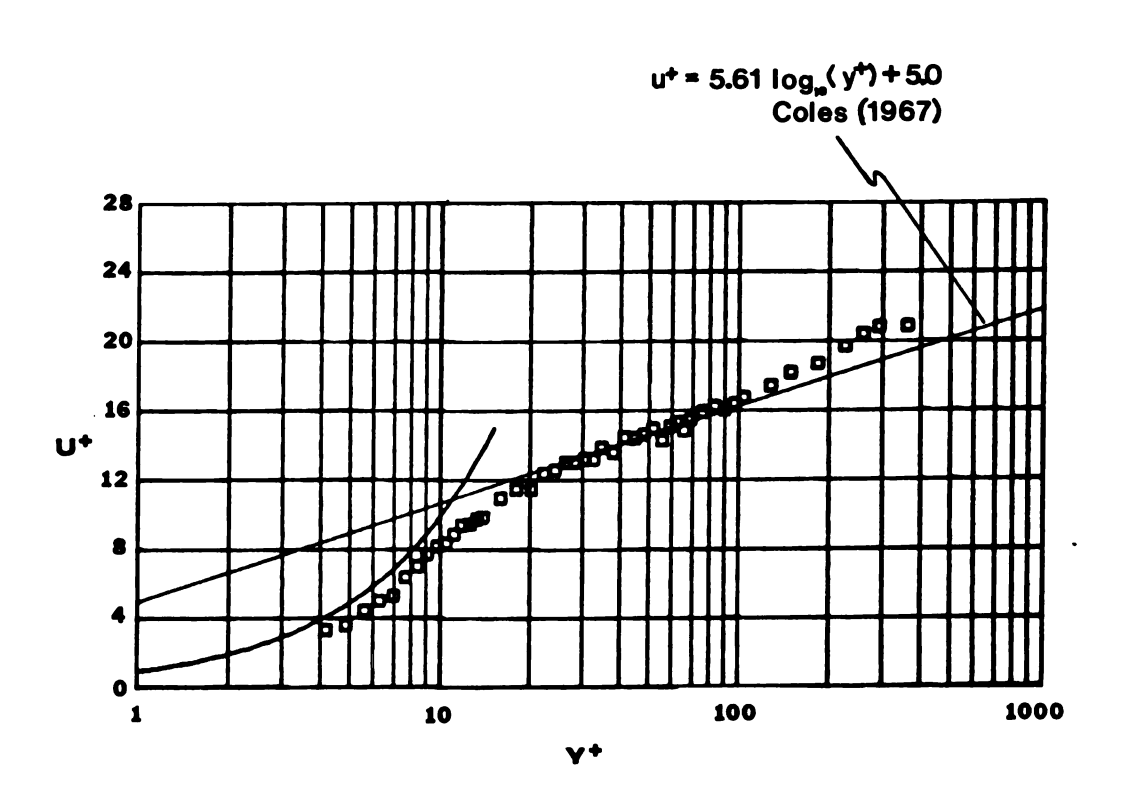
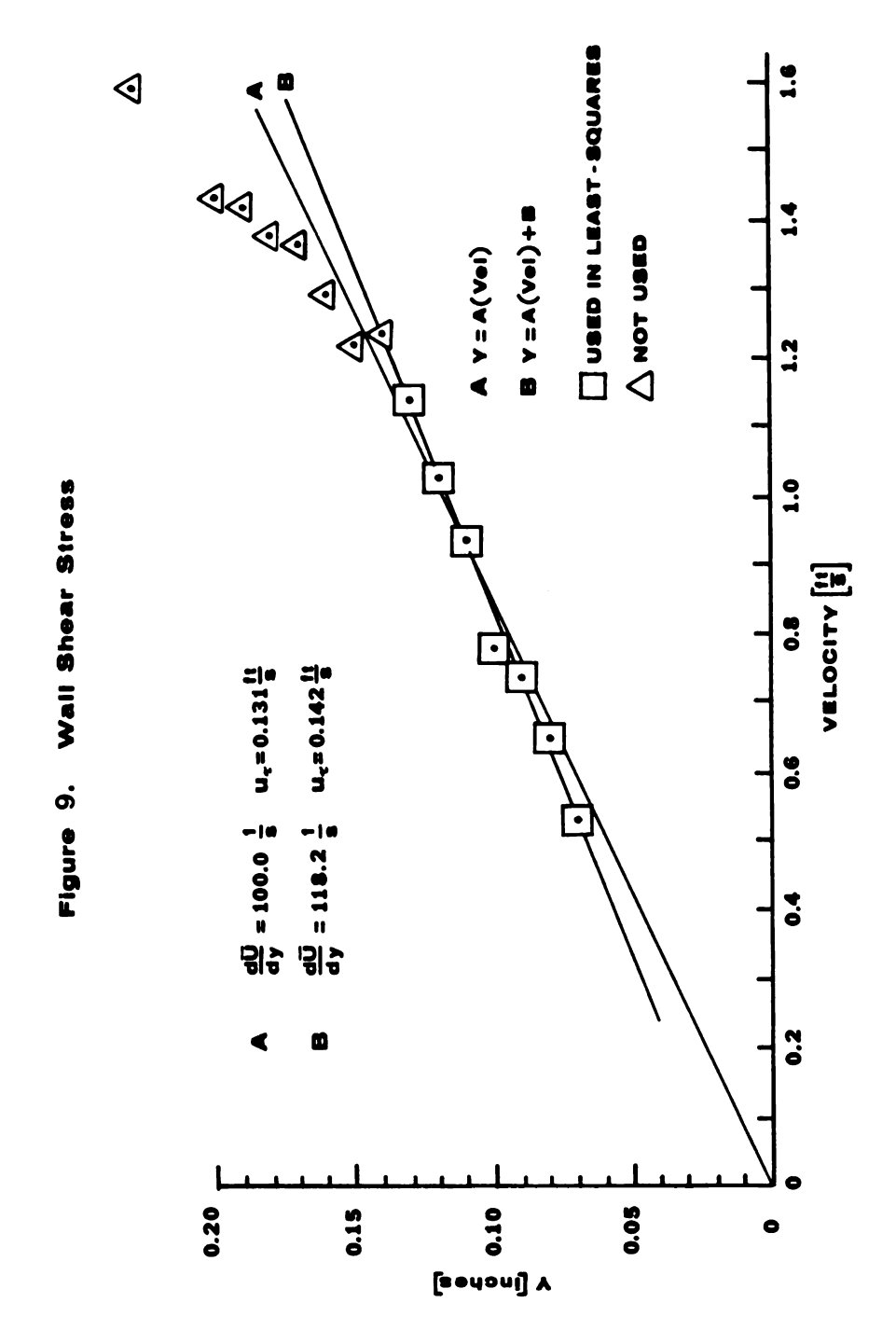


Figure 8. U+ vs. Y+ with Log Law Friction Velocity



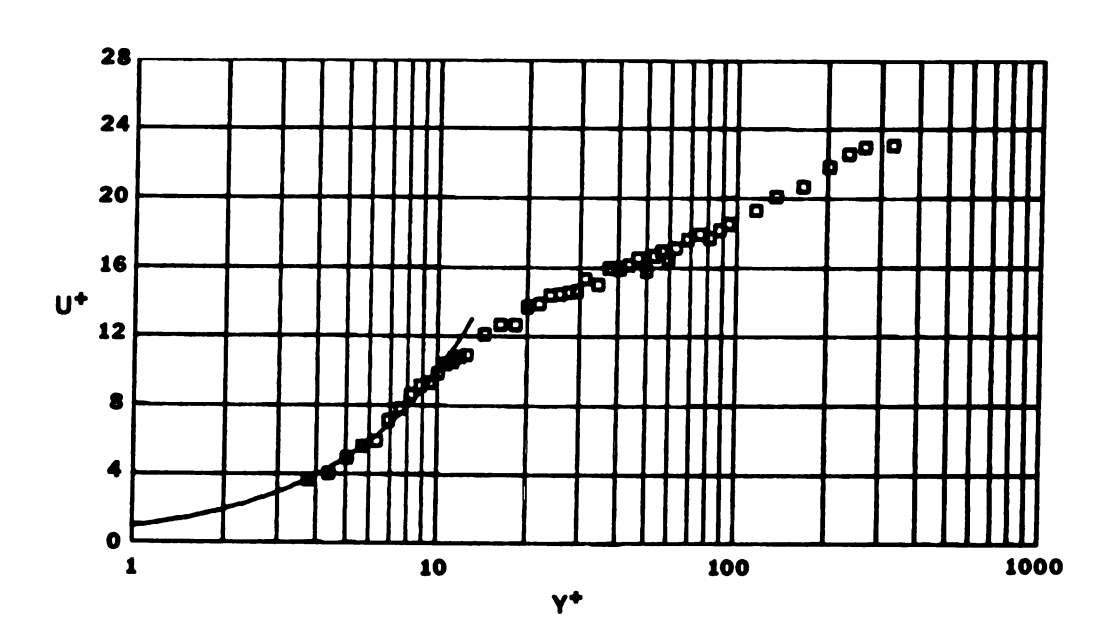


Figure 10. U+ vs. Y+ with Wall Shear Stress Friction Velocity

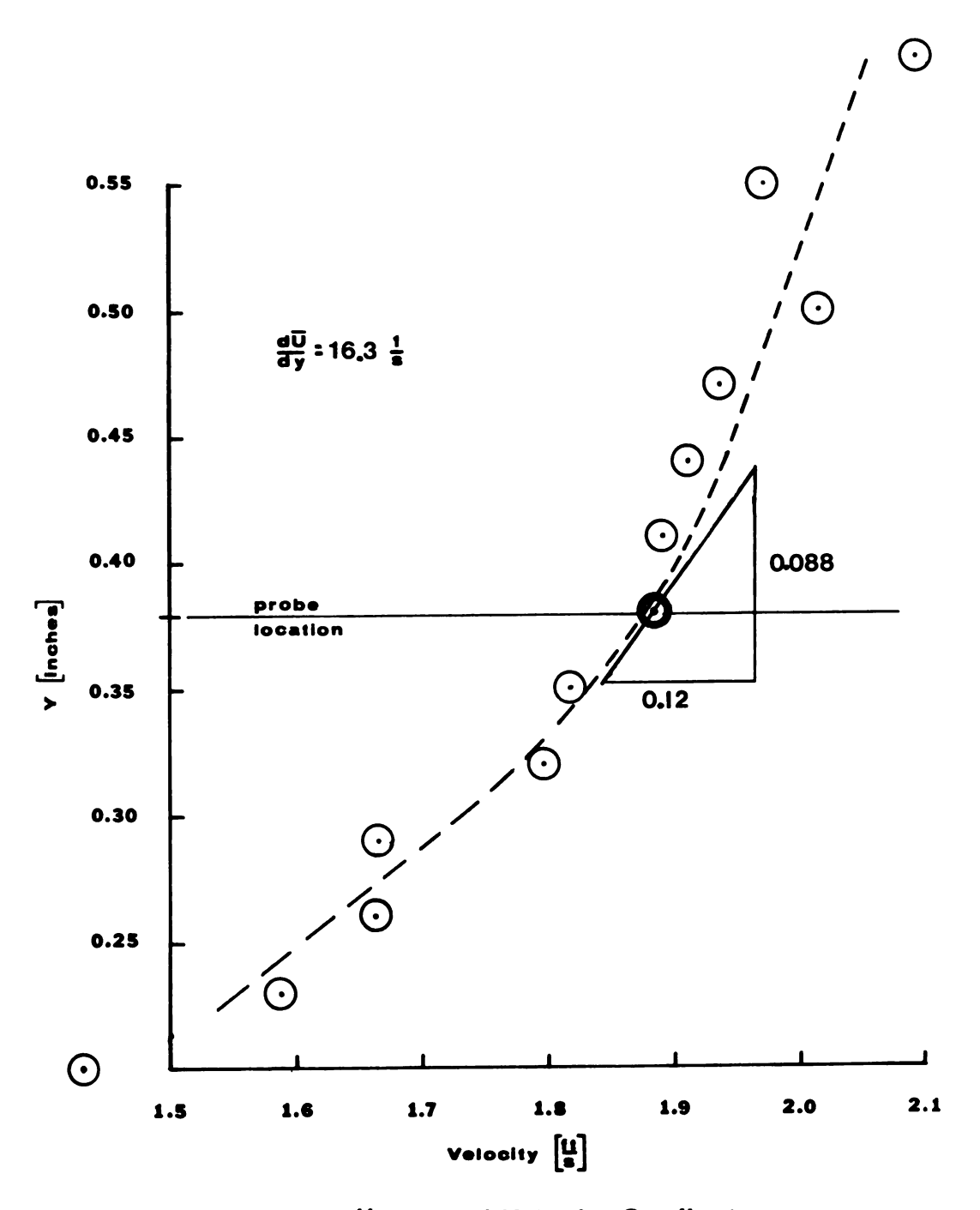


Figure 11. Local Velocity Gradient

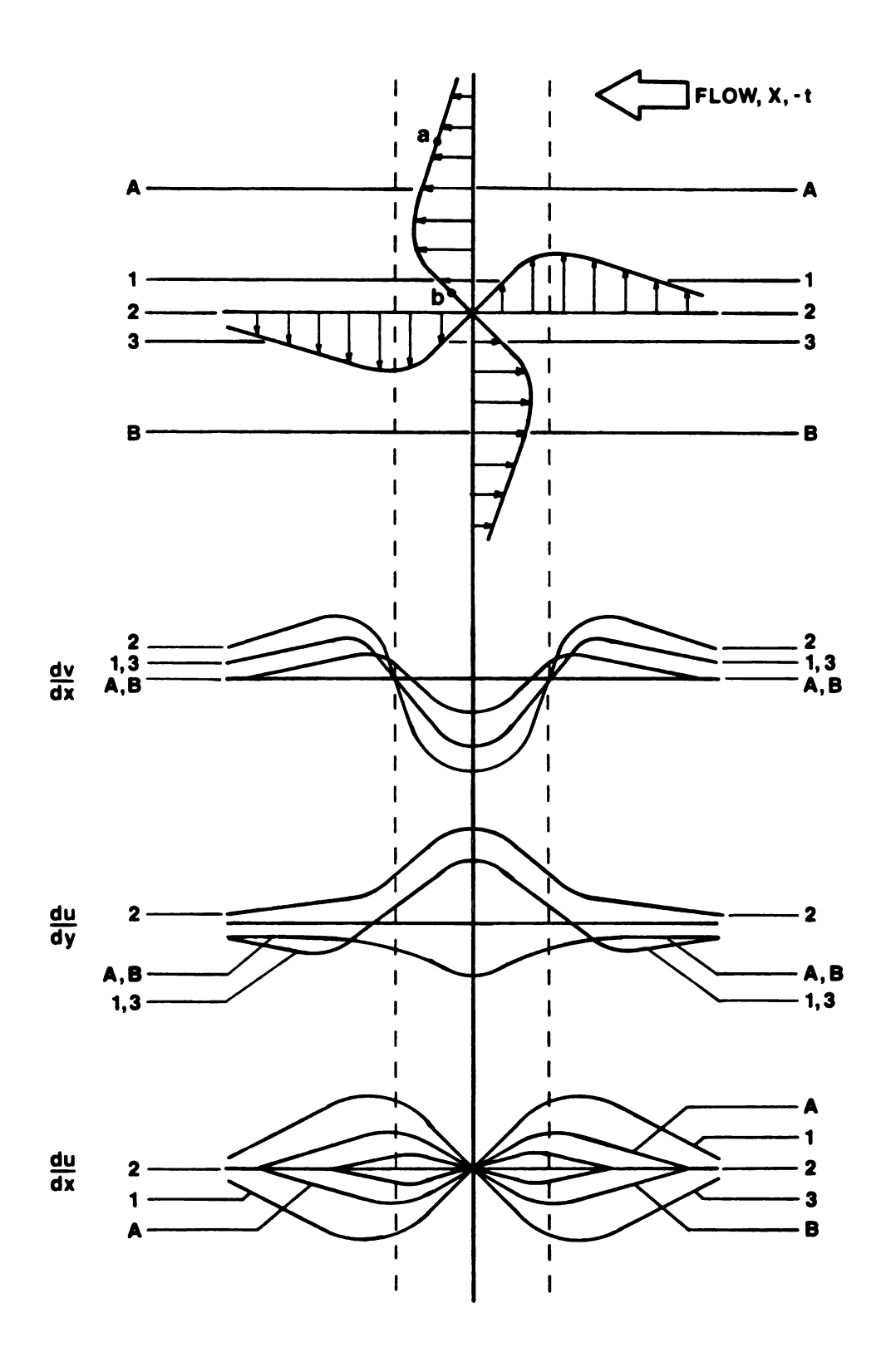
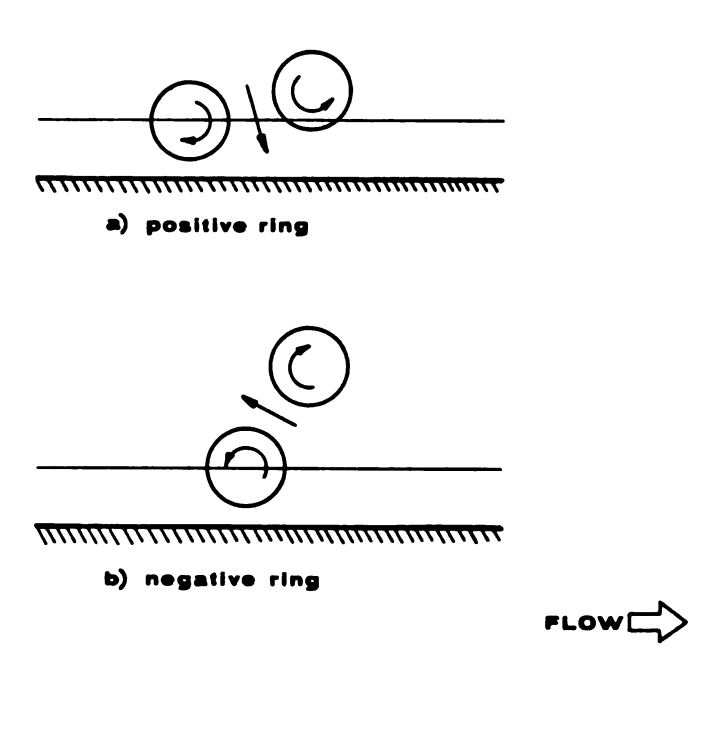
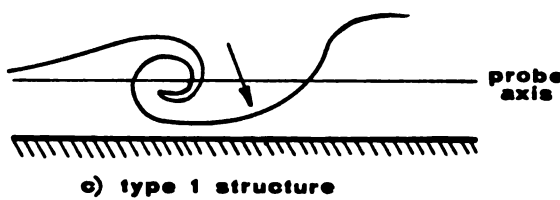


Figure 12. Derivative Signals Associated with a Vortex as a Function of Probe Position.





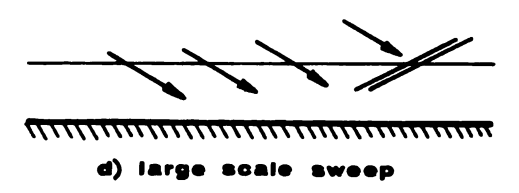
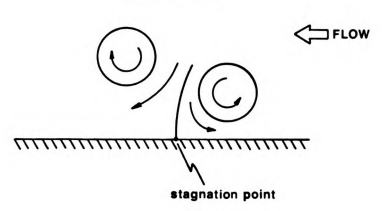


Figure 13, Causal structures

POSITIVE RING



NEGATIVE RING

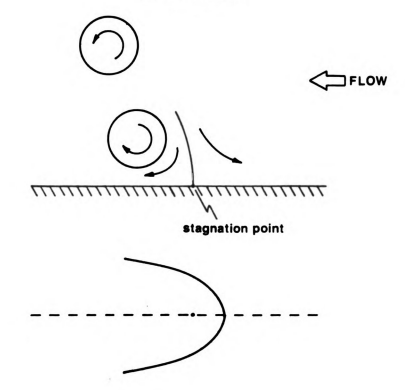
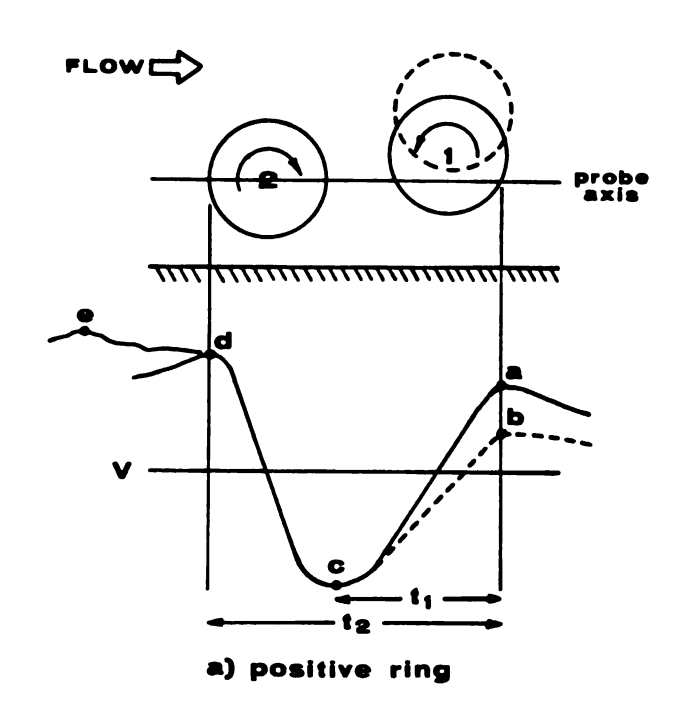


Figure 14. Stagnation Flow Fields Created by Vortex Pairs.



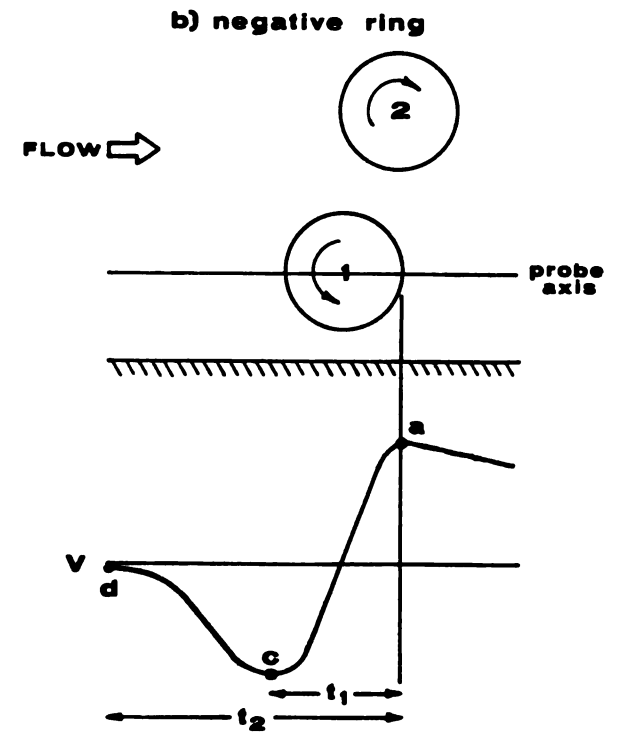


Figure 15. Normal Velocity Signal as a Means of Identifying Structural Boundaries. 207

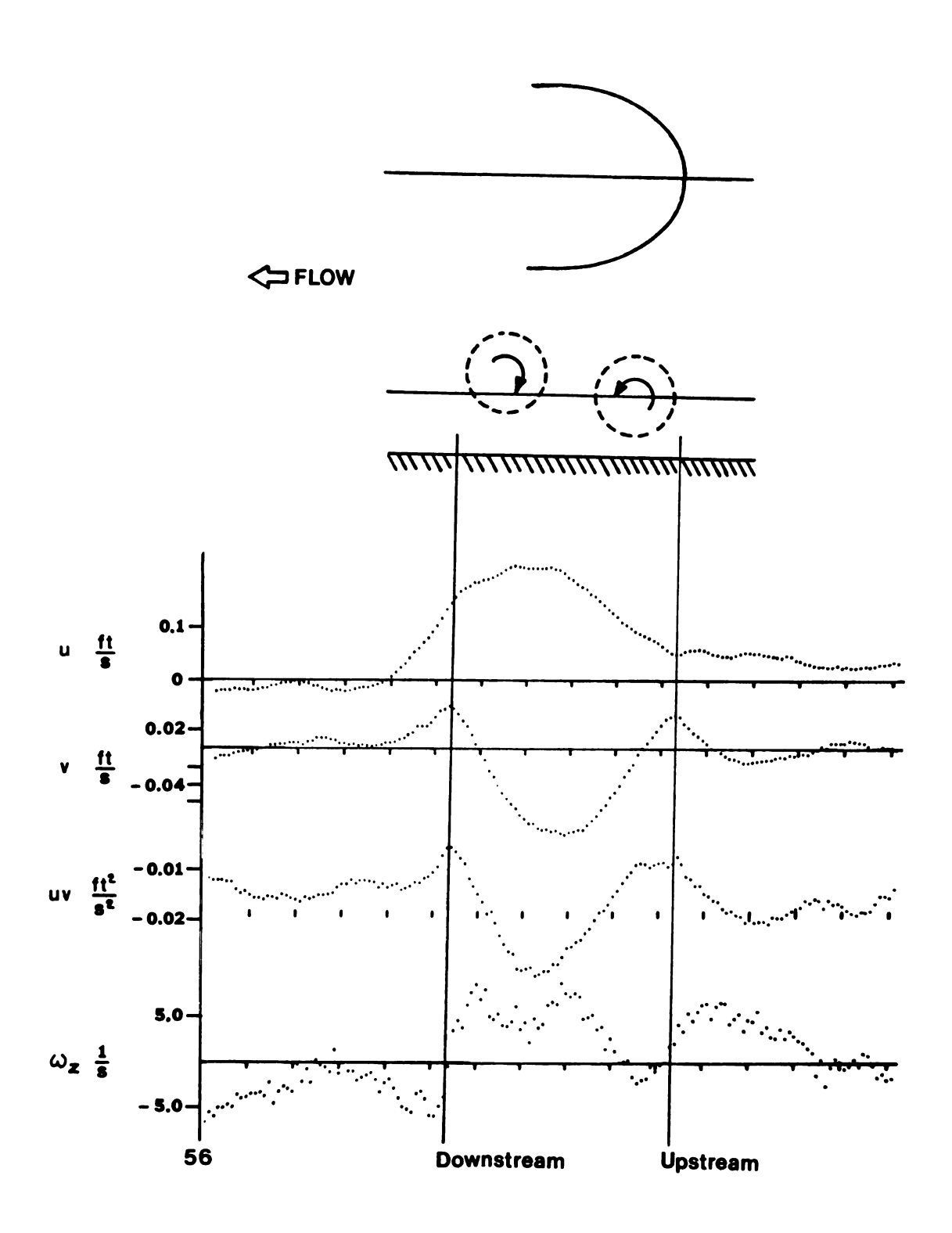


Figure 16a Ensemble Averaged Signals of Positive Rings with High $\dot{\mathbf{V}}$ isual Certainty

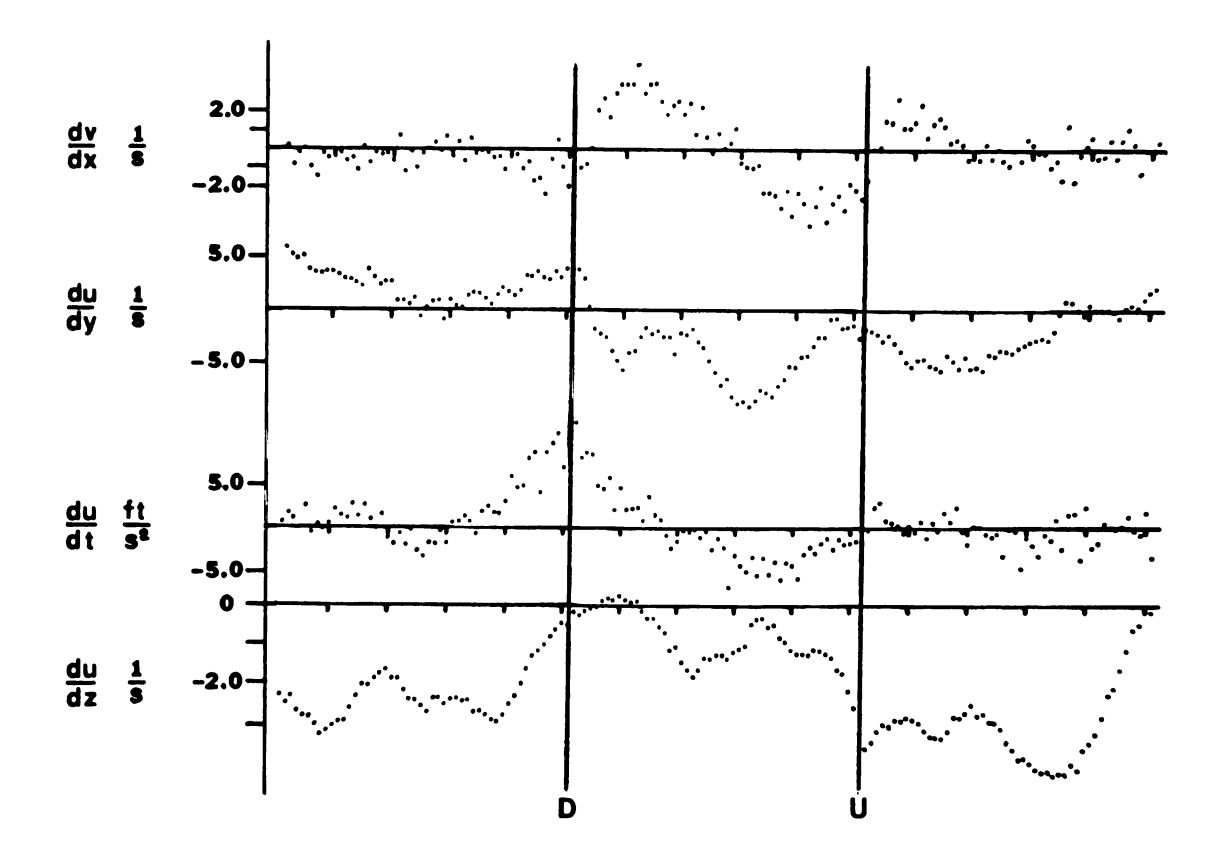


Figure 16b Ensemble Averaged Signals of Positive Rings with High Visual Certainty

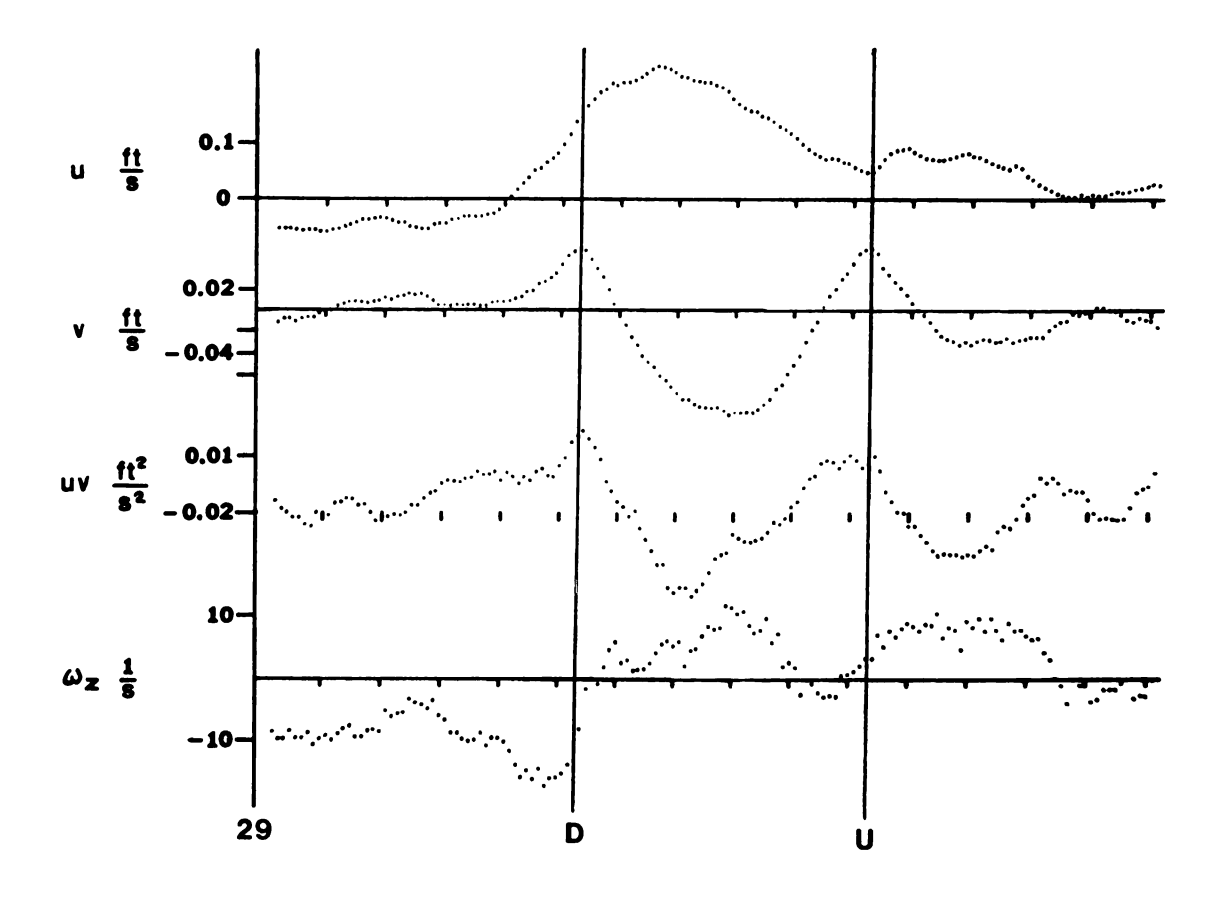


Figure 17a Ensemble Averaged Signals of Positive Rings with High Visual Certainty and Centered Pockets

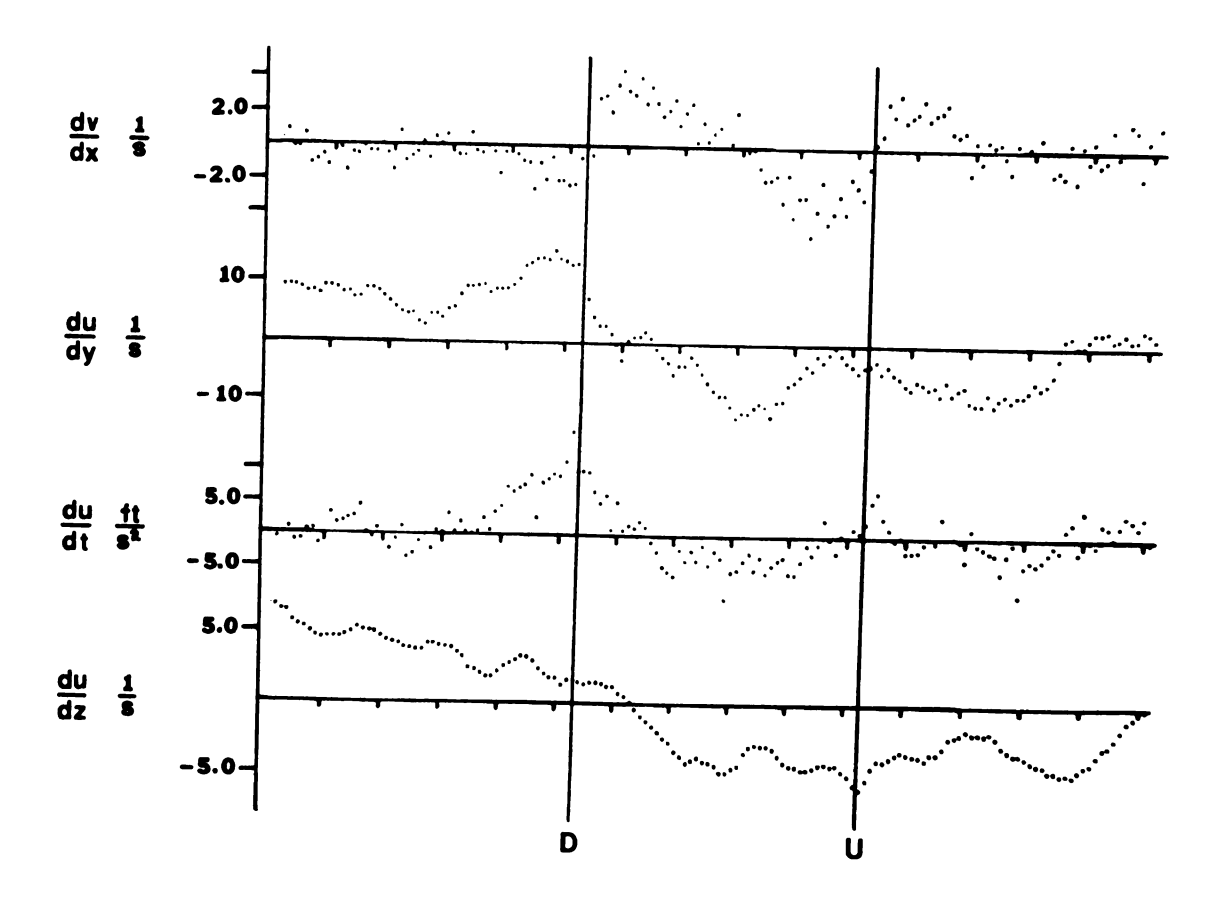


Figure 17b Ensemble Averaged Signals of Positive Rings with High Visual Certainty and Centered Pockets

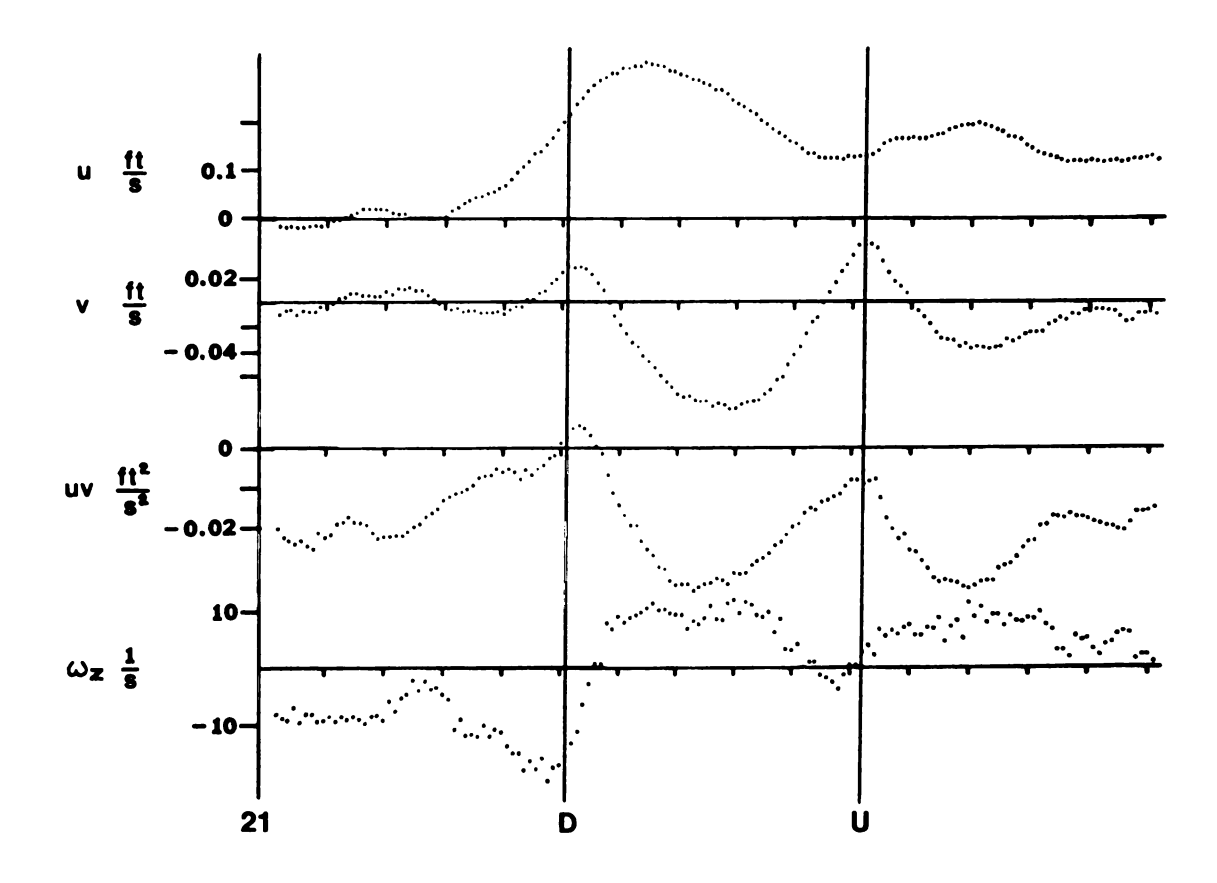


Figure 18a Ensemble Averaged Signals of Positive Rings with High Visual Certainty and Centered Pockets in Early Stages

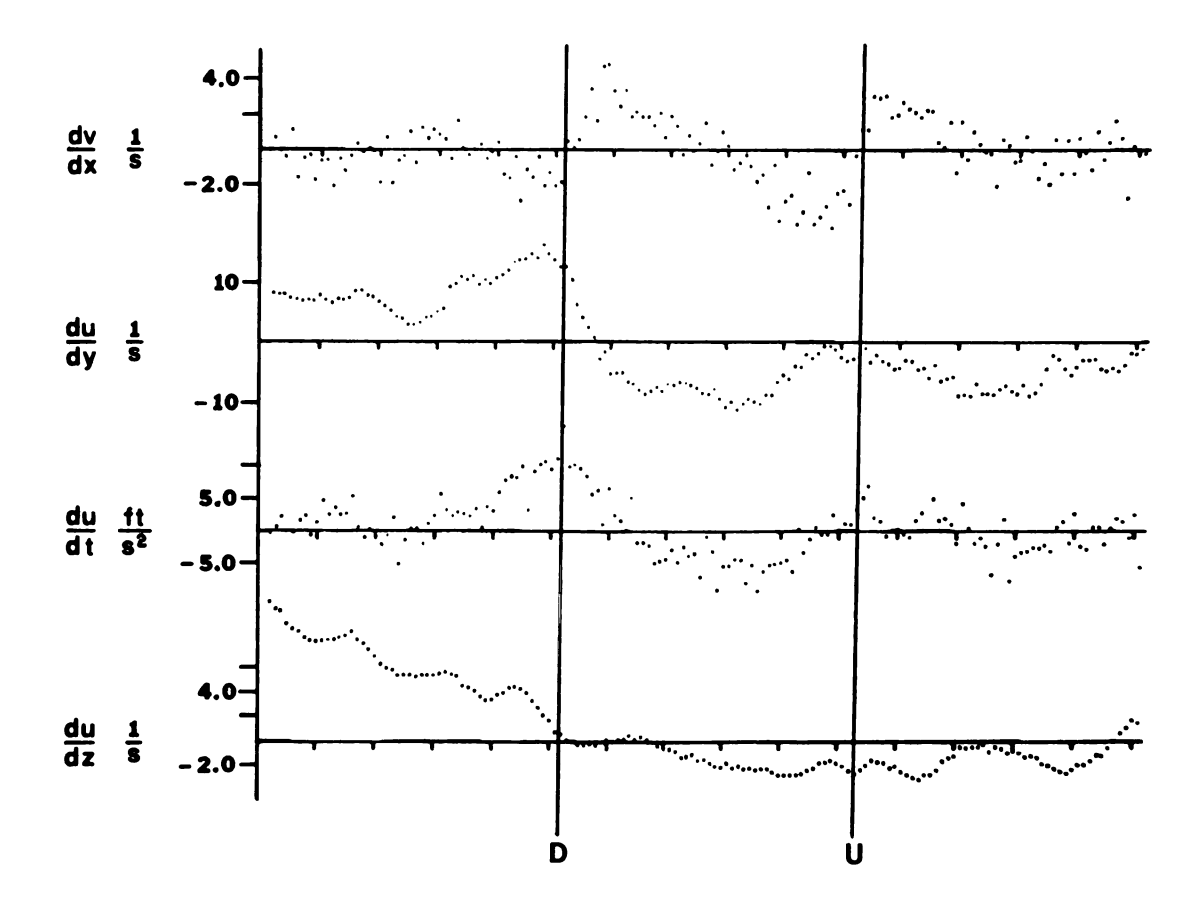


Figure 18b Ensemble Averaged Signals of Positive Rings with High Visual Certainty and Centered Pockets in Early Stages

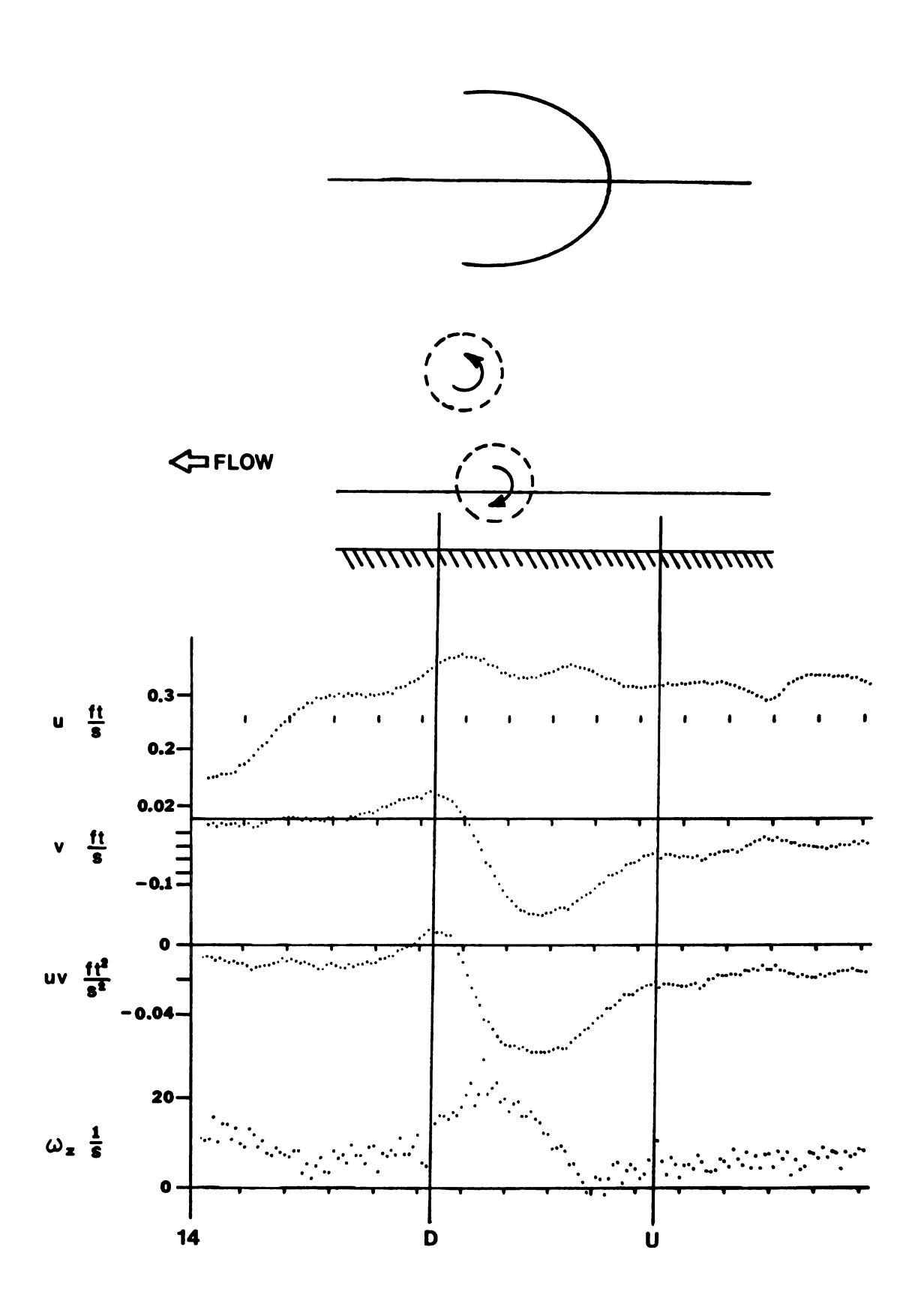


Figure 19a Ensemble Averaged Signals of Negative Rings with High Visual Certainty and Centered Pockets

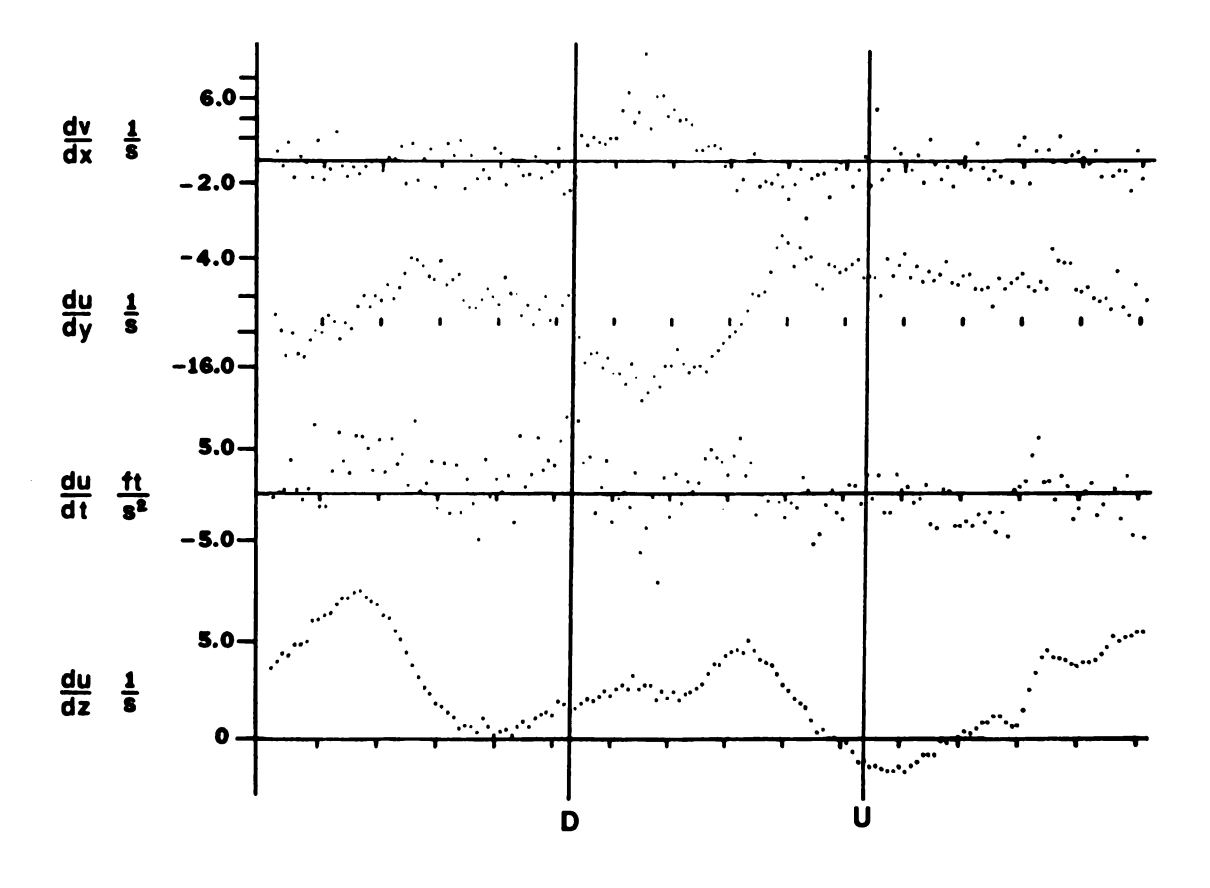


Figure 19b Ensemble Averaged Signals of Negative Rings with High Visual Certainty and Centered Pockets

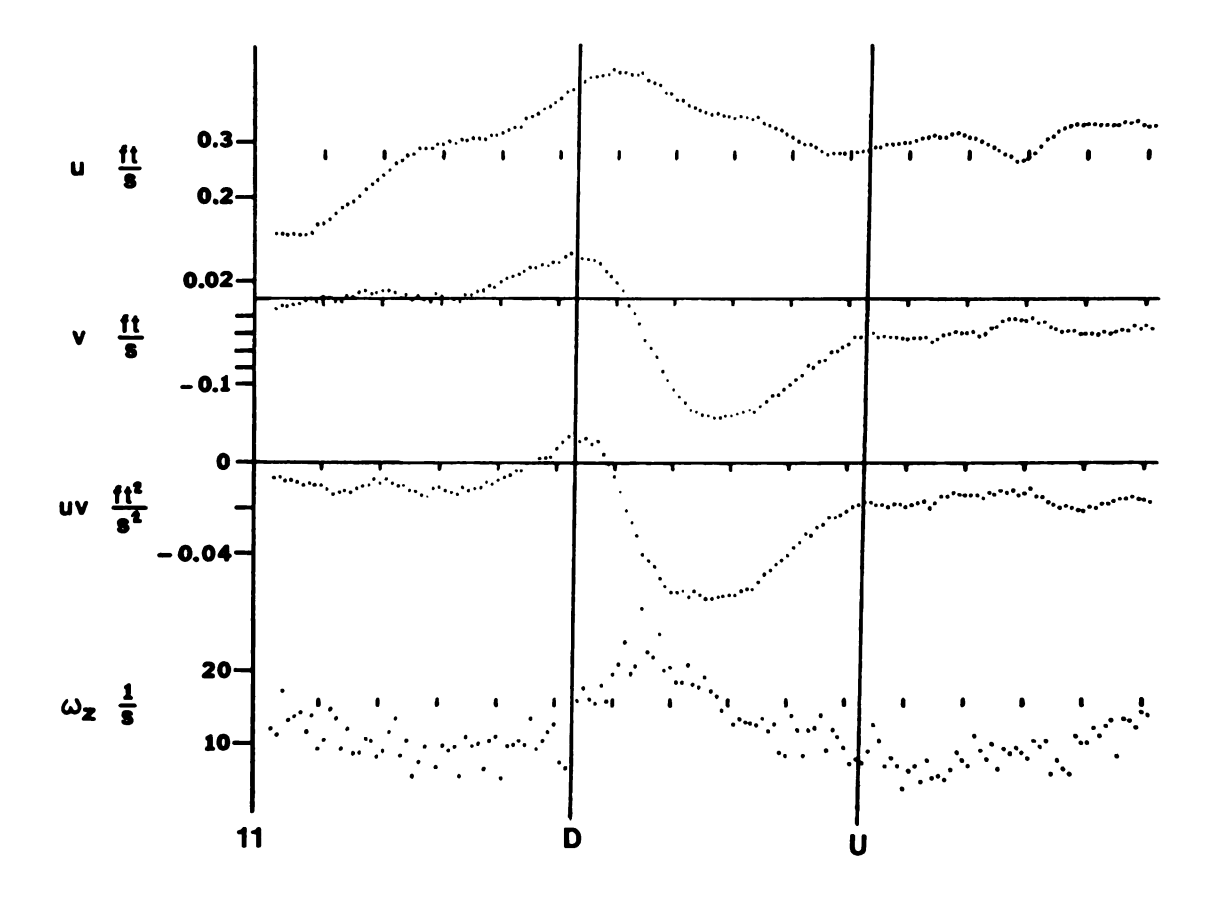


Figure 20a Ensemble Averaged Signals of Negative Rings with High Visual Certainty and Centered Pockets in Early Stages

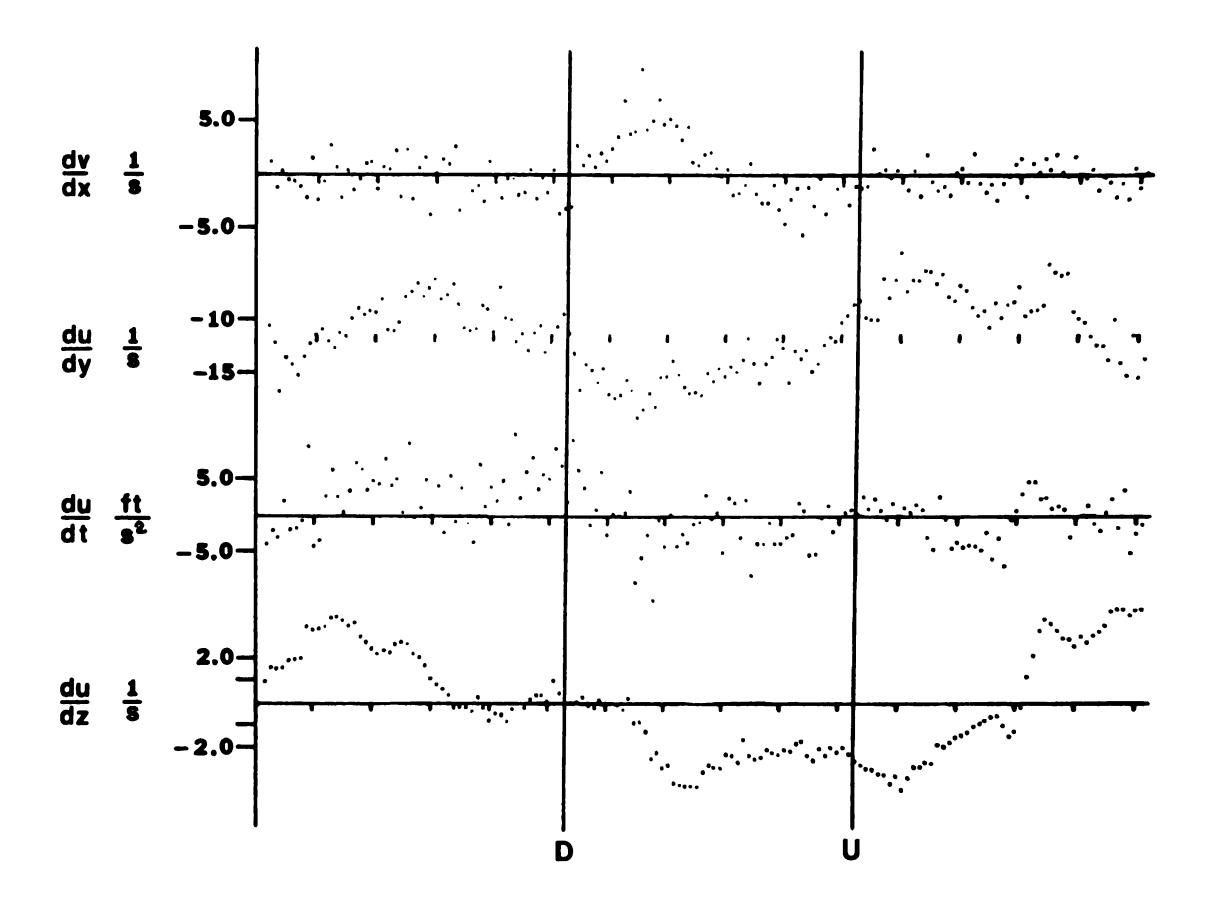


Figure 20b Ensemble Averaged Signals of Negative Rings with High Visual Certainty and Centered Pockets in Early Stages

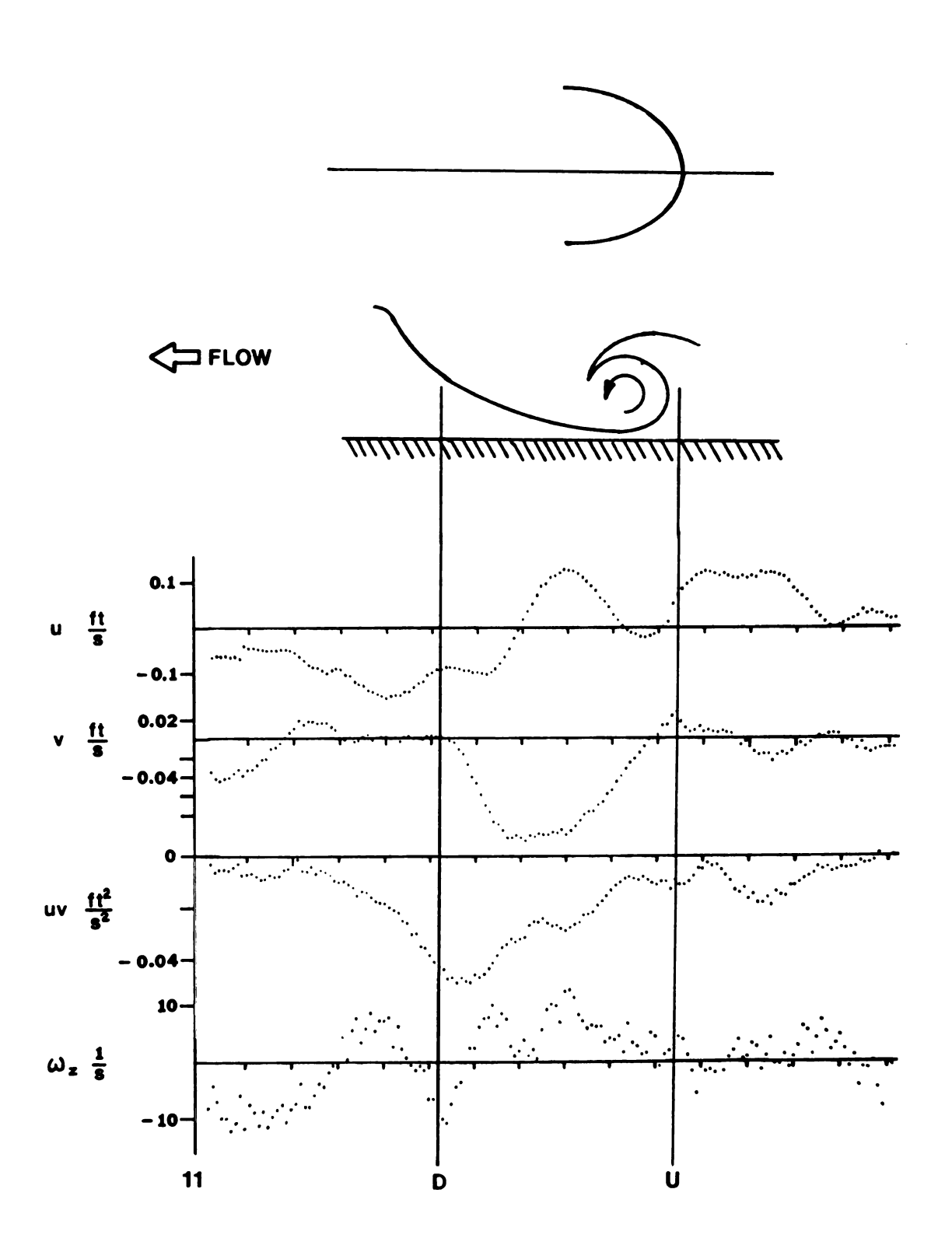


Figure 21a Ensemble Averaged Signals of Type 1 Structures with High Visual Certainty and Pockets in Early Stages

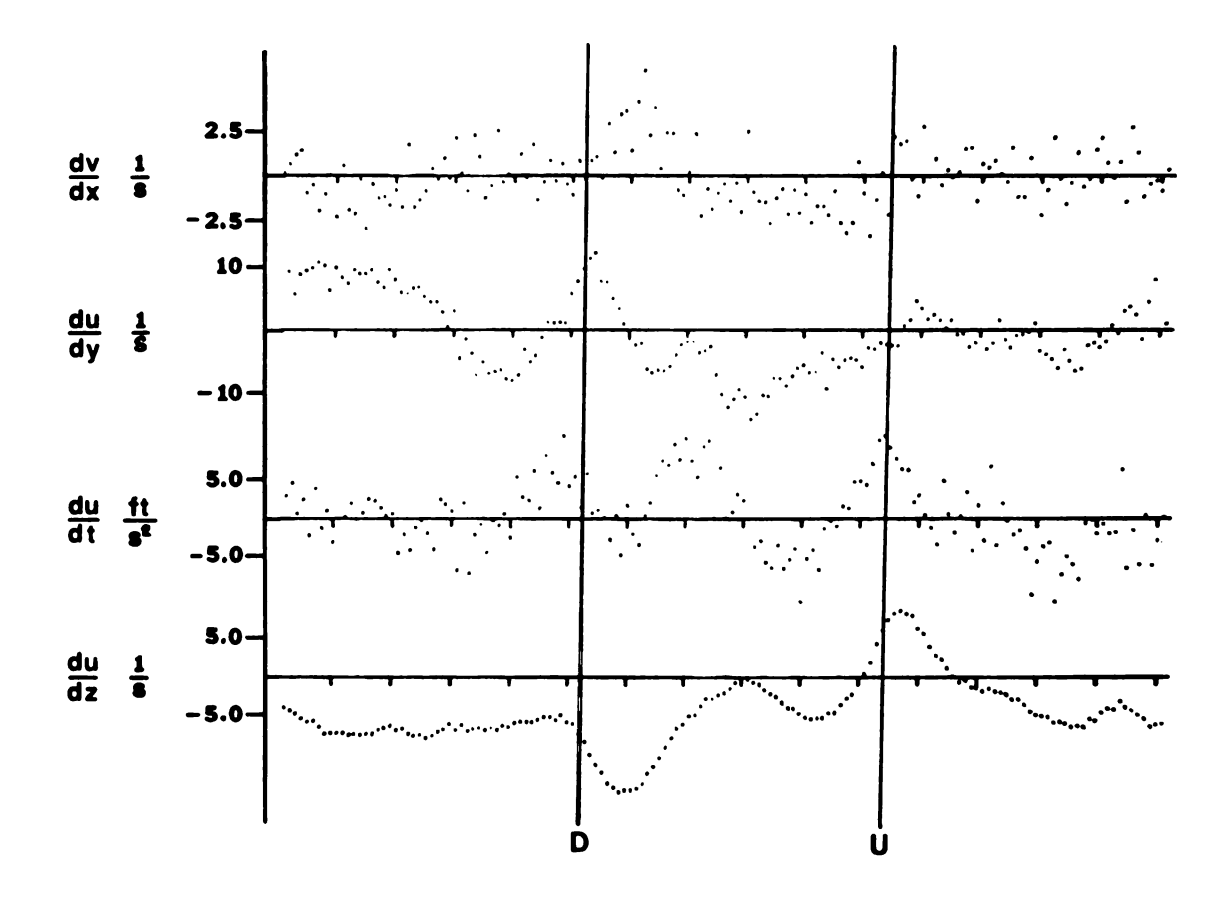


Figure 21b Ensemble Averaged Signals of Type 1 Structures with High Visual Certainty and Pockets in Early Stages

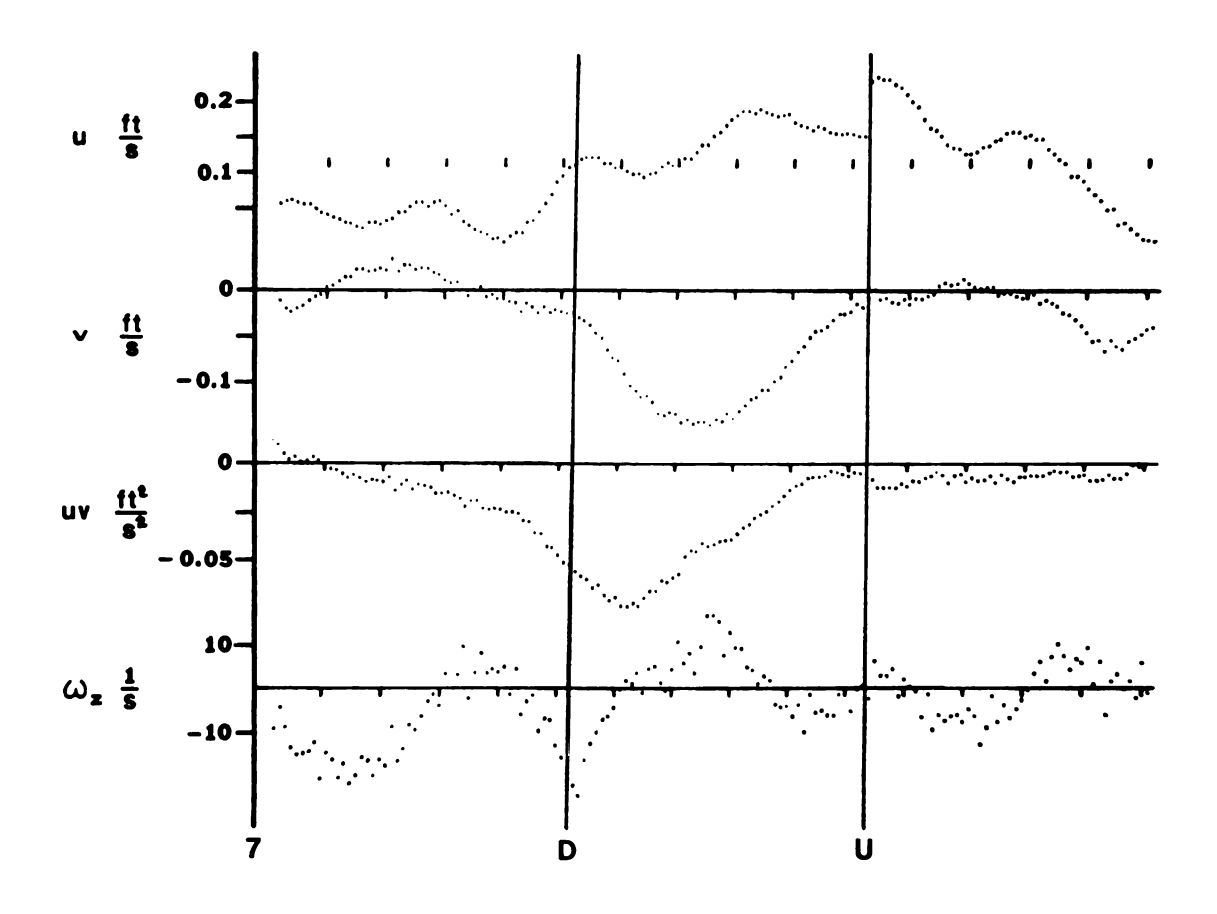


Figure 22a Ensemble Averaged Signals of Type 1 Structures with High Visual Certainty and Centered Pockets in Early Stages

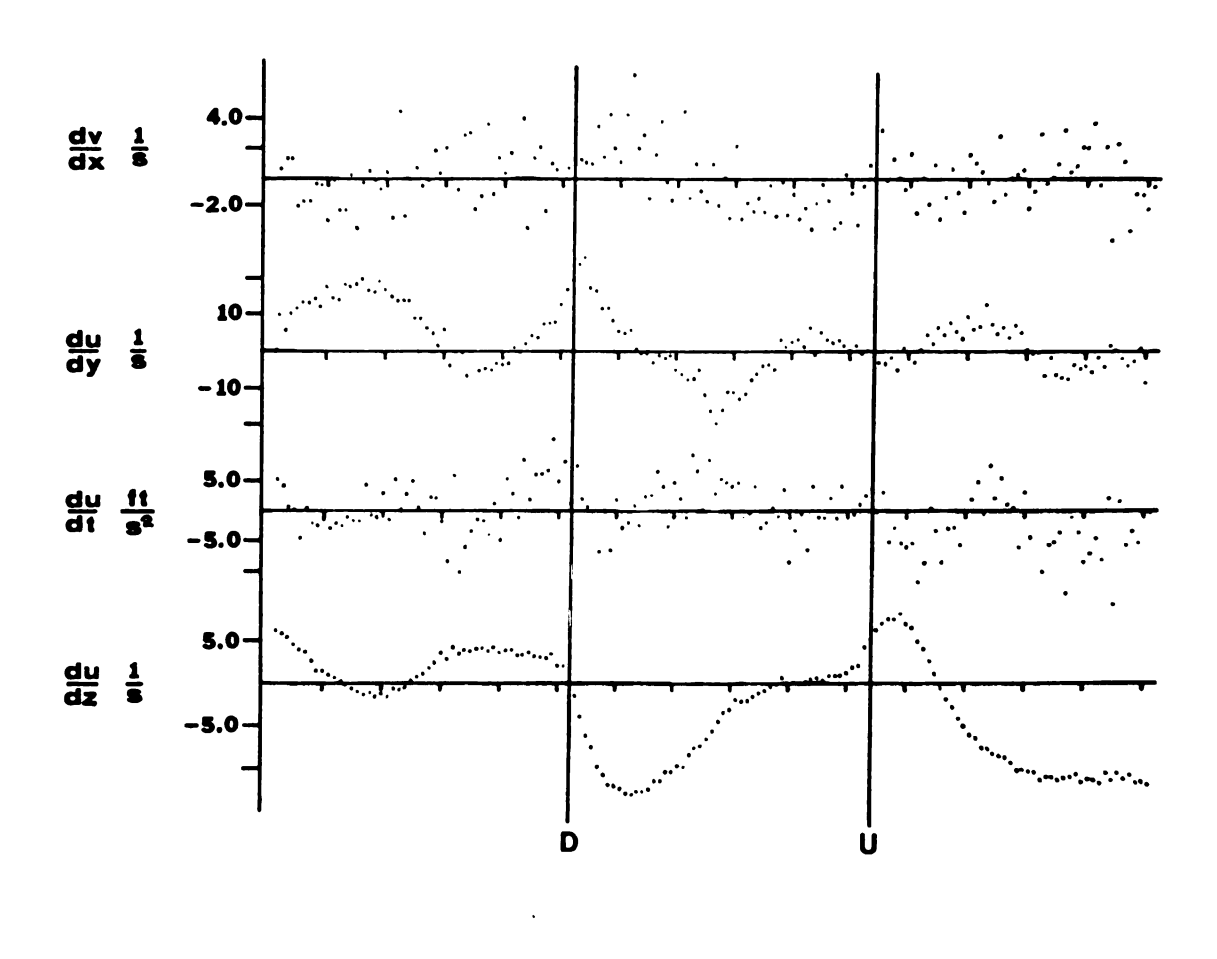
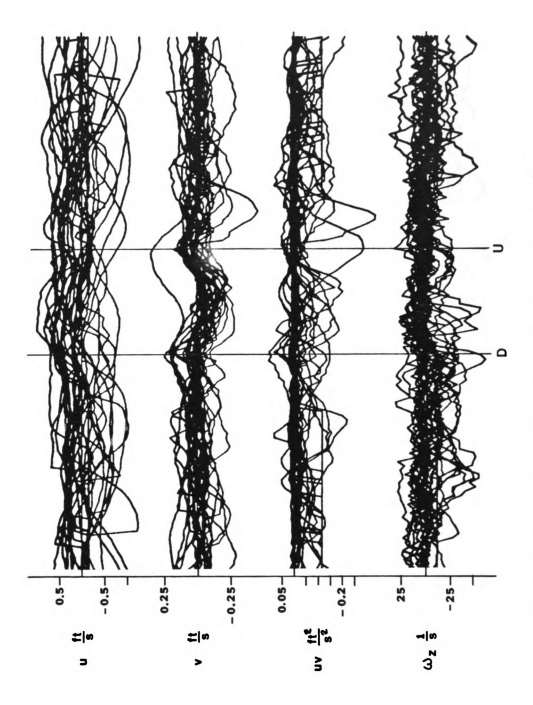
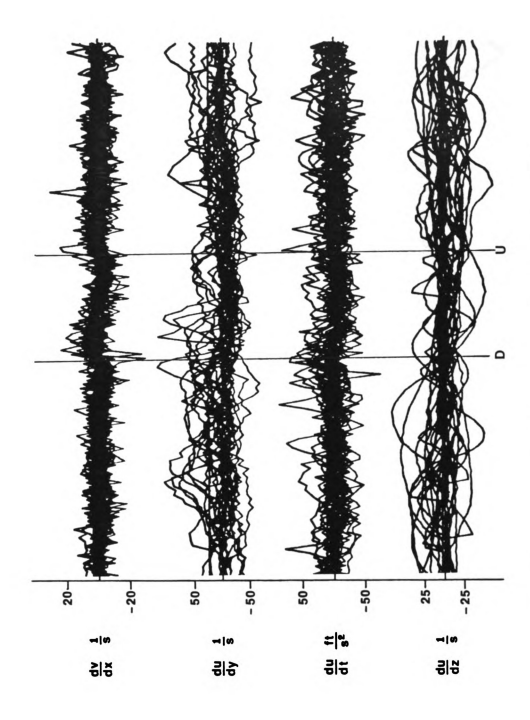


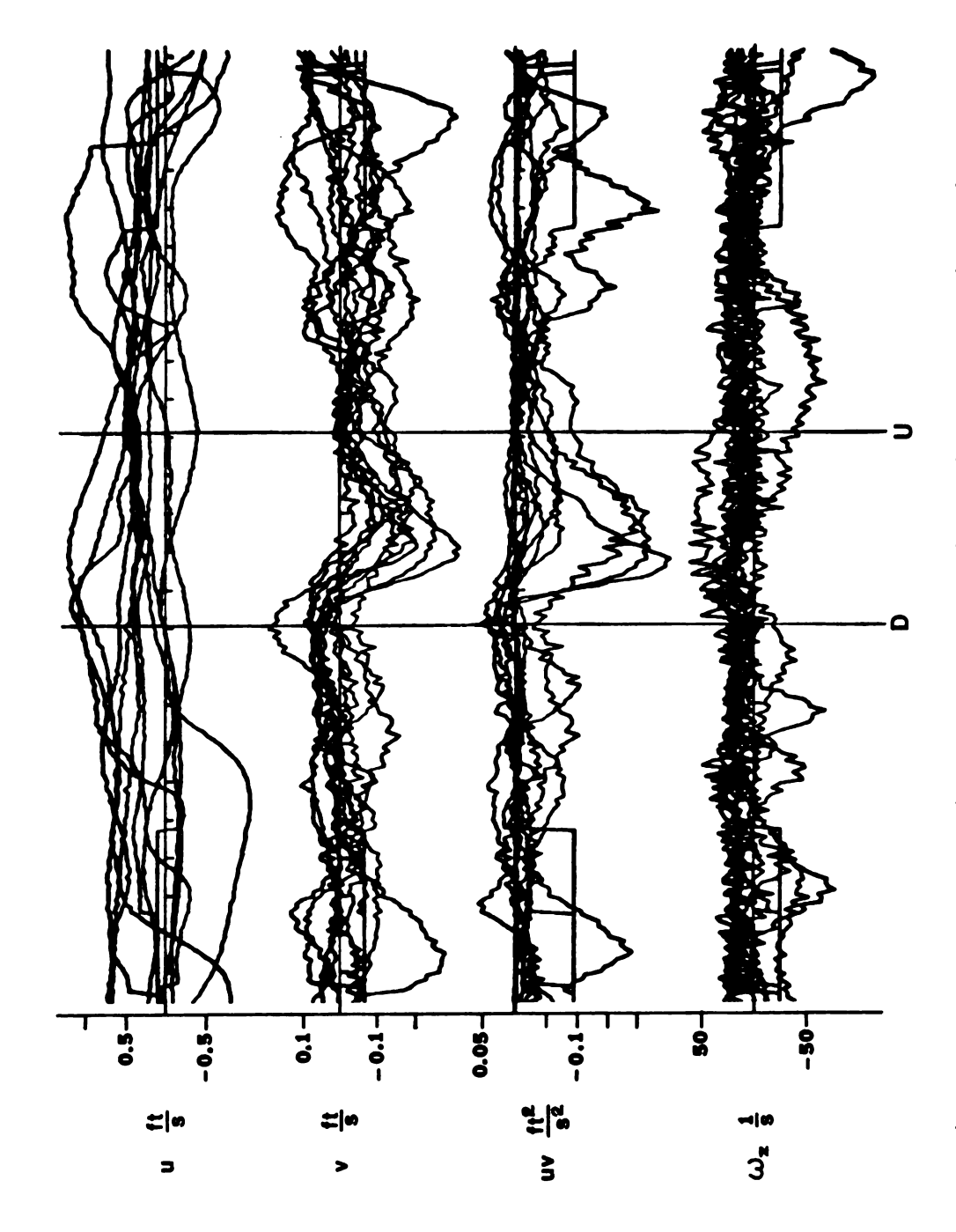
Figure 22b Ensemble Averaged Signals of Type 1 Structures with High Visual Certainty and Centered Pockets in Early Stages



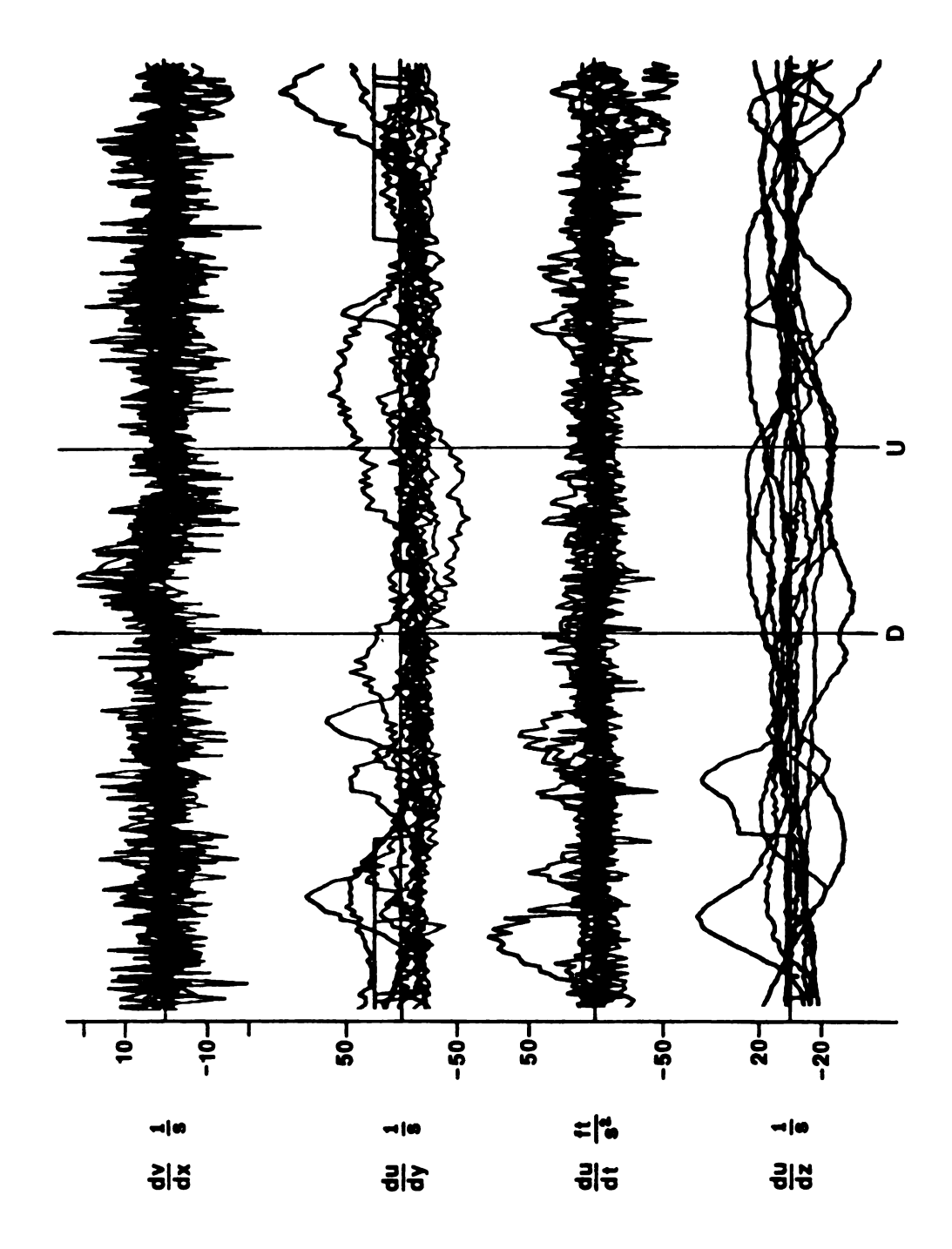
Scaled Signals of Positive Rings with High Visual Certainty and Centered Pockets Figure 23a



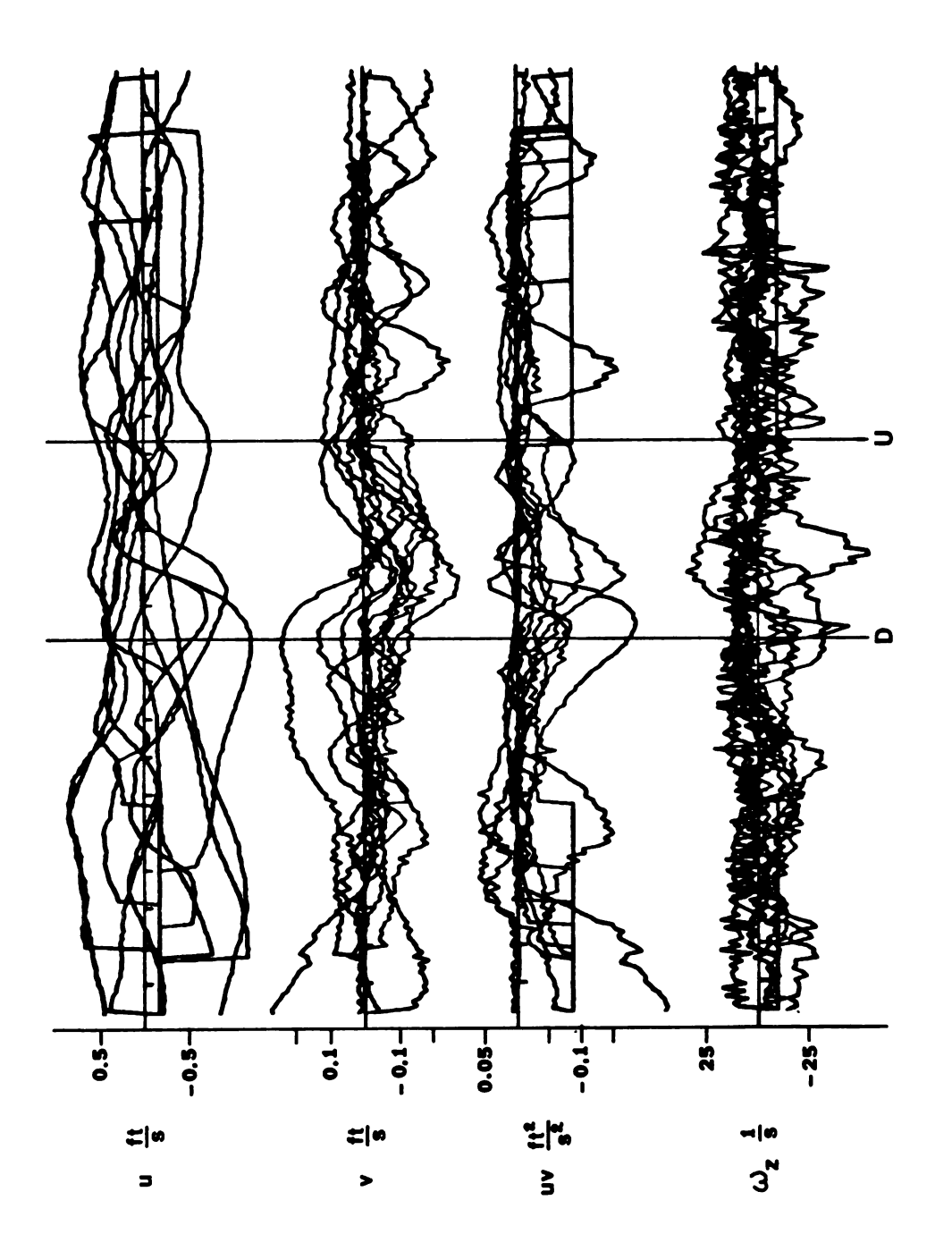
Scaled Signals of Positive Rings with High Visual Certainty and Centered Pockets Figure 23b



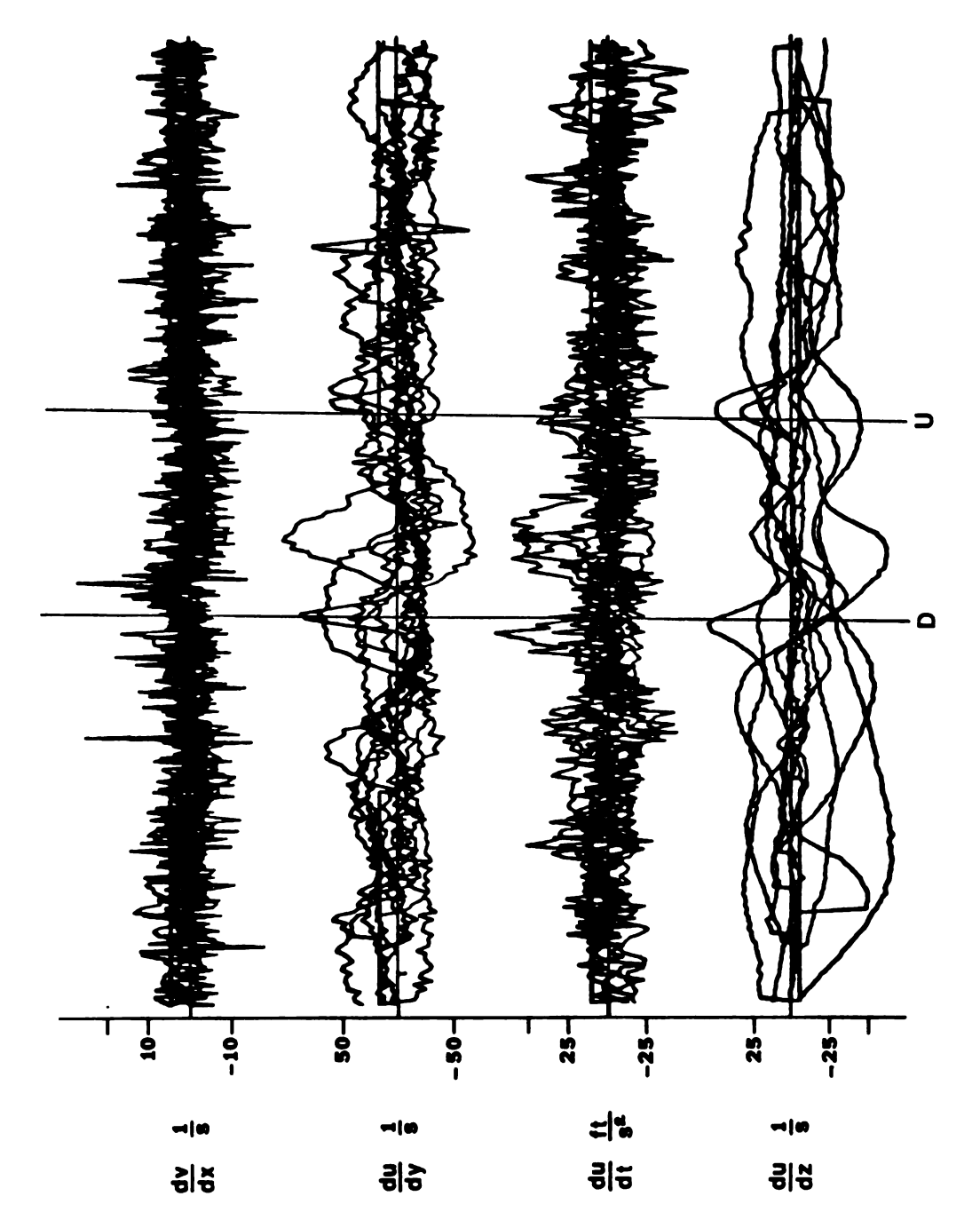
Scaled Signals of Negative Rings with High Visual Certainty and Centered Pockets in Early Stages Figure 24a



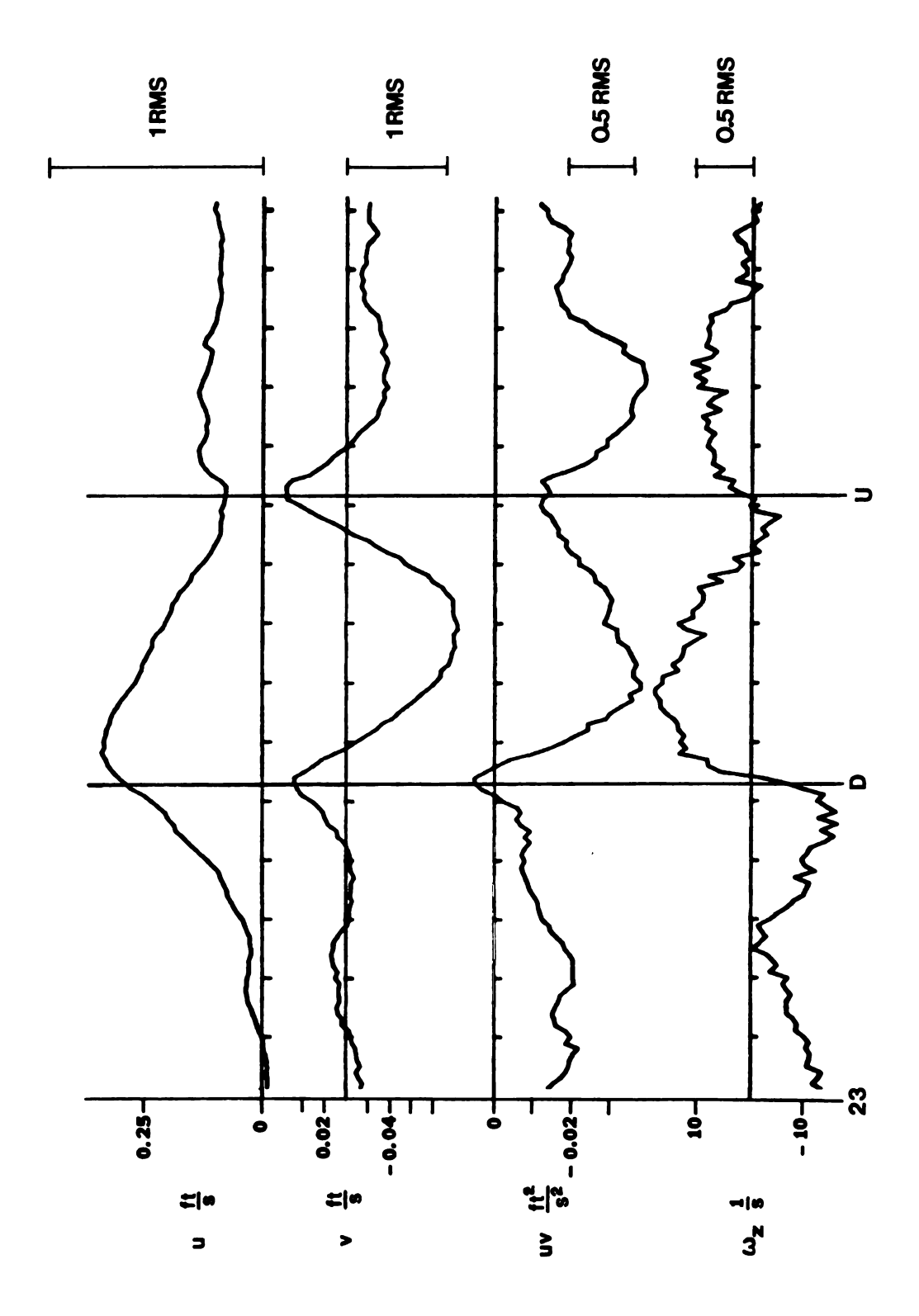
Scaled Signals of Negative Rings with High Visual Certainty and Centered Pockets in Early Stages Figure 24b



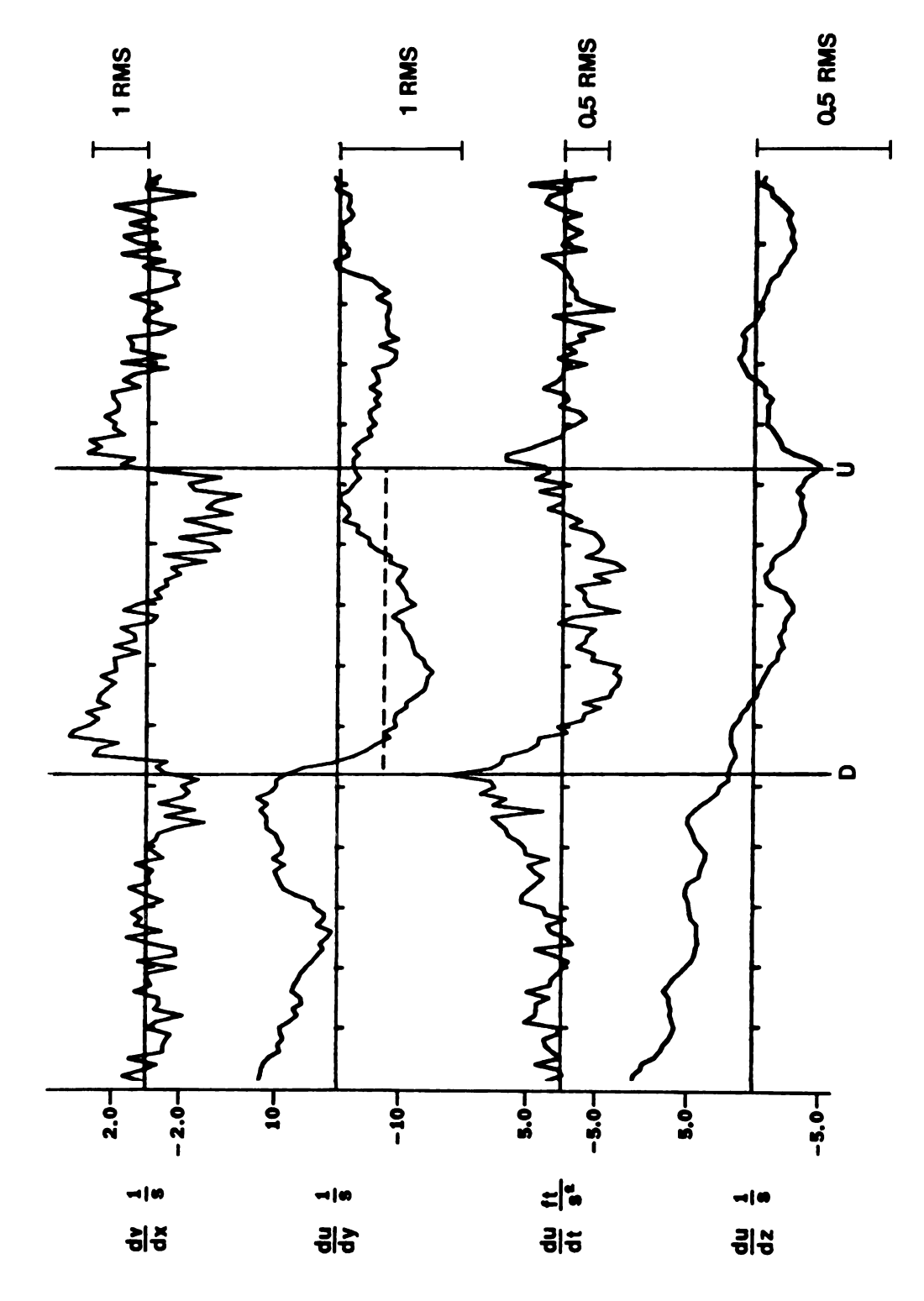
Scaled Signals of Type 1 Structures with High Visual Certainty and Pockets in Early Stages Figure 25a



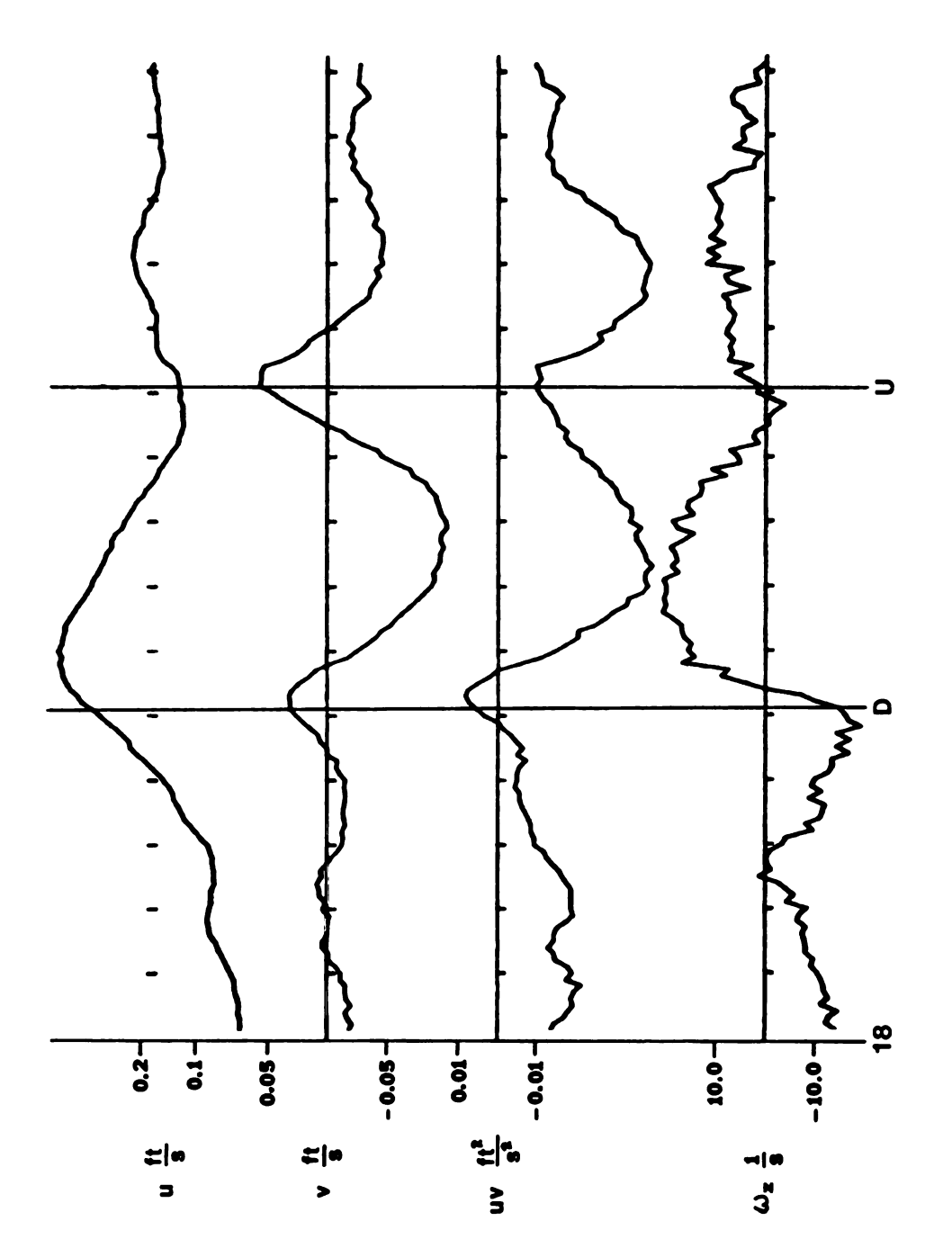
Scaled Signals of Type 1 Structures with High Visual Certainty and Pockets in Early Stages Figure 25b



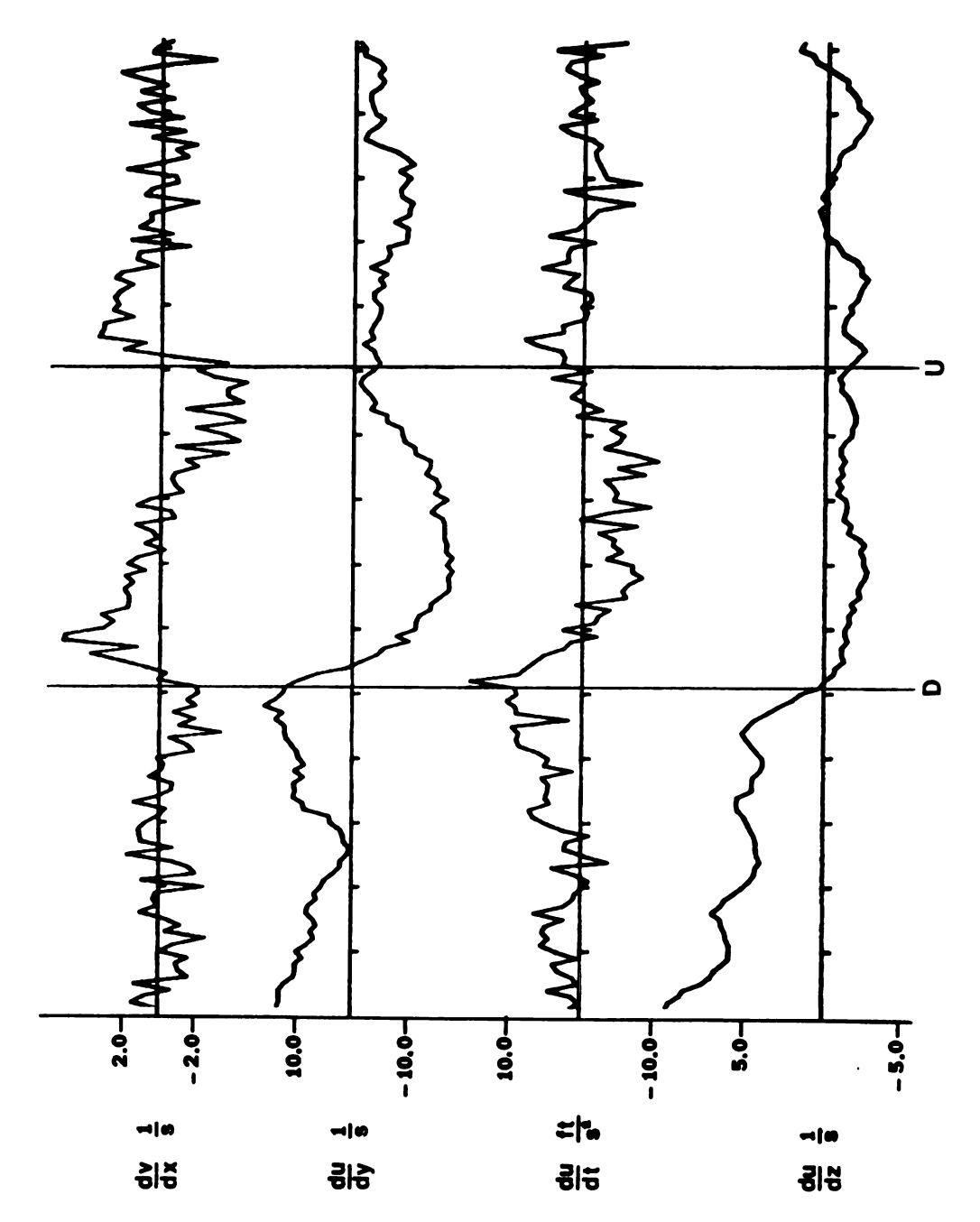
Ensemble Averaged Signals of Positive Rings with High Visual Certainty and Centered Pockets After Removing Six Samples Figure 26a



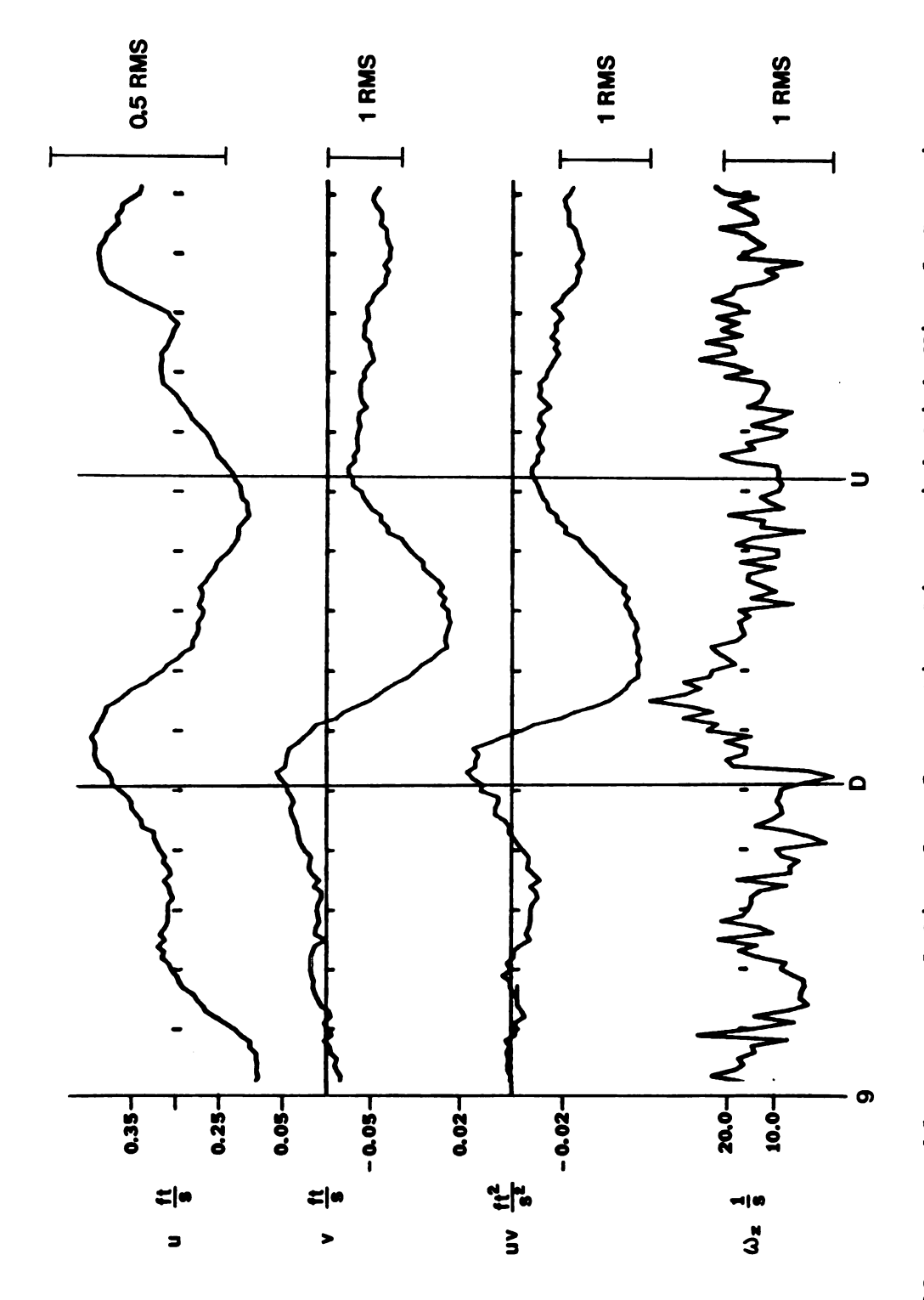
Ensemble Averaged Signals of Positive Rings with High Visual Certainty and Centered Pockets After Removing Six Samples Figure 26b



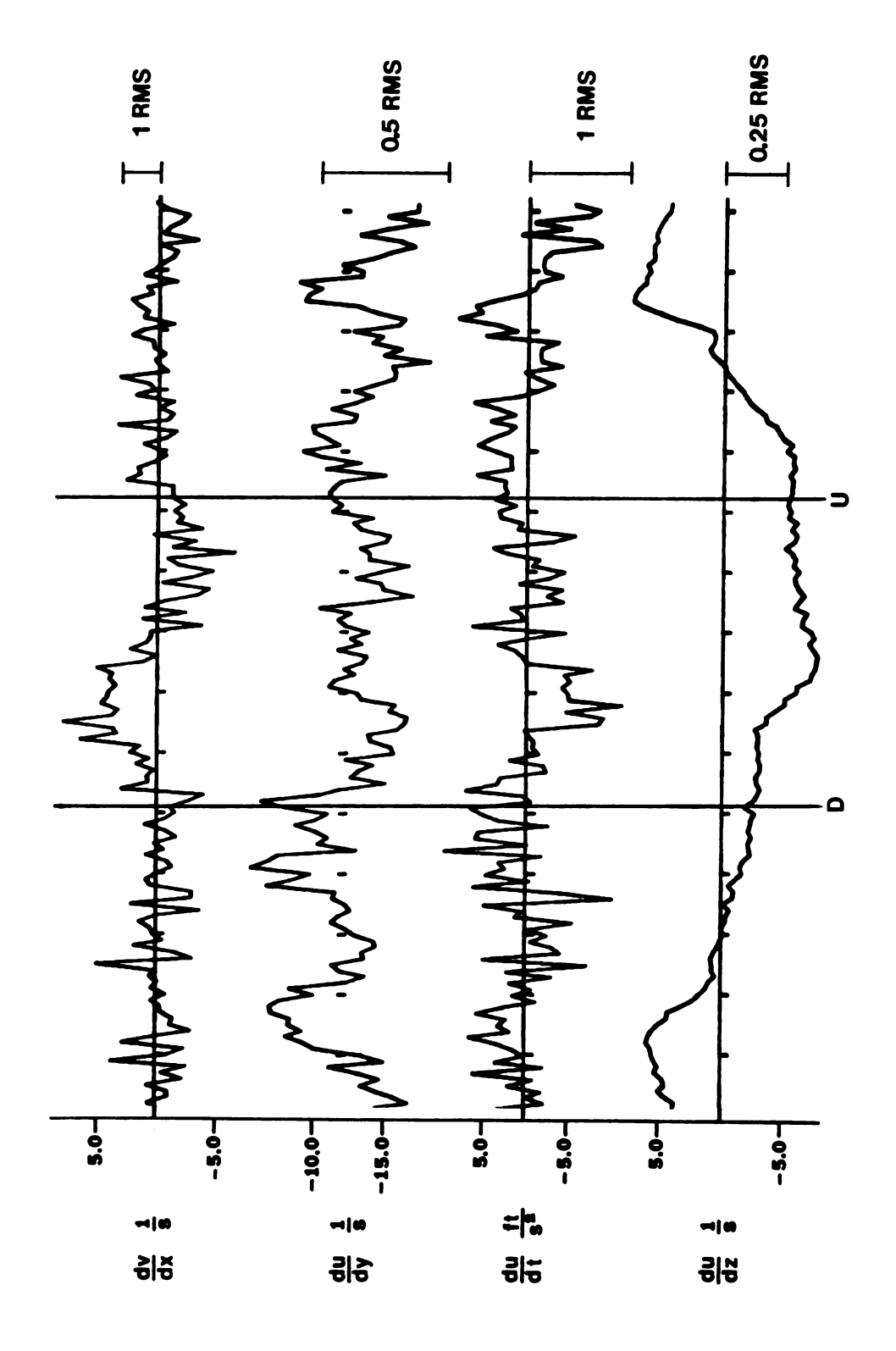
Ensemble Averaged Signals of Positive Rings with High Visual Certainty and Centered Pockets in Early Stages After Removing Three Samples Figure 27a



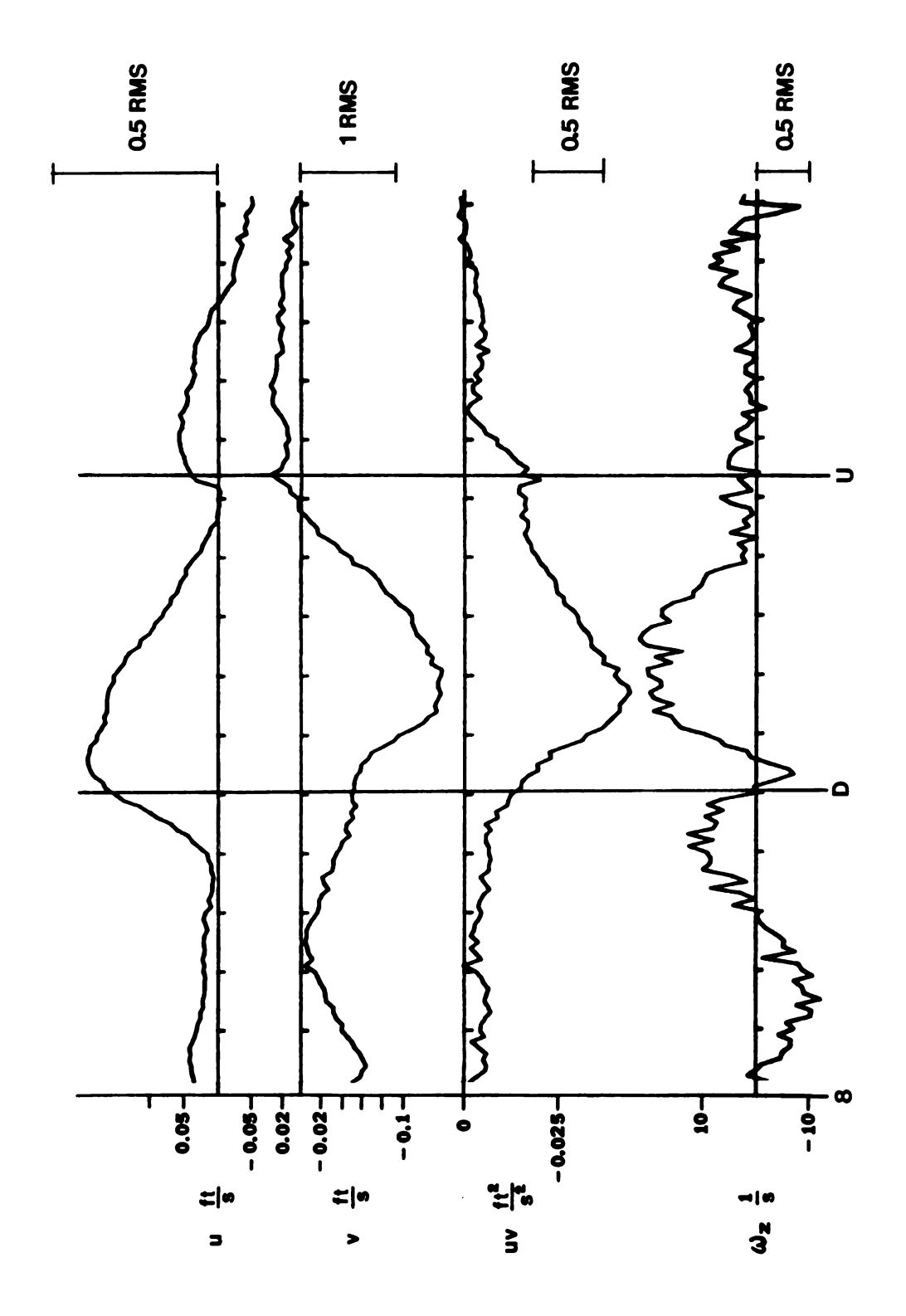
Ensemble Averaged Signals of Positive Rings with High Visual Certainty and Centered Pockets in Early Stages After Removing Three Samples Figure 27b



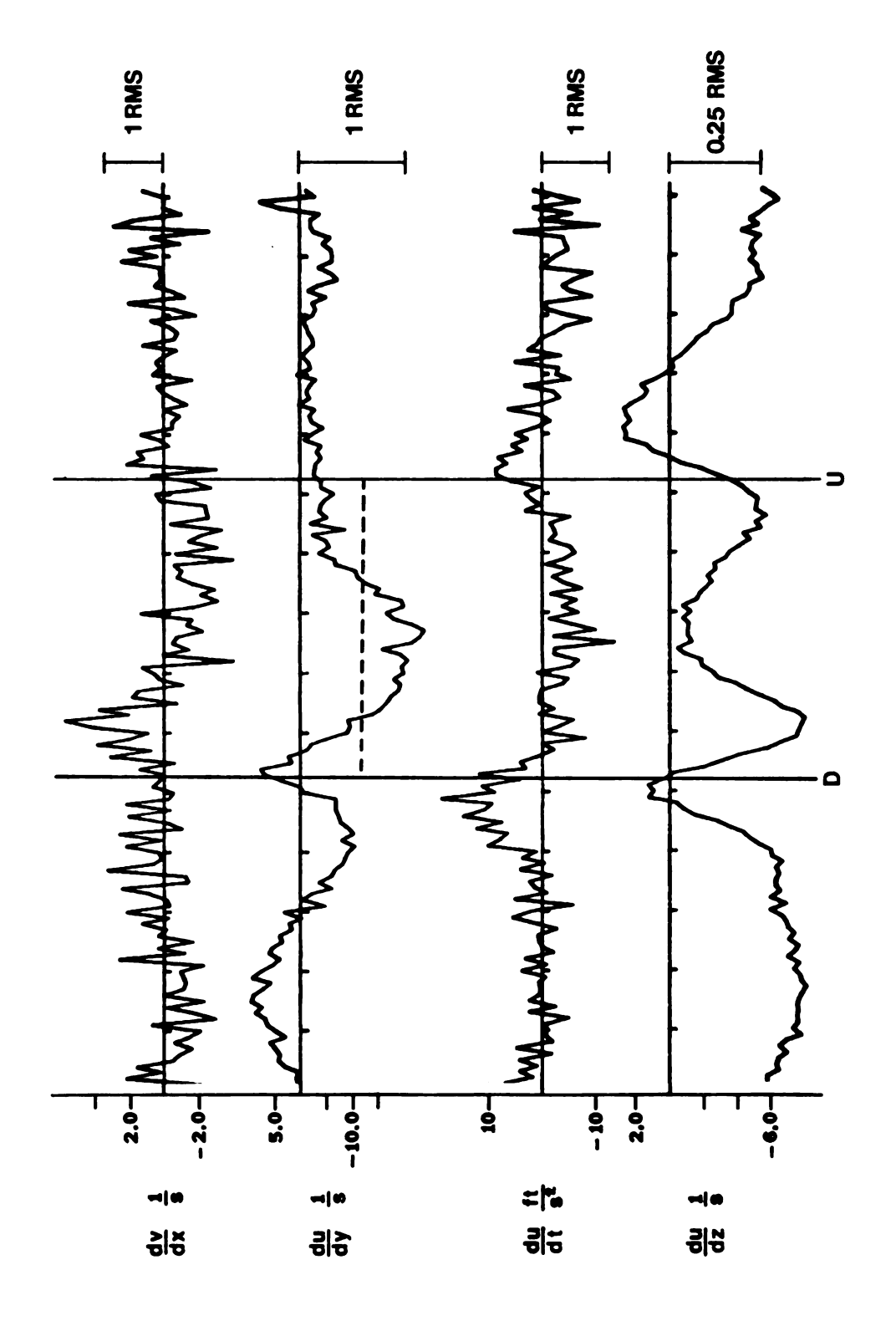
Ensemble Averaged Signals of Negative Rings with High Visual Certainty and Centered Pockets in Early Stages After Removing Two Samples Figure 28a



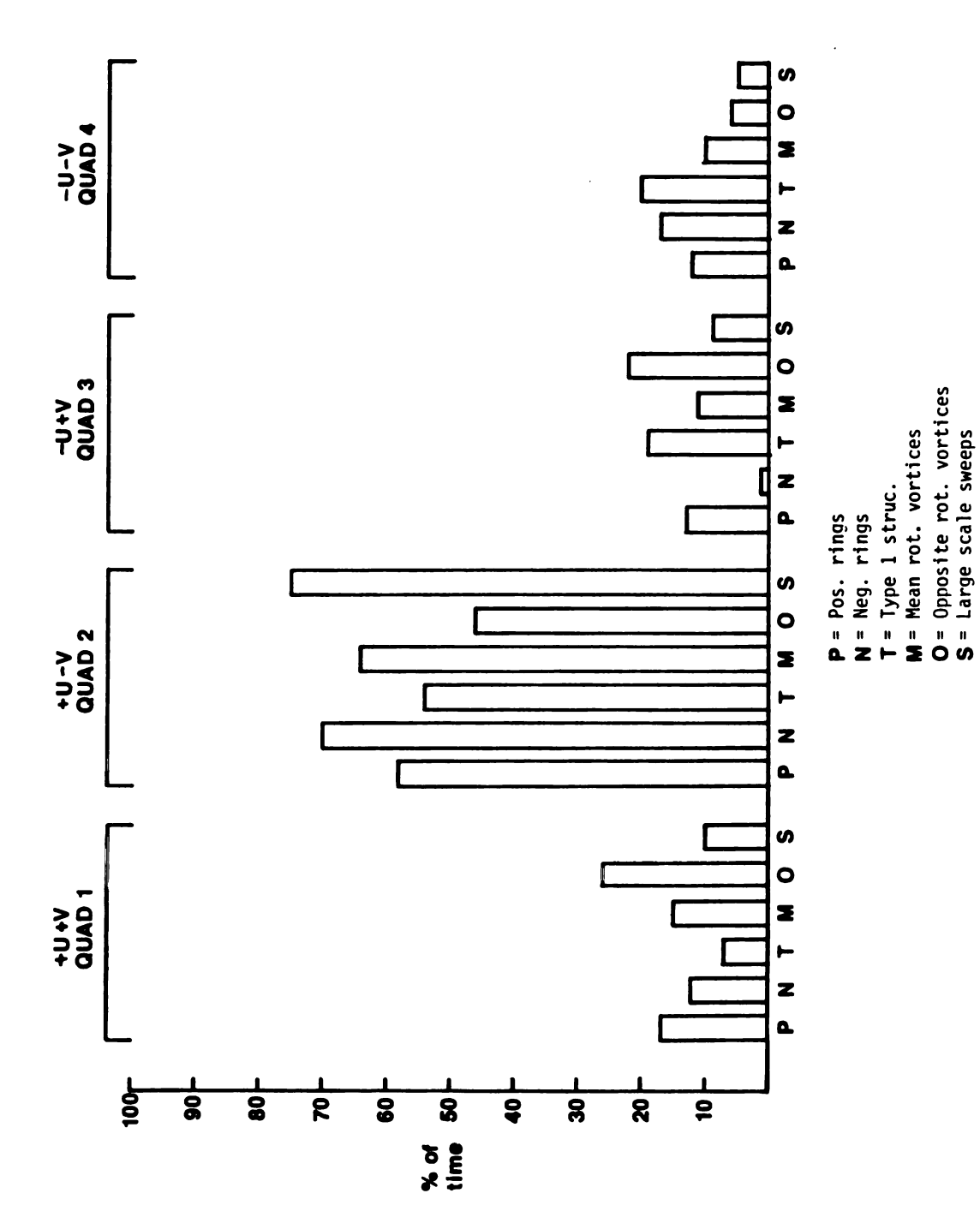
Ensemble Averaged Signals of Negative Rings with High Visual Certainty and Centered Pockets in Early Stages After Removing Two Samples Figure 28b



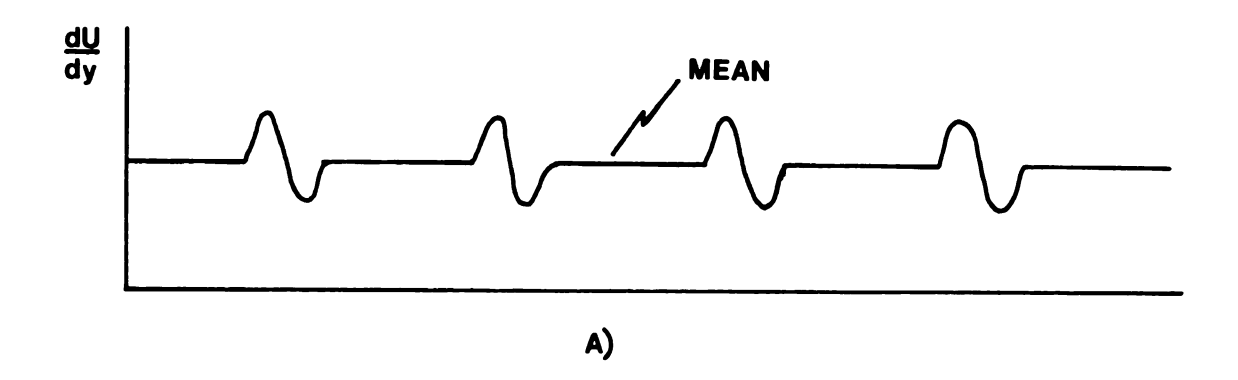
Ensemble Averaged Signals of Type 1 Structures with High Visual Certainty and Pockets in Early Stages After Removing Three Samples Figure 29a



Ensemble Averaged Signals of Type 1 Structures with High Visual Certainty and Pockets in Early Stages After Removing Three Samples Figure 29b



Percentage of the Time that the Probe Passes Through Causal Structures Which is Spent in Each uv Quadrant. Figure 30.



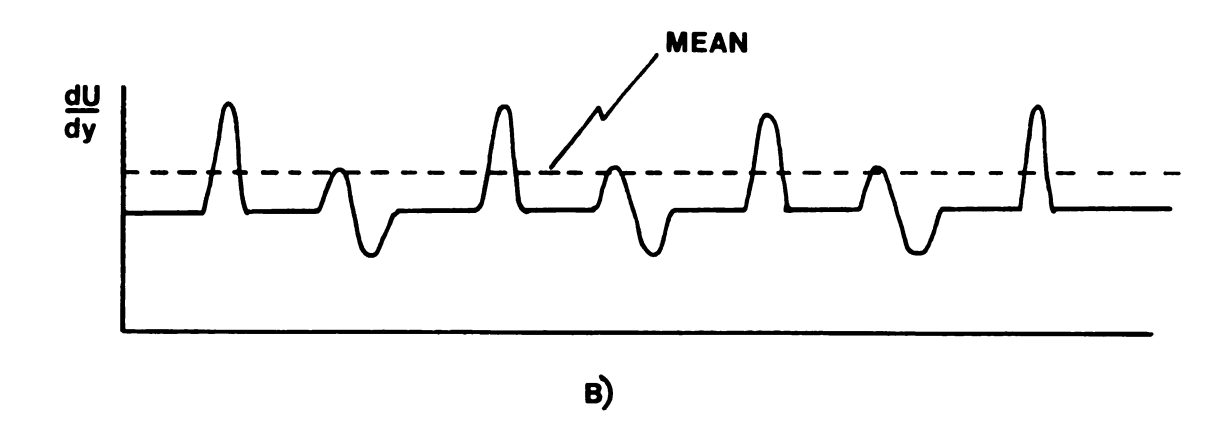


Figure 31. Shifting of the Average Due to the Skewness of a signal.

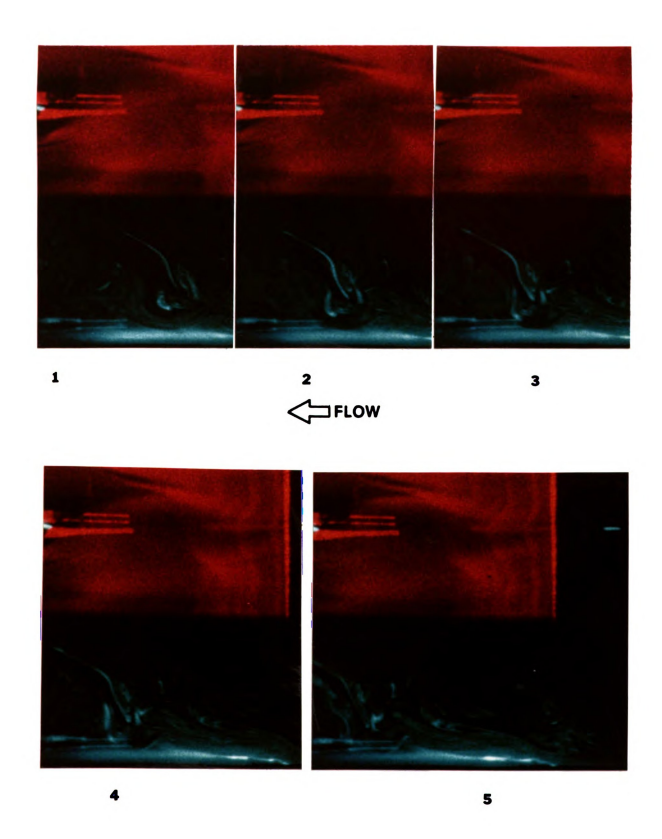


Figure 32a. Sequence showing a positive vortex pair moving wallward with centered pocket occurring in front of probe.

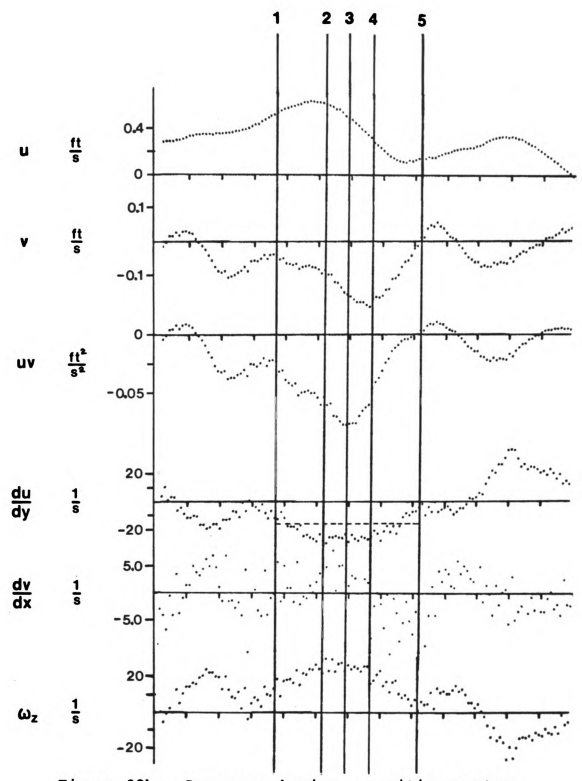


Figure 32b. Sequence showing a positive vortex pair moving wallward with centered pocket occurring in front of probe.

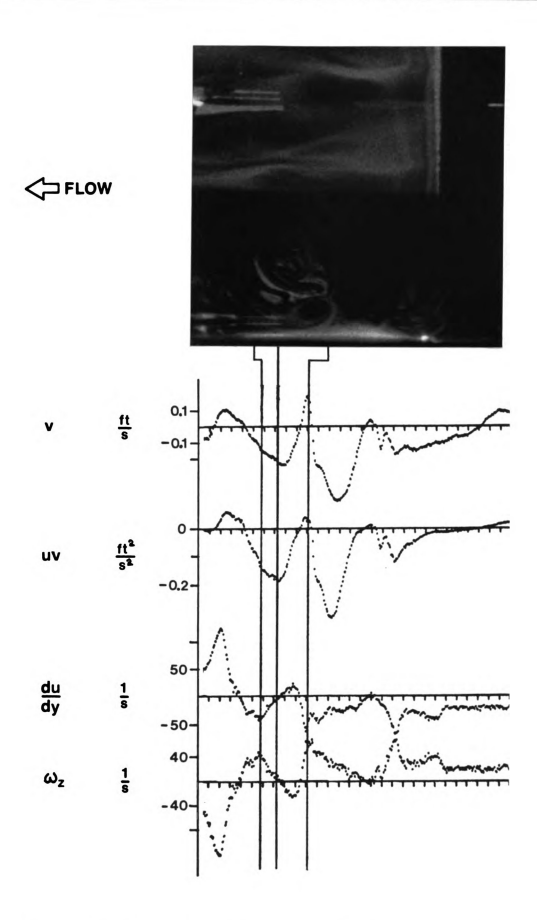


Figure 33. Positive vortex pair with probe at center.

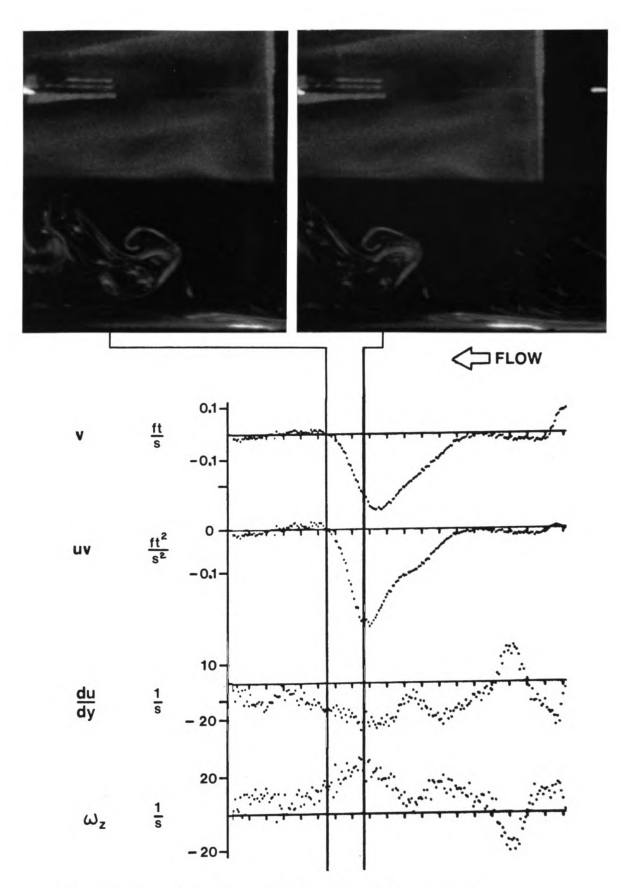


Figure 34. Sequence showing negative vortex pair passing above the probe.

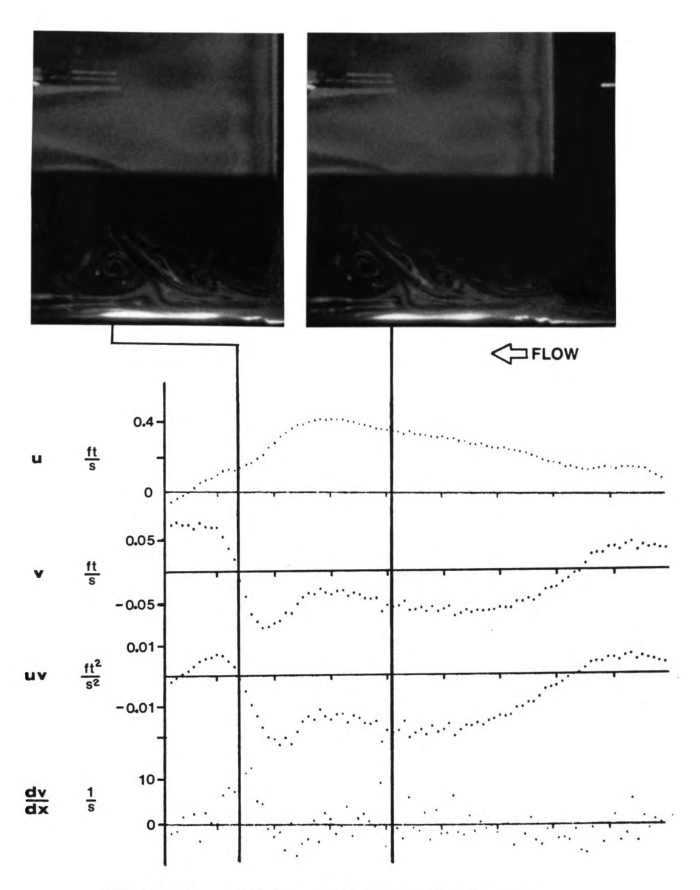


Figure 35. Sequence showing negative vortex pair and small off-center pocket.

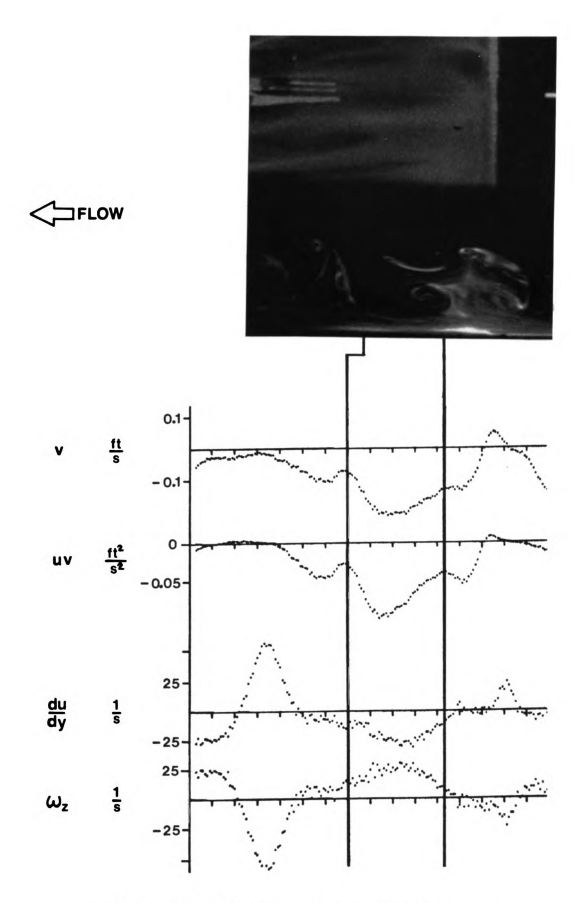


Figure 36. Example of type 1 structure.

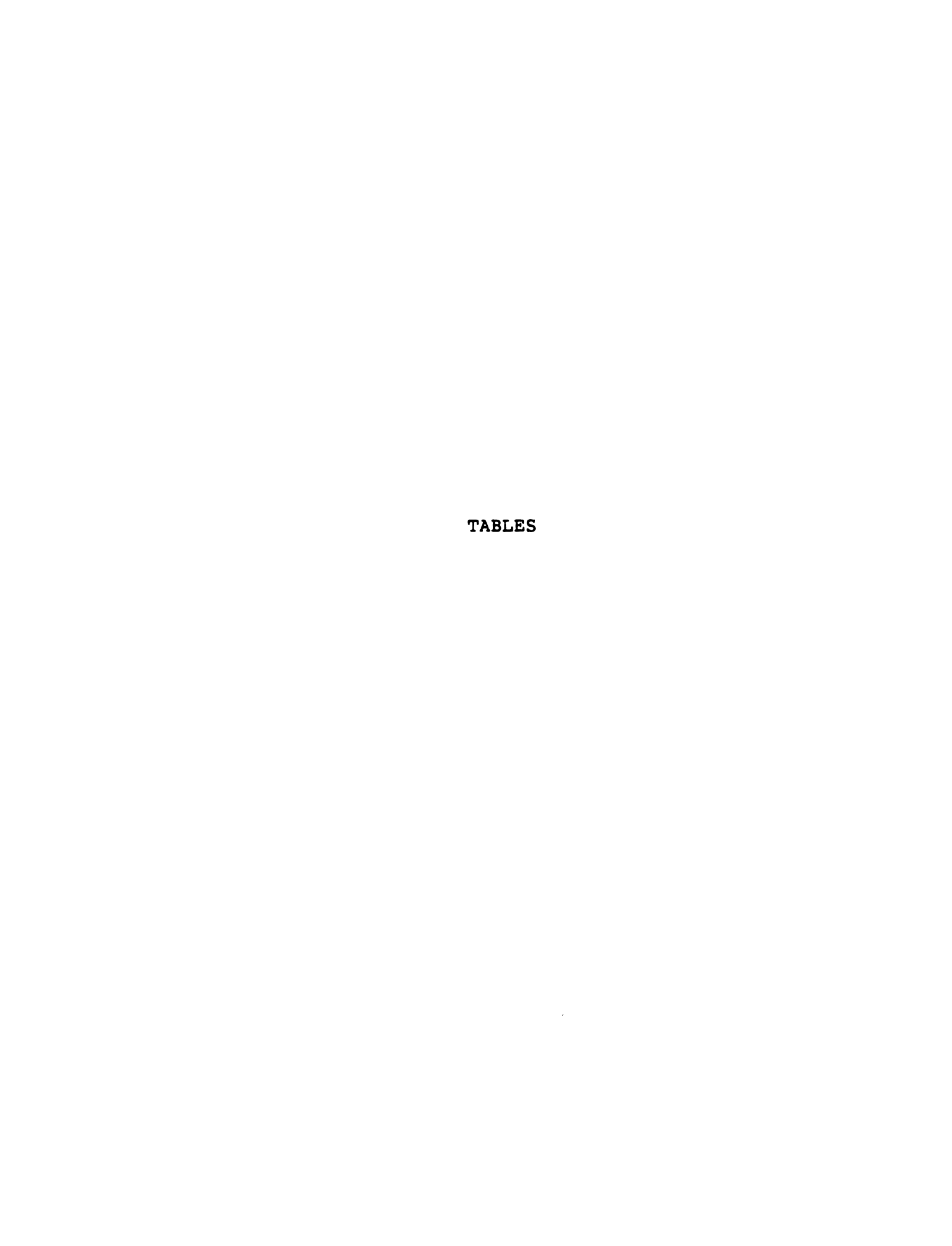


TABLE 1 Average Velocities for Each Data Set

DATA SET	Ū from x ft ∕sec	∇ from x ft /sec	$rac{\overline{U}}{U}$ bottom parallel ft /sec	$\overline{\overline{\mathtt{U}}}$ top parallel ft /sec
1	1.869	-0.02435	1.811	1.896
2	1.870	-0.01995	1.942	2.009
3	1.978	-0.03382	1.873	1.941
4	1.908	-0.02550	1.882	1.948
5	1.926	-0.01995	1.946	2.010
6	1.758	-0.02409	1.754	1.829
7	1.934	-0.03815	1.938	2.038
8	1.834	-0.02398	1.847	1.937
9	1.882	-0.02558	1.874	1.961
10	1.868	-0.01337	1.891	1.974
11	1.979	-0.03965	1.950	2.036
12	1.723	-0.01636	1.742	1.838
13	1.717	-0.01322	1.839	1.919
14	2.022	-0.04453	1.970	2.055
15	1.797	-0.02732	1.811	1.888
16	1.800	-0.01015	1.829	1.927
17	1.857	-0.02588	1.926	2.008
AVERAGE	1.866	-0.02505	1.872	1.954
STD. DEV.	0.088	0.00960	0.069	0.068

TABLE 2 Average Total Quantities for Each Data Set

DATA SET	dŪ/dy 1/sec	dV/dx 1/sec x10-3	dŪ∕dt ft/sec2	d√/dt ft/sec2	duv/dt ft2/sec3 x10-4	wz l/sec	dŪ/dz 1/sec
1	25.47	-2.956	0.3258	0.0000	-2.229	-25.47	0.9374
2	20.28	7.581	0.3382	-0.1288	-5.194	-20.27	-6.3501
3	20.30	2.701	0.4198	0.1247	2.891	-20.30	4.2377
4	19.78	7.938	0.3478	-0.1816	-6.728	-19.77	-0.4580
5	19.13	6.946	0.2938	-0.2076	0.262	-1912	-3.0810
6	22.39	-5.004	0.3199	0.0217	7.145	-22.40	-2.0135
7	30.11	-0.110	0.1868	-0.4614	-0.025	-30.12	-3.2310
8	26.90	-4.922	0.3587	-0.4614	0.265	-26.91	-3.4554
9	26.08	-4.010	0.1755	-0.4614	-0.011	-26.08	-2.1686
10	24.94	-0.219	0.3919	-0.4614	0.016	-24.96	-3.8976
11	26.00	0.153	0.3960	-0.4614	-0.618	-25.99	-0.8116
12	28.70	6.010	0.3340	0.0214	-0.133	-28.69	-4.0499
13	24.04	2.476	0.1466	0.0217	0.188	-24.03	-9.7719
14	25.52	-7.434	0.3040	0.0217	-6.831	-25.53	0.5678
15	23.14	9.801	0.3766	0.0217	-4.402	-23.13	-3.1510
16	29.40	5.980	0.4244	0.0217	-0.557	-29.40	-4.6804
17	24.72	6.731	0.3328	0.0217	-2.431	-24.72	-6.6222
AVG.	24.70	1.005	0.3272	-0.2624	-0.209	-24.70	-2.430
S.D.	3.33	8.935	0.0826	0.5238	0.786	3.33	3.561

TABLE 3 u Statistics for Each Data Set

DATA SET	AVERAGE FT/SEC	STANDARD DEVIATION FT/SEC	SKEWNESS FACTOR	FLATNESS FACTOR
1	-0.0	0.4321	-0.2980	2.197
2	-0.0	0.4880	-0.4607	2.239
3	-0.0	0.3820	-0.6250	3.379
4	-0.0	0.4623	-0.4857	2.418
5	-0.0	0.4907	-0.5121	2.286
6	0.0	0.4549	-0.5329	2.605
7	-0.0	0.4578	-0.7891	2.957
8	0.0	0.4604	-0.5402	2.502
9	0.0	0.4428	-0.2581	2.248
10	0.0	0.4527	-0.6640	2.695
11	-0.0	0.4486	-0.4117	2.442
12	0.0	0.5023	-0.3985	2.210
13	0.0	0.4648	0.0571	2.019
14	-0.0	0.5082	-0.9618	3.453
15	-0.0	0.4400	-0.1717	2.419
16	-0.0	0.5022	-0.0710	2.093
17	0.0	0.4512	-0.2404	2.214
AVERAGE	0.0	0.461	-0.433	2.49
STD. DEV.	0.0	0.031	0.257	0.42

TABLE 4 v Statistics for Each Data Set

DATA SET	AVERAGE FT/SEC	STANDARD DEVIATION FT/SEC	SKEWNESS FACTOR	FLATNESS FACTOR
1	-0.0	0.0744	0.5298	4.273
2	-0.0	0.0920	0.7506	4.898
3	0.0	0.0806	-0.3461	4.183
4	0.0	0.0921	0.0698	4.323
5	0.0	0.0762	0.0737	3.860
6	-0.0	0.0882	0.4740	4.091
7	0.0	0.0945	-0.1418	3.806
8	-0.0	0.0808	0.2196	4.915
9	0.0	0.0805	-0.3571	3.346
10	0.0	0.0754	0.0358	3.464
11	-0.0	0.1065	-0.2877	4.188
12	-0.0	0.1046	0.3148	5.224
13	-0.0	0.0907	0.0919	3.003
14	0.0	0.0828	-0.3389	4.410
15	0.0	0.0969	-0.2060	3.811
16	0.0	0.0836	0.1025	3.381
17	0.0	0.0942	0.0512	3.560
AVERAGE	0.0	0.0879	0.0610	4.04
STD. DEV.	0.0	0.0097	0.33	0.61

TABLE 5 uv Statistics for Each Data Set

DATA SET	AVERAGE FT**2/SEC**2	STANDARD DEVIATION FT**2/SEC**2	SKEWNESS FACTOR	FLATNESS FACTOR
1	-0.01338	0.03176	-1.722	9.135
2	-0.02307	0.04236	-1.705	7.220
3	-0.01165	0.02953	-1.439	7.400
4	-0.02467	0.04182	-1.953	8.295
5	-0.01662	0.03438	-2.080	10.027
6	-0.01708	0.03502	-1.454	8.057
7	-0.01815	0.03882	-1.729	8.390
8	-0.01419	0.03951	-2.569	13.264
9	-0.01370	0.02995	-0.912	5.268
10	-0.01733	0.03261	-1.348	5.497
11	-0.02411	0.04895	-1.944	8.621
12	-0.02090	0.04192	-1.538	6.601
13	-0.01928	0.03538	-0.378	5.282
14	-0.01849	0.04403	-2.047	8.208
15	-0.01670	0.04383	-1.575	7.763
16	-0.02370	0.03899	-1.427	5.656
17	-0.02202	0.03954	-1.407	5.905
AVERAGE	-0.0185	0.0381	-1.60	7.68
STD. DEV	. 0.0040	0.0055	0.49	2.03

TABLE 6 dU/dt Statistics for Each Set

DATA SET	AVERAGE FT/SEC**2	STANDARD DEVIATION FT/SEC**2	SKEWNESS FACTOR	FLATNESS FACTOR
1	0.3258	11.14	0.8608	6.132
2	0.3382	14.11	1.2853	9.576
3	0.4198	11.97	0.8301	5.291
4	0.3478	11.94	0.8842	5.214
5	0.2938	13.34	1.0254	7.363
6	0.3199	13.18	0.6368	4.663
7	0.1868	12.70	0.9744	6.929
8	0.3587	12.33	0.9393	5.844
9	0.1755	13.03	1.1769	7.127
10	0.3919	10.90	0.1592	5.602
11	0.3960	14.81	1.4169	8.958
12	0.3340	13.42	1.4391	9.798
13	0.1466	12.23	0.5845	4.072
14	0.3040	13.23	1.4956	8.116
15	0.3766	14.62	1.0684	6.174
16	0.4244	12.50	1.2123	6.941
17	0.3328	13.32	0.5664	5.050
AVERAGE	0.322	12.9	0.974	6.64
STD. DEV.	0.080	1.1	0.356	1.70

TABLE 7 dV/dt Statistics for Each Set

DATA SET	AVERAGE FT/SEC**2	STANDARD DEVIATION FT/SEC**2	SKEWNESS FACTOR	FLATNESS FACTOR
1	0.0000	5.823	-0.1471	4.125
2	-0.1288	6.933	-0.2136	6.261
3	0.1247	6.773	-0.1231	8.099
4	-0.1816	6.608	-0.6674	9.291
5	-0.2076	6.641	-0.1507	7.315
6	0.0217	6.313	-0.4785	4.688
7	-0.4614	6.855	-0.1588	5.798
8	-0.4614	5.918	-0.1055	4.150
9	-0.4614	6.589	-0.1934	8.078
10	-0.4614	5.706	0.1007	4.344
11	-0.4614	7.850	-0.6569	9.129
12	0.0217	6.461	-0.1716	7.390
13	0.0217	5.546	-0.0974	4.335
14	0.0217	6.836	-0.5254	8.773
15	0.0217	6.762	-0.2427	4.653
16	0.0217	6.544	-0.1662	8.090
17	0.0217	6.305	-0.0426	3.950
AVERAGE		6.50	-0.238	6.38
STD. DEV.		0.55	0.215	1.98

TABLE 8 dU/dy Statistics for Each Set

DATA SET	AVERAGE 1/sec	STANDARD DEVIATION 1/sec	SKEWNESS FACTOR	FLATNESS FACTOR
1	25.47	21.18	0.673	3.895
2	20.28	22.37	1.189	5.520
3	20.30	20.98	0.335	3.250
4	19.78	20.90	0.739	3.493
5	19.13	20.70	0.906	4.175
6	22.39	22.54	0.994	4.776
7	30.11	21.91	0.805	3.295
8	26.90	18.83	1.704	9.088
9	26.08	20.26	0.789	5.238
10	24.94	18.71	0.655	3.859
11	26.00	24.59	1.351	5.636
12	28.70	20.53	0.800	4.689
13	24.04	19.21	0.599	3.511
14	25.52	22.85	0.818	4.275
15	23.14	21.85	0.874	4.638
16	29.40	20.20	0.555	3.258
17	24.72	21.24	0.920	3.849
AVERAGE	24.52	21.11	0.829	4.497
STD. DEV.	3.345	1.514	0.371	1.413

TABLE 9 dv/dx Statistics for Each Set

DATA SET	AVERAGE 1/SEC	STANDARD DEVIATION 1/SEC	SKEWNESS FACTOR	FLATNESS FACTOR
1	-0.0030	3.129	0.1471	4.125
2	0.0076	3.606	0.2136	6.261
3	0.0027	3.486	0.1231	8.099
4	0.0079	3.457	0.6674	9.291
5	0.0070	3.402	0.1507	7.315
6	-0.0050	3.556	0.4785	4.688
7	-0.0110	3.495	0.1588	5.798
8	-0.0049	3.176	0.1055	4.150
9	-0.0040	3.468	0.1934	8.078
10	-0.0219	3.002	-0.100	4.344
11	0.0153	3.952	0.6569	9.129
12	0.0061	3.679	0.172	7.390
13	0.0025	3.085	0.097	4.335
14	-0.0074	3.389	0.525	8.773
15	0.0098	3.709	0.243	4.653
16	0.0060	3.558	0.166	8.090
17	0.0067	3.298	0.043	3.950
AVERAGE	0.0008	3.44	0.238	6.38
STD. DEV.	0.0092	0.25	0.215	1.98

DATA SET	AVERAGE 1/SEC	STANDARD DEVIATION 1/SEC	SKEWNESS FACTOR	FLATNESS FACTOR
1	-25.47	21.22	-0.6410	3.856
2	-20.27	22.72	-1.1912	5.735
3	-20.30	21.14	-0.2902	3.310
4	-19.77	21.18	-0.6593	3.410
5	-19.12	20.81	-0.8541	4.190
6	-22.40	23.12	-0.9994	4.866
7	-30.12	22.25	-0.7782	3.318
8	-26.91	19.02	-1.6389	9.020
9	-26.08	20.69	-0.7088	4.958
10	-24.96	18.95	-0.6104	3.916
11 .	-25.99	25.07	-1.2752	5.583
12	-28.69	20.86	-0.7594	4.632
13	-24.00	19.32	-0.5361	3.446
14	-25.53	23.23	-0.7462	4.226
15	-23.13	22.05	-0.8223	4.593
16	-29.40	20.42	-0.4740	3.230
17	-24.72	21.37	-0.8892	3.826
AVERAGE	-24.5	21.4	-0.816	4.48
STD. DEV.	3.3	1.6	0.322	1.40

TABLE 11 du/dz Statistics for Each Data Set

DATA SET	AVERAGE 1/SEC	STANDARD DEVIATION 1/SEC	SKEWNESS FACTOR	FLATNESS FACTOR
1	0.940	20.25	0.057	3.709
2	-6.350	21.33	-0.119	3.636
3	4.240	18.80	-0.195	3.577
4	-0.460	15.66	0.558	4.075
5	-3.080	18.70	-0.104	3.931
6	-2.010	20.22	0.183	3.572
7	-3.230	19.83	-0.107	3.031
8	-3.460	22.04	0.236	3.594
9	-2.170	22.07	-0.051	3.685
10	-3.900	20.50	0.228	3.484
11	-0.810	23.51	-0.007	3.785
12	-4.050	22.84	-0.201	3.113
13	-9.770	23.55	0.311	2.959
14	0.570	20.29	-0.674	4.772
15	-3.150	23.61	-0.016	3.413
16	-4.680	24.33	-0.384	3.660
17	0.660	23.79	-0.256	2.712
AVERAGE	-2.82	21.26	-0.03	3.57
STD. DEV.	3.24	2.32	0.29	0.47

TABLE 12 duv/dt Statistics for Each Data Set

DATA SET	AVERAGE FT**2/SEC**3	STANDARD DEVIATION FT**2/SEC**3	SKEWNESS FACTOR	FLATNESS FACTOR
1	-0.0002	2.585	0.2892	8.699
2	-0.0005	3.614	0.3552	8.426
3	0.0003	2.576	0.3284	9.679
4	-0.0007	2.985	-0.3287	10.751
5	0.0026	3.244	0.8574	16.311
6	0.0007	2.856	-0.1911	7.589
7	-0.0248	3.141	0.0787	9.254
8	0.0027	2.773	0.2743	8.072
9	-0.0108	2.968	-0.3876	12.134
10	0.0155	2.508	-0.1421	7.878
11	-0.0062	3.734	-0.2340	14.973
12	-0.0013	3.298	-0.1678	12.697
13	0.0019	2.808	0.1174	6.239
14	-0.0068	3.116	-0.3666	11.328
15	-0.0044	3.437	-0.2346	11.681
16	-0.0056	3.835	-0.0975	17.388
17	-0.0002	3.029	-0.4610	7.376
AVERAGE	-0.002	3.08	-0.018	10.61
STD. DEV	. 0.008	0.40	0.349	3.26

TABLE 13 $\overline{\overline{U}}$ Statistics for Each Data Set

DATA SET	AVERAGE FT/SEC	STANDARD DEVIATION FT/SEC	SKEWNESS FACTOR	FLATNESS FACTOR
1	1.861	0.4128	-0.2812	2.617
2	1.923	0.4176	-0.5328	2.293
3	1.943	0.4085	-0.2644	2.479
4	1.912	0.4683	-0.4517	2.439
5	1.952	0.4614	-0.5140	2.439
6	1.775	0.4695	-0.2989	2.363
7	1.961	0.4247	-0.4114	2.336
8	1.863	0.4947	-0.3636	2.252
9	1.900	0.5174	-0.4019	2.314
10	1.900	0.4621	-0.9020	3.306
11	1.986	0.4740	-0.3617	2.291
12	1.756	0.5018	-0.3402	2.269
13	1.798	0.4674	-0.2207	2.068
14	2.017	0.4654	-0.6278	2.742
15	1.823	0.5163	-0.3371	2.183
16	1.839	0.4675	-0.0917	2.402
17	1.912	0.4377	-0.1503	2.106
AVERAGE	1.89	0.463	-0.385	2.41
STD. DEV.	0.074	0.034	0.190	0.29

VISCOUS LENGTH SCALE DETERMINED USING NORMAL VELOCITY

Positive orientated rings (56) Average $1^{+}(t2) = 108$ Std. dev. Average 1⁺(t1) = 51 Std. dev. = 35 Negative orientated rings (14) Average $1^+(t2)$ = 35 Std. dev. Average $1^+(t1) =$ Std. dev. Type 1 structures (11) Average $1^+(t2) = 120$ Std. dev. Average $1^{+}(t1) = 58$ Std. dev. = 40 Mean rotating vortices (11) Average $1^{+}(t2) = 124$ Std. dev. Average $1^+(t1)$ = Std. dev. Opposite rotating vortices (6) Average $1^+(t2) = 81$ Std. dev. 23 1⁺(t1) = Average Std. dev. Large scale sweeps (11) Average 1⁺(t2) = 240 Std. dev. = 54

Table 14. Viscous Length Scale Determined Using Normal Velocity.

REYNOLD STRESS AVERAGES IN UV QUADRANTS

Positive orientated rings

All Quadrants = -0.0243 Quad 1 (+u+v) = 0.0137 Quad 2 (+u-v) = -0.0418 Quad 3 (-u+v) = -0.0314 Quad 4 (-u-v) = 0.0159

Negative orientated rings

All Quadrants = -0.0386 Quad 1 (+u+v) = 0.0106 Quad 2 (+u-v) = -0.0588 Quad 3 (-u+v) = -0.0064 Quad 4 (-u-v) = 0.0081

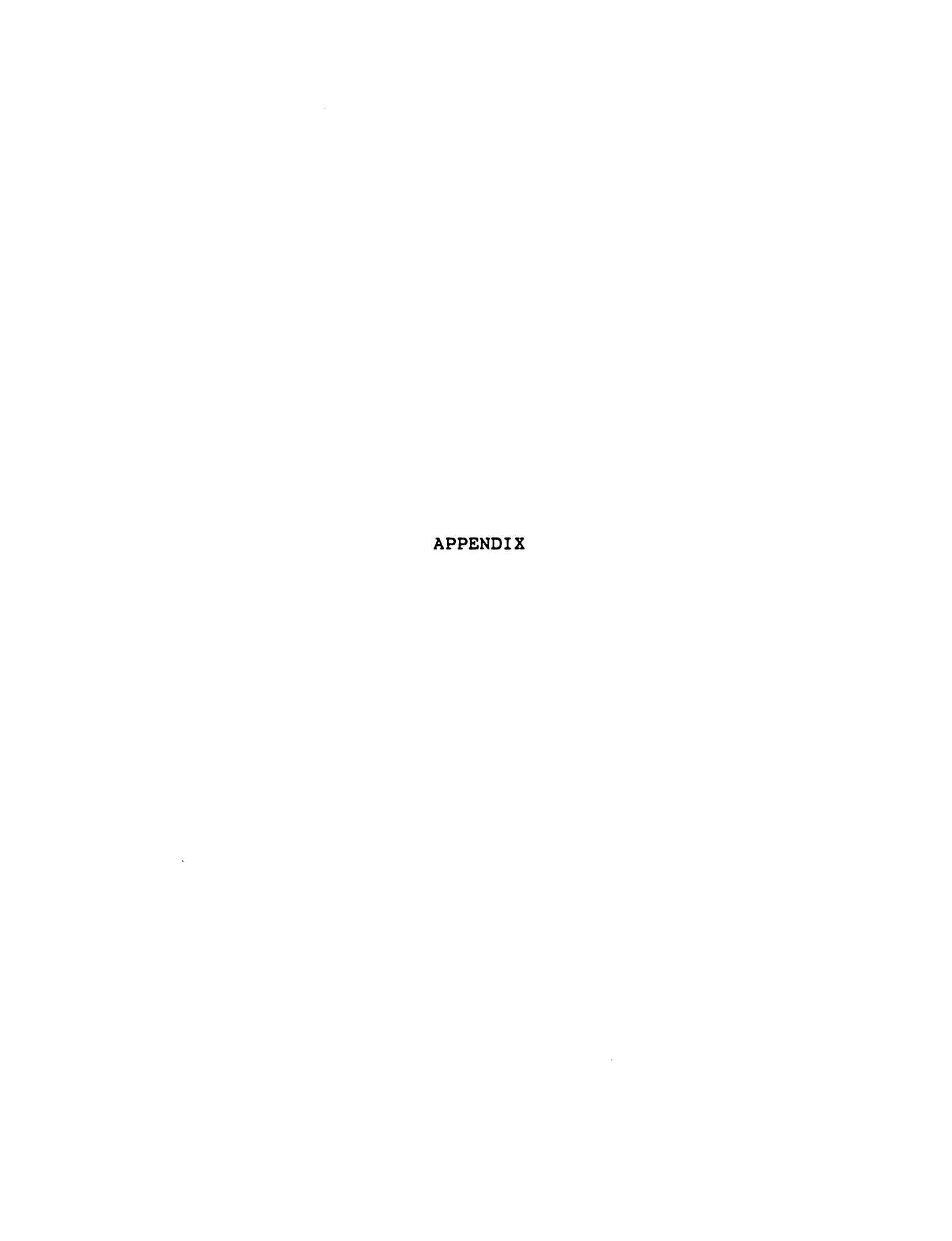
Large scale sweeps

All Quadrants = -0.0284 Quad 1 (+u+v) = 0.0078 Quad 2 (+u-v) = -0.0376 Quad 3 (-u+v) = -0.0151 Quad 4 (-u-v) = 0.0102

Table 15. Reynolds Stress Averages in uv Quadrants

TABLE 16	Comparison of uv QUAD 1	Averages with QUAD 2	Brodkey, QUAD 3	et al., 1973 QUAD 4
* <u>uv</u> uv	-0.24	0.63	0.78	-0.20
Pos. Pairs	-0.74	2.26	1.70	-0.86
HC	(308%)	(359%)	(217%)	(431%)
Neg. Pairs	-0.57	3.18	0.34	-0.44
HC,CT	(238%)	(505%)	(44%)	(220%)
Pos. Pairs	-0.76	2.17	2.13	-0.91
HC,CT,ES	(317%)	(344%)	(273%)	(455%)
* % Time	0.20	0.35	0.28	0.17
Pos. Pairs	0.17	0.58	0.13	0.12
HC	(85%)	(166%)	(46%)	(71%)
Neg. Pairs	0.12	0.70	0.01	0.17
HC,CT	(60%)	(200%)	(4%)	(100%)
Pos. Pairs	0.19	0.58	0.11	0.12
HC,CT,ES	(95%)	(166%)	(39%)	(71%)
Neg. Pairs	0.18	0.64	0.01	0.16
HC,CT,ES	(90%)	(183%)	(4%)	(94%)
* <u>uw/uv</u> % Time	0.75	-1.25	-1.85	0.75
Pos. Pairs	4.68	-4.20	-14.07	7.75
HC	(623%)	(336%)	(760%)	(1032%)
Neg. Pairs	5.14	-4.89	-37.1	2.78
HC,CT	(685%)	(391%)	(2006%)	(370%)
Pos. Pairs	6.78	-4.03	-20.90	8.21
HC,CT,ES	(905%)	(324%)	(1128%)	(1094%)
*Avg. Durat	ion 1.00	1.72	1.71	1.00
Pos. Pairs	1.00	3.14	0.77	0.71
Neg. Pairs HC,CT	1.00	5.83	0.01	1.42
Pos. Pairs HC,CT,ES	1.00	3.05	0.52	0.63
Neg. Pairs HC,CT,ES	1.00	3.56	0.06	0.89

HC = High Vis. Certainty, CT = Centered, ES = Early Stages * Brodkey et al.



APPENDIX A: CALIBRATION PROCEDURE

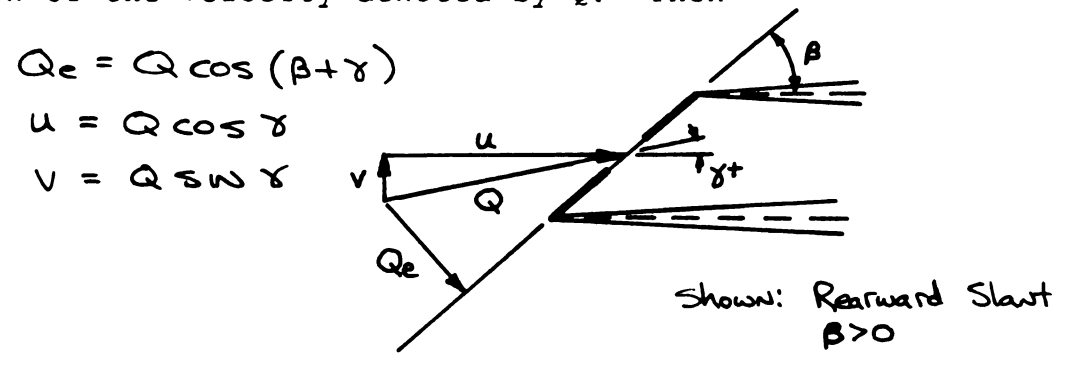
The following is a description of the method used to calibrate the four element hot-wire probe. An analysis of the method followed by the calibration procedure is described below.

Analysis

The method assumes that the hot-wire voltage depends only on the velocity component normal to the wire axis (called Q effective) and that the streamwise and normal components of velocity can be determined from the X-wire signals by simple geometry. The following analysis then determines the real angle between the hot wires in the X probe to be used in the geometric relation.

From the Collis and Williams relationship we have

where Qe is the effective velocity normal to the wire axis. Consider the wire to be mounted at an angle (S) to the probe axis. Let 7 be the angle between the probe axis and the direction of the velocity denoted by Q. Then



$$Qe = Q \cos(\beta + \delta)$$

$$Qe = Q (\cos\beta \cos \gamma - \sin\beta \sin\gamma)$$

$$Qe = u \cos\beta - v \sin\beta$$

Now let us assume that the angle between the wire axis and the probe axis is unknown but very close to 45 degrees. Let

$$\beta = \overline{4} + \delta \beta$$

$$\cos(\beta) = \cos(\overline{4} + \delta \beta)$$

Assuming $\delta \beta$ is very small

Now

$$Q_{e} = u(\frac{2}{5}(1-5\beta)) - v(\frac{2}{5}(1+5\beta))$$

$$Q_{e} = \frac{2}{5}(u(1-5\beta) - v(\frac{2}{5}(1+5\beta))$$

$$Q_{e} = \frac{2}{5}[(u-v) - 5\beta(u+v)]$$

Substituting in the Collis and Williams relationship

Let

For the forward slanting wire, i.e. where $\beta < 0$, similar results follow.

Denoting forward slanting wire by 'F' and rearward slanting wire by 'R', we have

Likewise for the forward slanting wire

$$\beta = -\frac{\pi}{4} + \delta \beta_{F}$$

$$\cos(\beta) \approx \cos(-\frac{\pi}{4})(1) - \sin(-\frac{\pi}{4})(\delta \beta_{F})$$

$$\approx \frac{\pi}{2} (1 + \delta \beta_{F})$$

$$\sin(\beta) \approx \sin(-\frac{\pi}{4})(1) + \cos(-\frac{\pi}{4})(\delta \beta_{F})$$

$$\approx \frac{\pi}{2} (\delta \beta_{F} - 1)$$

For this case
$$Q_{e} = u(\frac{1}{2}(1+\delta B_{F})) - v(\frac{1}{2}(\delta B_{F}-1))$$

$$Q_{e} = \frac{1}{2}(u(1+\delta B_{F}) - v(\delta B_{F}-1))$$

Similarly

Rearranging we find

$$ER = AR + BR \left(1 - \delta BR\right) \left[u - \left(\frac{1 + \delta BR}{1 - \delta BR}\right) \sqrt{J}^{R}\right]$$

PLEASE NOTE:

Page 263 is missing in number only. No text is missing. Filmed as received.

UNIVERSITY MICROFILMS INTERNATIONAL.

Now if we assume $\delta \mathcal{G}$ is small for both the wires, then

1+5B= 21

Let
$$C_{R} = \left(\frac{1 + \delta B_{R}}{1 - \delta B_{R}}\right)$$

$$C_{F} = \left(\frac{1 - \delta B_{F}}{1 + \delta B_{F}}\right)$$

$$E_{R}^{2} = A_{R} + B_{R} \left[u - C_{R} V \right]^{M_{R}}$$

$$E_{F}^{2} = A_{F} + B_{F} \left[u + C_{F} V \right]^{M_{F}}$$
Now, if the probe is aligned with the velocity vector then $V_{R}^{2} = 0$ and $V_{R}^{2} = 0$. Therefore $V_{R}^{2} = 0$ and we arrive at

Let

$$Ar|_{T=0} = \overline{A}_{R}$$

$$Ar|_{T=0} = \overline{A}_{F}$$

$$B'_{r}|_{T=0} = \overline{B}_{R}$$

$$E^{2}|_{T=0} = \overline{E}^{2}_{F}$$

$$E^{2}|_{T=0} = \overline{E}^{2}_{F}$$

$$Mr|_{T=0} = \overline{M}_{F}$$

$$Mr|_{T=0} = \overline{M}_{F}$$

This represents data from a calibration run where the probe axis is in the velocity direction. During the calibration we determine

Now, determining the constants $C_{\mathbf{F}}$, $C_{\mathbf{F}}$ [u-CRV] = 1 [ER-ART U-CRV = [to [ER - AR]] /UR

Likewise

$$\begin{bmatrix} u + c_F v \end{bmatrix}^{\overline{n}_F} = \frac{1}{6} \begin{bmatrix} \overline{E}_F^2 - \overline{A}_F \end{bmatrix}$$

$$u + c_F v = \begin{bmatrix} \frac{1}{6} \end{bmatrix} (\overline{E}_F^2 - \overline{A}_F) \end{bmatrix}^{\gamma_{\overline{n}_F}}$$

$$c_F = \frac{1}{6} \begin{bmatrix} \frac{1}{6} \end{bmatrix} (\overline{E}_F^2 - \overline{A}_F) \end{bmatrix}^{\gamma_{\overline{n}_F}} - \frac{U}{6}$$

Let

$$R = \left[\frac{1}{3R}(E_R^2 - \overline{A}_R)\right]^{1/\overline{n}_R}$$

$$F = \left[\frac{1}{3F}(E_R^2 - \overline{A}_R)\right]^{1/\overline{n}_R}$$

Then

$$R = \left[\frac{1}{16R}(E_R^2 - \overline{A}_R)\right]^{1/\overline{u}_R}$$

$$F = \left[\frac{1}{16F}(E_F^2 - \overline{A}_F)\right]^{1/\overline{u}_F}$$

$$C_R = \sqrt{(u - R)}$$

$$C_F = \sqrt{(F - u)}$$

Next we assume that A, B and n in the Collis and Williams relation do not change with small changes in angle . With the wire at a small angle, say 10 degrees $\frac{1}{2}$

$$U = Q \cos 10^{\circ}$$

$$V = Q \sin 10^{\circ}$$

Now

$$C_R = COT 10^\circ - \frac{R}{Q \sin 10^\circ}$$

$$C_F = \frac{F}{Q \sin 10^\circ} - COT 10^\circ$$

The true angle difference from $\,eta\,\,$ can now be determined

$$\delta \beta_R = \frac{C_R - 1}{1 + C_R}$$

$$\delta \beta_F = \frac{1 - C_F}{1 + C_F}$$

U-CeV = R

Once the error in angle is determined the conversion to velocities can be made easily. Solving for U and V

$$U+CFV = F$$

$$(CF+CR)V = F-R$$

$$V = \frac{F-R}{CF+CR}$$

$$U = (\frac{CF}{CF+CR})R + (\frac{CR}{CF+CR})F$$

The relation for velocity which was used with the pressure transducer begins with Bernoulli's equation applied at a static pressure tap in the wall of the wind tunnel (Ps) and an impact tube located at the centerline of the wind tunnel (Pt). Here the classical assumption of no pressure gradient existing normal to the wall in the boundary layer is employed. Hence, the static and total pressure at the center of the wind tunnel is known. The velocity relation is then

$$\frac{1}{2}V^2 + \frac{1}{\rho}(P_3) = \frac{1}{\rho}(P_T)$$

If we assume an incompressible fluid

$$e = \frac{P_b}{RT}$$

where Pb is the barometric pressure in lb/ft**2. The velocity relation then becomes

$$V^2 = \frac{2RT}{b} \left(\frac{5.206}{70.8}\right) (P_T - P_S)$$

where b is the barometric pressure in inches of mercury, and (Pt-Ps) is in lb/ft**2. Converting (Pt-Ps) into inches of water and substituting standard values for the temperature and baromentric pressure we obtain

$$V^{2} = \frac{2(1716)(530)}{29.5} \left(\frac{5.206}{70.8}\right) (P_{T} - P_{S})_{\text{in}, H_{2}O}$$

Converting (Pt-Ps) into units of torr

The pressure transducer output voltage is linearly proportional to pressure in torr, giving

$$V^2 = 2434 \left(\frac{0.01 \text{ for}}{\text{Volt}}\right) (\text{Volts})$$

This is an example of the relation used with the pressure transducer. The actual temperature and barometric pressure at the time of the measurement must be used in the relation described above.

Calibration procedure

The four element hot-wire probe was calibrated by determining the Collis and Williams constants A, B and n for each wire at angle = 0, as explained in the analysis. This was done by determining the voltages and velocities at eight different speeds with the data acquisition system described in chapter 2. Then using program CALFIT the parameters A, B and n were determined for each wire using least squares. At the speed closest to the local boundary layer velocity of the experiment, the probe was rotated plus and minus 10 degrees from the velocity direction and the voltages determined. This provides enough knowns to solve for the constants CF and CR, and hence the real angle between the X-wires. Only one 10 degree angle voltage was necessary but both plus and minus 10 degree angles were used to check the resulting angle correction. The procedure was as follows:

- 1) Align probe with flow streamline.
- 2) Bring wind tunnel to steady speed.
- 3) Determine actual speed and output voltages with data acquisition system.
- 4) Repeat steps 2 and 3 for next three speeds.
- 5) Rotate probe + 10 degrees and determine speed and voltages.
- 6) Rotate probe 10 degrees and determine speed and voltages.
- 7) Replace probe in streamline direction.
- 8) Repeat steps 2 and 3 for last four speeds.

The values of the parameters for the probe used in this experiment are:

Forward Slant X	A = 8.274 CF = 0.88127	B = 2.804	n = 0.39
Rearward Slant X	A = 9.681 CR = 0.84414	B = 2.639	n = 0.42
Bottom U-wire	A = 8.601	B = 2.748	n = 0.45
Top U-wire	A = 9.883	B = 2.978	n = 0.44

APPENDIX B : Computer programs

```
TABLE
                                                  page
     CFCR
                                                   269
Bl
                                                   270
B2
      CONVEL
     REDUC2
B3
                                                   274
                                                   275
B4
      SEPPTS
      SEP4CH
                                                   276
B5
                                                   277
B6
      STSTCS
                                                   281
В7
      AVGINT
TABLE B1: PROGRAM CFCR
C PROGRAM CFCR CALCULATES
C CORRECTION COEFFICIENTS FOR
C SMALL ANGLE DEVIATIONS OF THE "X" WIRES
C FROM 45 DEGREES.
C OREF REFERENCE FREE STREAM VELOCITY .
C USED TO DETERMINE "X"-WIRE
   ANGLE MISSALIGNMENT CORRECTION.
C REFANG ANGLE "X"-WIRE IS ROTATED TO
 PERFORM MISSALIGNMENT
        CORRECTION.
C EFREF VOLTAGE AT REF VEL AND ANGLE
  FROM FORWARD "X".
С
C ERREF VOLTAGE AT REF VEL AND ANGLE
  FROM REARWARD "X".
C PROGRAM REVISED BY JEFFERY A. LOVETT
С
WRITE(7,111)
111 FORMAT('0','****** USING PROGRAM CRCF ******',/,/,
     1 1X, 'OUTPUT FILE CFCR.DAT CONTAINS THE CONSTANTS')
OPEN (UNIT=14, NAME='DK:CALCRV.DAT', FORM='FORMATTED',
     1 TYPE='OLD', READONLY)
READ(14,*) AXF, BXF, STDF, XNXF
READ(14,*) AXR, BXR, STDR, XNXR
CLOSE (UNIT=14)
TYPE 5
5 FORMAT('0', 'ENTER REFERENCE ANGLE IN DEGREES: ',$)
ACCEPT *, REFANG
10 FORMAT('0', 'ENTER FREE STREAM VELOCITY IN FT/SEC: ',$)
ACCEPT *, QREF
```

```
TYPE 11
11 FORMAT('0', 'ENTER VOLTAGE OF THE FORWARD SLANTING X, EFREF'/)
TYPE *, '
ACCEPT *, EFREF
TYPE 12
12 FORMAT(1X, 'ENTER VOLTAGE OF THE BACKWARD SLANTING X, ERREF'/)
TYPE *, ' '
ACCEPT *, ERREF
WRITE(7,13) REFANG, QREF, EFREF, ERREF
2 ' VOLTS',/,/,1X,'ERREF=',F10.6,' VOLTS')
C CALCULATION OF CORRECTION COEFFICIENTS CR AND CF
REFANG=(3.141592654/180.0)*REFANG
ERREFS=ERREF*ERREF
RSAV=(ERREFS-AXR)/BXR
RX=1.0/XNXR
RREF=RSAV**RX
RSAV2=RREF/(OREF*SIN(REFANG))
COT=COS(REFANG)/SIN(REFANG)
CR=COT-RSAV2
EFREFS=EFREF*EFREF
FSAV=(EFREFS-AXF)/BXF
FX=1.0/XNXF
FREF=FSAV**FX
FSAV2=FREF/(QREF*SIN(REFANG))
CF=FSAV2-COT
DELTAF = (1-CF)/(1+CF)
DELTAR = (CR-1)/(1+CR)
DELTAF=DELTAF/(3.141592654/180.0)
DELTAR=DELTAR/(3.141592654/180.0)
WRITE(7,40) CF,CR
40 FORMAT('0','CF =',Fl0.6,lX,'CR =',Fl0.6)
OPEN(UNIT=12, TYPE='NEW', NAME='DK:CFCR.DAT')
WRITE(12,100) CF,CR
100 FORMAT(' ',F11.8,5x,F11.8)
WRITE(7,41) DELTAF, DELTAR
41 FORMAT('0', 'DELTAF = ',F8.3,' DEG.',/,/,
     1 1X, 'DELTAR = ', F8.3, ' DEG.')
CLOSE (UNIT=12)
RETURN
TABLE B2: PROGRAM CONVEL
C FILENAME: CONVEL.JAL
C THIS PROGRAM CONVERTS VOLTAGES TO VELOCITIES FOR A VORTICITY
```

```
C PROBE CONSISTING OF AN X-WIRE AND A PARALLEL PROBE.
C THE PROGRAM TAKES COLLIS AND WILLIAMS CONSTANTS FROM A NORMAL
C CALIBRATION WHERE THE PROBE IS ALIGNED WITH FLOW DIRECTION
C CORRESPONDING TO ANGLE GAMMA EQUAL ZERO IN DOCUMENTATION.
C THE VOLTAGES FOR EACH WIRE AT ONE SMALL ANGLE ARE THEN ASKED
C FOR AS INPUT WHICH ARE THEN USED TO DETERMINE THE CONSTANTS
C CR AND CF. THEN A DATA FILE CAN BE CONVERTED INTO VELOCITIES
C AND AVERAGES FOR THE FOUR WIRES ARE DETERMINED, UV ALSO.
C
C AXF
          FIRST COEFFICIENT OF THE COLLIS AND WILLIAMS CALIBRATION
          FOR THE CASE OF V=0, QREF=U, AND GAMMA=0 (GAMMA IS ANGLE
          BETWEEN FLOW DIR AND STING AXIS) FOR FORWARD FACING X.
C
C BXF
        SECOND COEF OF THE C-W CALIBRATION UNDER SAME CONDITIONS
C XNXF
         EXPONENT IN THE C-W CALIB UNDER SAME CONDITIONS
C EF(I)
         VOLTAGE FOR FORWARD FACING X WIRE, CORRESPONDS
                                                            TO NEG
BETA
C ER(I)
         VOLTAGE FOR REARWARD FACING X WIRE, POSITIVE BETA
C EU1(I) VOLTAGE FROM ONE OF THE "U"-WIRES IN THE PARALLEL PROBE
C EU2(I) VOLTAGE FROM SECOND "U"-WIRE OF PARALLEL PROBE
C REFANG REFERENCE ANGLE FOR DETERMINING CR AND CF
C QREF REFERENCE SPEED FOR DETERMINING CR AND CF
C VX V COMPONENT OF VELOCITY FROM X WIRE
C UX U COMPONENT OF VELOCITY FROM X WIRE
C Ul VELOCITY FROM U-WIRE ONE
C U2 VELOCITY FROM U-WIRE TWO
C UV UV PRODUCT
C AVX V COMPONENT OF VELOCITY FROM X WIRE
C AUX U COMPONENT OF VELOCITY FROM X WIRE
C AU1 VELOCITY FROM U-WIRE ONE
C AU2 VELOCITY FROM U-WIRE TWO
C AUV UV PRODUCT
C
IMPLICIT REAL(A-Z)
INTEGER I, J, K, IPOINT, ICHANL, IPTS
LOGICAL*1 DATFIL(11), DATOUT(15), YN
C THE FOLLOWING SECTION OF CODE ACCEPTS A FILE NAME FOR THE
C INPUT OF THE VOLTAGE FILES OPENS THE FILE, OPENS THE FILE
C FOR THE OUTPUT VELOCITIES AND A FILE FOR THE AVERAGE VELOCITY
C AND THEN OPENS CALCRV.DAT FOR READING A, B, N, AND STANDARD DEV.
C COEF OBTAINED FROM STANDARD C-W FITTING PROGRAM FOR CASE WHEN
C "X"-WIRE AT GAMMA=0 AND V=0, U=QREF
C
C PROGRAM REVISED BY JEFFERY A. LOVETT
C
WRITE(7,120)
120 FORMAT('0','***** USING PROGRAM CONVEL *****',/,
```

```
1X, THIS PROGRAM REQUIRES FORWARD FACING X-WIRE BE WIRE
ONE',/,
        1X, AND REARWARD FACING X-WIRE BE WIRE TWO IN CALCRV AND
DATA')
        WRITE(7,121)
121 FORMAT('0', 'ENTER INPUT DATA FILE NAME ON DK : ',s)
CALL GTLIN(DATFIL)
        WRITE(7,122)
122 FORMAT('0','ENTER DESIRED OUTPUT DATA FILE NAME : ',$)
CALL GTLIN(DATOUT)
WRITE(7,123)
123 FORMAT('0','INPUT THE TOTAL NUMBER OF POINTS TAKEN: ',s)
ACCEPT *, IPTS
WRITE(7,124)
124 FORMAT('0','INPUT NUMBER OF CHANNELS: ',$)
ACCEPT *, ICHANL
IPOINT=IPTS/ICHANL
CCHECK=0
WRITE(7,301)
301 FORMAT('0','DO YOU WANT TO CALCULATE CF AND CR : ',$)
CALL GTLIN(YN)
IF(SCOMP(YN, 'Y').NE.0) GOTO 302
CALL CFCR(AXF, BXF, XNXF, AXR, BXR, XNXR, CF, CR)
GO TO 303
302 OPEN(UNIT=14, TYPE='OLD', NAME='DK:CFCR.DAT')
READ(14,*) CF,CR
CLOSE (UNIT=14)
303 OPEN(UNIT=11,NAME=DATFIL,TYPE='OLD',FORM='UNFORMATTED')
OPEN (UNIT=12, NAME=DATOUT, TYPE='NEW', FORM='UNFORMATTED',
       INITIALSIZE=500)
OPEN(UNIT=13, NAME='AVGVEL.DAT', TYPE='NEW', INITIALSIZE=40)
C CALCULATION OF VELOCITIES
OPEN(UNIT=14, TYPE='OLD', NAME='DK:CALCRV.DAT')
READ(14,*)AXF,BXF,SD1,XNXF
READ(14,*)AXR, BXR, SD2, XNXR
READ(14,*)AU1,BU1,SD3,XNU1
READ(14,*)AU2,BU2,SD4,XNU2
CLOSE (UNIT=14)
SUMUX=0.0
SUMVX=0.0
SUMUV=0.0
SUMU1=0.0
SUMU2=0.0
NNN=0
ICHK=0
DO 300 J=1, IPOINT
READ(11, END=300) EF, ER, EU1, EU2
IF(EF.GT.5000.0) GOTO 111
IF(ER.GT.5000.0) GOTO 111
```

```
IF(EU1.GT.5000.0) GOTO 111
IF(EU2.GT.5000.0) GOTO 111
GO TO 127
111
    NNN=2
125 WRITE(7,126) J
126 FORMAT('0','****WARNING**** POSSIBLE BAD DATA POINT',/,
     1 1X, 'POINT NUMBER ', 15, ' HAS BEEN REJECTED', /, /)
IF(NNN.EO.2) WRITE(7,112)
    FORMAT(' ','VOLTAGE TOO HIGH, OVER 5.0 VOLTS')
NNN = 0
ICHK=ICHK+1
GO TO 128
127 EFSQ=(EF/1000.0)*(EF/1000.0)
ERSQ=(ER/1000.0)*(ER/1000.0)
EU1SQ=(EU1/1000.0)*(EU1/1000.0)
EU2SQ = (EU2/1000.0) * (EU2/1000.0)
IF(EFSQ.LE.AXF) GOTO 125
IF(ERSQ.LE.AXR) GOTO 125
SAVEF=((EFSO-AXF)/BXF)
RECPX=1.0/XNXF
F=SAVEF**RECPX
SAVER=((ERSQ-AXR)/BXR)
RECPX=1.0/XNXR
R=SAVER**RECPX
C=CF+CR
UX = ((CF/C)*R) + ((CR/C)*F)
VX = (F - R) / C
SAVE1 = ((EU1SQ-AU1)/BU1)
RECPX=1.0/XNU1
U1=SAVE1**RECPX
SAVE2 = ((EU2SQ-AU2)/BU2)
RECPX=1.0/XNU2
U2=SAVE2**RECPX
UV=UX*VX
SUMUX=SUMUX+UX
SUMVX=SUMVX+VX
SUMUV=SUMUV+UV
SUMU1=SUMU1+U1
SUMU2=SUMU2+U2
WRITE(12) UX, VX, U1, U2, UV
128
     CONTINUE
300 CONTINUE
C CALCULATION OF AVERAGE VELOCITIES
C
IPOINT=IPOINT-ICHK
AUX=SUMUX/IPOINT !AVERAGE U OF X
AVX=SUMVX/IPOINT !AVERAGE V OF X
AVUV=SUMUV/IPOINT !AVERAGE UV OF X
AVU1=SUMU1/IPOINT !AVERAGE OF U1
AVU2=SUMU2/IPOINT !AVERAGE OF U2
```

```
CALL CLOSE(11)
CALL CLOSE(12)
CALL CLOSE(13)
CALL EXIT
TABLE B3: PROGRAM REDUC2
C THIS IS A USER CALLABLE SUBROUTINE TO BE USED WITH THE
C MACRO FILE REDUCL.MAC FOR DETERMINING THE TIME DERIVATIVES
C AND VORTICITY COMPONENTS FROM VORTICITY PROBE SIGNALS
C THE CHANNEL AND CONSTANT ASSIGNMENTS ARE ACCORDING TO
C LABELING OF REDUCL.MAC.
C PROGRAM CREATED BY JEFFERY A. LOVETT
C
LOGICAL*1 LINE(81), T, TM1, NS, NC, NCMD, NUSR, LVARS
COMMON /VAR/VARS(128), IVARS(128), LVARS(128)
COMMON /SYS/T, TMl, NS, NC, NCMD, NUSR, LUIN, LUOUT, LUC
C THREE STATEMENT FUNCTIONS TO ACCESS THE VARS ARRAY APPEAR BELOW:
KF(I)=NS-1+I
IVT(I) = NC - 1 + I + T * 16
IVTMl(I)=NC-1+I+TMl*16
C----SUBTRACT THE AVERAGE VELOCITIES
C
VARS(IVT(1))=VARS(IVT(1))-VARS(KF(2))
VARS(IVT(2))=VARS(IVT(2))-VARS(KF(3))
VARS(IVT(3))=VARS(IVT(3))-VARS(KF(4))
VARS(IVT(4)) = VARS(IVT(4)) - VARS(KF(5))
C
C----CALCULATE UV
VARS(IVT(5))=VARS(IVT(1))*VARS(IVT(2))
C-----CALCULATE THE TIME DERIVATIVES
VARS(IVT(7)) = (VARS(IVT(1)) - VARS(IVTM1(1)))/VARS(KF(6))
VARS(IVT(8)) = (VARS(IVT(2)) - VARS(IVTM1(2))) / VARS(KF(6))
VARS(IVT(9)) = (VARS(IVT(3)) - VARS(IVTM1(3))) / VARS(KF(6))
VARS(IVT(10)) = (VARS(IVT(4)) - VARS(IVTM1(4)))/VARS(KF(6))
VARS(IVT(11))=(VARS(IVT(5))-VARS(IVTM1(5)))/VARS(KF(6))
C
```

WRITE(13,*) AUX, AVX, AVU1, AVU2, AVUV

```
C----CALCULATE DU/DY
VARS(IVT(6)) = (VARS(IVT(4)) - VARS(IVT(3))) / VARS(KF(8))
C----CALCULATE DV/DX
VARS(IVT(12))=VARS(IVT(8))/(-1.0*VARS(KF(10)))
C-----CALCULATE DU/DZ
C
VARS(IVT(14)) = (VARS(IVT(3)) + VARS(IVT(4)))/2.0
VARS(IVT(13))=(VARS(IVT(1))-VARS(IVT(14)))/VARS(KF(9))
C-----DETERMINE THE VORTICITY COMPONENTS
VARS(IVT(15)) = (VARS(IVT(12)) - VARS(IVT(6)))/2.0
VARS(IVT(16)) = VARS(IVT(13))/2.0
RETURN
TABLE B4: PROGRAM SEPPTS
C
C SEPERATE INTERVALS OF DATA FILE
C
C THIS PROGRAM TAKES SELECTED RECORDS
  FROM A BINARY DATA FILE
C AND OUTPUTS IT INTO ANOTHER FILE
C THIS PROGRAM WAS DEVELOPED
С
 FOR SEPERATING INTERVALS OF
C VELOCITIES TO BE INPUT INTO HARVY
С
  OR OTHER REDUCTION PROGRAMS
C
C PROGRAM CREATED BY JEFFERY A. LOVETT
LOGICAL*1 FNAME(15), ONAME(15), INPUT
DIMENSION VOLDAT(16)
C
TYPE 500
TYPE 504
ACCEPT *, N
4 TYPE 506
READ(7,*) NFIRST, NLAST
TYPE 502
CALL GTLIN(FNAME)
OPEN (UNIT=2, NAME=FNAME, FORM='UNFORMATTED', TYPE='OLD')
TYPE 505
CALL GTLIN (ONAME)
```

```
OPEN (UNIT=3, NAME=ONAME, TYPE='NEW', FORM='UNFORMATTED',
      1 INITIALSIZE=200)
DO 10 M=1,NLAST
READ(2,END=700) (VOLDAT(I), I=1,N)
IF(M.LT.NFIRST) GOTO 10
WRITE(3,END=700) (VOLDAT(I), I=1,N)
10 CONTINUE
700 CLOSE (UNIT=2)
CLOSE (UNIT=3)
C----
C FORMAT STATEMENTS
500 FORMAT('0','****** USING PROGRAM SEPPTS *******
501 FORMAT(' ','DO YOU WANT TO USE ADOLOG DAT 2 ' C
501 FORMAT( ','DO YOU WANT TO USE AD2LOG.DAT ? ',$)
502 FORMAT('0','ENTER INPUT DATA FILE NAME : ',$)
503 FORMAT('','ENTER FILE NAME WITH BELLETING
                 'DO YOU WANT TO USE AD2LOG.DAT ? ',$)
503 FORMAT(' ','ENTER FILE NAME WITH DEVICE: ',$)
504 FORMAT(' ','ENTER NUMBER OF CHANNELS ',$)
                 'ENTER NUMBER OF CHANNELS IN DATA FILE : ',$)
505 FORMAT(' ', 'ENTER FILE NAME FOR OUTPUT : ',$)
506 FORMAT('0', 'ENTER FIRST AND LAST POINT TO STORE: ',s)
CALL EXIT
TABLE B5: PROGRAM SEP4CH
C SEPERATE CHANNELS OF DATA FILE
C THIS PROGRAM TAKES SELECTED RECORDS
  FROM A BINARY DATA FILE
 AND OUTPUTS THE ASCII CONVERSION
  INTO ANOTHER FILE
C THIS PROGRAM WAS DEVELOPED FOR
  SEPERATING CHANNELS OF
C SIGNALS TO BE PLOTTED ON THE TEKTRONIX
C PROGRAM CREATED BY JEFFERY A. LOVETT
LOGICAL*1 FNAME(15), ONAME(15), INPUT
DIMENSION VOLDAT(16)
TYPE 500
3 TYPE 504
READ(7,*) N
4 TYPE 506
READ(7,*) NFIRST, NLAST
```

```
WRITE(7,601)
READ(7,*) N1,N2,N3,N4
TYPE 502
CALL GTLIN(FNAME)
OPEN (UNIT=2, NAME=FNAME, FORM='UNFORMATTED', TYPE='OLD')
TYPE 505
CALL GTLIN(ONAME)
OPEN (UNIT=3, NAME=ONAME, TYPE='NEW', INITIALSIZE=800)
DO 10 M=1.NLAST
READ(2,END=700) (VOLDAT(I), I=1, N)
IF(M.LT.NFIRST) GOTO 10
WRITE(3,*) VOLDAT(N1), VOLDAT(N2), VOLDAT(N3), VOLDAT(N4)
10 CONTINUE
700 CLOSE(UNIT=2)
CLOSE (UNIT=3)
C FORMAT STATEMENTS
500 FORMAT('0','****** USING PROGRAM SEP4CH ******',/)
501 FORMAT('','DO YOU WANT TO USE AD2LOG.DAT ?',$)
502 FORMAT('0','ENTER INPUT DATA FILE NAME : ',$)
503 FORMAT('','ENTER FILE NAME WITH DEVICE : ',$)
504 FORMAT('','ENTER NUMBER OF CHANNELS IN DATA FILE : ',$
505 FORMAT('0','ENTER FILE NAME FOR OUTPUT : ',$)
506 FORMAT('0','ENTER FIRST AND LAST POINT TO STORE : ',$)
601 FORMAT('0','ENTER THE 4 CHANNELS YOU WOULD LIKE OUTPUT :
                                                                                         ',$)
CALL EXIT
TABLE B6: PROGRAM STSTCS
C-----
C THIS PROGRAM DETERMINES THE
         SAMPLE MEAN
С
          SAMPLE STANDARD DEVIATION
С
         SKEWNESS FACTOR
С
        FLATNESS FACTOR
C FOR A SAMPLE OF SIZE N AND PRINTS
C THE VALUES OUT. THE DATA FILE SHOULD
C CONTAIN THE DATE, NUMBER OF DATA POINTS, DATA
DIMENSION X(550), XDIFF(550), FORD(550)
C READ IN DATE AND NUMBER OF DATA POINTS
READ (3,*) MONTH, IDAY, IYEAR
READ (3,*) N, UTAU, ANU, RTHETA, UINF, DELTA9
XN = N
XSUM=0.0
```

```
C SET PROPER DIMENSION ORDER
C
WRITE (7,750)
READ (5,*) L
IF(L.EQ.1) GO TO 17
IF(L.EQ.2) GO TO 18
ORDER=1000.0
GO TO 19
17 ORDER=1.0
GO TO 19
18 ORDER=100.0
C READ IN DATA POINTS
19 READ (3,*) (X(I),I=1,N)
C CALCULATE SAMPLE MEAN
C
DO 20 I=1,N
20 XSUM=XSUM+X(I)
XMEAN=XSUM/XN
XNDMN=(XMEAN*UTAU)/ANU
XNDMN=XNDMN/ORDER
WRITE (7,840) MONTH, IDAY, IYEAR
WRITE (7,841) N
WRITE (7,700) RTHETA, UINF, DELTA9, ANU, UTAU, XNDMN
WRITE (7,800) XMEAN
C CALCULATE SAMPLE STANDARD DEVIATION
DO 21 J=1,N
21 XDIFF(J) = X(J) - XMEAN
XDIFSQ=0.0
DO 30 K=1,N
30 XDIFSQ=XDIFSQ+XDIFF(K)*XDIFF(K)
STDDSQ=XDIFSQ/(XN-1.0)
STDDEV=(STDDSQ)**0.5
WRITE (7,810) STDDEV
C CALCULATE SKEWNESS FACTOR
XDIFCU=0.0
DO 40 L=1, N
40 XDIFCU=XDIFCU+((XDIFF(L)*XDIFF(L))*XDIFF(L))
SDENOM=(XDIFSQ/XN)**1.5
SKEWNF=XDIFCU/(XN*SDENOM)
WRITE (7,820) SKEWNF
C CALCULATE FLATNESS FACTOR
```

```
XDIFF4=0.0
DO 50 M=1, N
50 XDIFF4=XDIFF4+((XDIFF(M)*XDIFF(M))**2.0)
FDENOM=(XDIFSO*XDIFSO)/(XN*XN)
FLATNF=XDIFF4/(XN*FDENOM)
WRITE (7,830) FLATNF
C ORDER DATA
X(N+1)=0.0
IPl=0
DO 60 I=1.N
IP1=I+1
DO 55 J=IP1,N+1
IF(X(I).LE.X(J)) GO TO 55
TEMP=X(I)
X(I)=X(J)
X(J) = TEMP
55 CONTINUE
60 CONTINUE
C LIST THE ORDERED DATA WITH FREQUENCY
WRITE (7,850)
DO 80 I = 2, N+1
IF(I.EQ.2) GO TO 70
GO TO 74
70 CHECK=X(2)
NOCNT=0
74 IF(X(I).GT.CHECK) GO TO 78
NOCNT=NOCNT+1
GO TO 80
78 WRITE(7,860) CHECK, NOCHT
CHECK=X(I)
NOCNT=1
80 CONTINUE
WRITE (7,860) CHECK, NOCHT
C DETERMINE THE RANGE OF VALUES AND THE PLOTTING INTERVAL
XRANGE=X(N+1)-X(1)
IF((XRANGE/60.0).LE.1.0) GO TO 97
DELTAF=5.0
GO TO 190
97 IF((XRANGE/50.0).LE.1.0) GO TO 98
DELTAF=3.0
GO TO 190
98 IF((XRANGE/40.0).LE.1.0) GO TO 99
DELTAF=2.5
GO TO 190
99 IF((XRANGE/20.0).LE.1.0) GO TO 100
```

```
DELTAF=2.0
GO TO 190
100 IF((XRANGE/10.0).LE.1.0) GO TO 110
DELTAF=1.0
GO TO 190
110 IF((XRANGE/5.0).LE.1.0) GO TO 120
DELTAF=0.5
GO TO 190
120 IF((XRANGE/2.0).LE.1.0) GO TO 130
DELTAF=0.25
GO TO 190
130 IF((XRANGE/1.0).LE.1.0) GO TO 140
DELTAF=0.1
GO TO 190
140 DELTAF=0.05
190 CONTINUE
C DETERMINE THE NUMBER OF DATA POINTS IN EACH INTERVAL
WRITE (7,870)
K = 2
MO=N+1
DO 230 I=1,21
NCOUNT = 0
IF(I.GE.2) GO TO 211
FORD(I)=0.05
GO TO 212
211 IN=I-1
FORD(I)=FORD(IN)+DELTAF
212 DO 220 J=K,MO
IF(X(J).GT.FORD(I)) GO TO 215
IF(I.EQ.1) GO TO 214
IF(X(J).GT.FORD(I-1)) GO TO 214
NCOUNT=0
GO TO 220
214 NCOUNT=NCOUNT+1
GO TO 220
215 K=J
J=MO
220 CONTINUE
XNDFRD=(FORD(I)*UTAU)/ANU
XNDFRD=XNDFRD/ORDER
230 WRITE(7,880) FORD(I), NCOUNT, XNDFRD
700 FORMAT(/,1X,'RTHETA = ',F10.3,/,1X,'UINF = '
     ORMAT(/,IX, RTHETA = ',F10.3,/,IX, UINF = ',
1 F10.6,' M/S',/,IX,'DELTA99 = ',F10.6,' M',/,IX,'KINEMATIC
     1 'VISCOSITY = ',F10.8,' M*M/S',/,1X,'UTAU = ',F10.6,
     l'
             M/S',/,1X,'NON-DIMENSIONALIZED MEAN DIMENSION =
',F10.2,
     1 /,/,/,1x,'STATISTICAL QUANTITIES-----',/)
750 FORMAT(/,1X,' INPUT THE PROPER NUMBER FOR THE DIMENSION USED',
```

```
2 = CENTILLE
3 = MILLIMETERS')
800 FORMAT (/,1x,'THE SAMPLE MEAN XBAR IS ',F10.6)
810 FORMAT (/,lx,'THE SAMPLE STANDARD DEVIATION SX IS
                                                          ',F10.6)
820 FORMAT (/,lx,'THE SKEWNESS FACTOR S IS ',F10.6)
830 FORMAT (/,lx,'THE FLATNESS FACTOR F IS ',F10.6)
840 FORMAT (/,1X,'DATA TAKEN ',12,2X,12,2X,14)
841 FORMAT(/,1X,'NUMBER OF DATA POINTS ',13)
850 FORMAT(/,/,1X,'ORDERED DIMENSION X FR
                                                FREQUENCY')
860 FORMAT(1X,F10.6,' X ',I4)
870 FORMAT(/,/,1X,'DIMENSION X HISTOGRAM FREQUENCY',
1' X NON-DIMENSIONAL DIMENSION')
     880 FORMAT(1X,F10.6,' X ',I3,' X ',F10.4)
STOP
TABLE B7: PROGRAM AVGINT
C SEPERATE INTERVALS OF DATA FILE AND AVERAGES VALUES
C THIS PROGRAM TAKES SELECTED RECORDS FROM A BINARY DATA FILE
C AND OUTPUTS QUANTITIES INTO ANOTHER FILE
C THIS PROGRAM WAS DEVELOPED FOR SEPERATING INTERVALS OF
C DATA FROM SEVERAL DATA FILES AND DETERMINE AVERAGE VALUES
C FOR EACH CHANNEL AND SEPERATES EACH INTERVAL INTO FOUR
C QUADRANTS FOR +U,+V +U,-V -U,+V -U,-V
C***** REQUIRES U IN CHANNEL 1, V IN CHANNEL 2 **********
C
C PROGRAM CREATED BY JEFFERY A. LOVETT
LOGICAL*1 FNAME(15), ONAME(15)
DIMENSION VOLDAT(16), SUM(16), SUM1(16), SUM2(16), SUM3(16), SUM4(16)
TYPE 500
TYPE 504
ACCEPT *,NC
TYPE 501
ACCEPT *, NF
TYPE 505
CALL GTLIN(ONAME)
OPEN (UNIT=3, NAME=ONAME, TYPE='NEW', FORM='FORMATTED',
     1 INITIALSIZE=200)
XN=0.0
```

```
XN1=0.0
XN2 = 0.0
XN3 = 0.0
XN4=0.0
DO 101 L=1,NC
SUM(L)=0.0
SUM1(L)=0.0
SUM2(L)=0.0
SUM3(L) = 0.0
SUM4(L)=0.0
101 CONTINUE
DO 302 M=1,NF
WRITE(7,599) M
WRITE(7,503) M
ACCEPT *, NI
TYPE 502
CALL GTLIN(FNAME)
OPEN (UNIT=2, NAME=FNAME, FORM='UNFORMATTED', TYPE='OLD')
LASTN=0
DO 301 N=1,NI
4 WRITE (7,506) N
READ(7,*) NFIRST, NLAST
NREAD=NLAST-LASTN
DO 10 J=1,NREAD
UPLUS=0.0
VPLUS=0.0
READ(2, END=700) (VOLDAT(I), I=1,NC)
NCHK=J+LASTN
IF(NCHK.LT.NFIRST) GOTO 10
XN = XN + 1.0
DO 201 K=1,NC
SUM(K) = SUM(K) + VOLDAT(K)
201 CONTINUE
IF(VOLDAT(1).GT.0.0) UPLUS=2.0
IF(VOLDAT(2).GT.0.0) VPLUS=2.0
IF(UPLUS.NE.2.0) GO TO 220
IF(VPLUS.NE.2.0) GO TO 210
С
C----QUADRANT 1
XN1=XN1+1.0
DO 205 K=1,NC
SUM1(K) = SUM1(K) + VOLDAT(K)
205 CONTINUE
GO TO 10
C-----QUADRANT 2
210 XN2=XN2+1.0
DO 211 K=1,NC
SUM2(K) = SUM2(K) + VOLDAT(K)
```

```
211 CONTINUE
GO TO 10
C----QUADRANT 3
220 IF(VPLUS.NE.2.0) GO TO 230
XN3 = XN3 + 1.0
DO 221 K=1,NC
SUM3(K) = SUM3(K) + VOLDAT(K)
221 CONTINUE
GO TO 10
C----QUADRANT 4
230 XN4 = XN4 + 1.0
DO 231 K=1,NC
SUM4(K) = SUM4(K) + VOLDAT(K)
231 CONTINUE
10 CONTINUE
LASTN=NLAST
301 CONTINUE
700 CLOSE(UNIT=2)
302 CONTINUE
WRITE(3,508) XN
DO 304 L=1,NC
AVG=SUM(L)/XN
WRITE(3,507) L, AVG
304 CONTINUE
WRITE(3,511)
WRITE(3,508) XN1
DO 305 L=1,NC
AVG=SUM1(L)/XN1
WRITE(3,507) L, AVG
305 CONTINUE
WRITE(3,512)
WRITE(3,508) XN2
DO 306 L=1,NC
AVG=SUM2(L)/XN2
WRITE(3,507) L, AVG
306 CONTINUE
WRITE(3,513)
WRITE(3,508) XN3
DO 307 L=1,NC
AVG=SUM3(L)/XN3
WRITE(3,507) L, AVG
307 CONTINUE
WRITE(3,514)
WRITE(3,508) XN4
DO 308 L=1,NC
AVG=SUM4(L)/XN4
WRITE(3,507) L, AVG
```